

DISSERTATION

A Constitutive Model for the Elasto-Plasto-Damage Ply Behavior in Laminated FRP Composites: Its Development, Implementation, and Application in FEM Simulations

ausgeführt zum Zwecke der Erlangung des akademischen Grades eines
Doktors der technischen Wissenschaften unter der Leitung von

Univ.Doz. Dipl.-Ing. Dr.techn. Heinz Pettermann

E317

Institut für Leichtbau und Struktur-Biomechanik

eingereicht an der Technischen Universität Wien

Fakultät für Maschinenwesen und Betriebswissenschaften

von

Dipl.-Ing. Thomas Flatscher

Matrikelnummer 0025279

Favoritenstraße 86/15

1100 Wien

Wien, im März 2010

Thomas Flatscher

für Peter

Acknowledgment

This work was carried out in the course of my employment at the Institute of Lightweight Design and Structural Biomechanics (ILSB) at the Vienna University of Technology, which hosted a node of the Austrian Aerospace Research (AAR) / Network for Materials and Engineering for many years. The funding of the ILSB as well as the funding of the AAR by the Austrian Ministry of Economics and Labor is gratefully acknowledged.

The experimental tests presented in the thesis were carried out at the *Polymer Competence Center Leoben GmbH* (PCCL) within the framework of the *K_{plus}*-Program of the Austrian Ministry of Traffic, Innovation and Technology with contributions from the University of Leoben and *FACC AG*. The valuable collaboration is gratefully acknowledged.

I am indebted to my thesis advisor, Heinz Pettermann, who contributed to this work by many fruitful discussions. In particular I thank him for his positive attitude. I also thank Clara Schuecker, whose scientific work provided the basis of the present thesis. Furthermore, I thank Prof. Gerald Pinter for acting as co-advisor.

I wish to express my sincere gratitude to all members of the ILSB for creating such a friendly and supportive work environment. Special thanks go to Prof. Helmut J. Böhm, Prof. Franz G. Rammerstorfer, and Prof. Philippe K. Zysset as well as to my cheerful office mates Gerald Wimmer and Sergio Nogales.

I thank my family, especially my parents, Margit and Thomas Flatscher. None of this would have been possible without their support.

Contents

Abstract	VIII
Kurzfassung	X
Notations	XII
1 Introduction	1
1.1 Fiber reinforced laminates	2
1.2 Scope of the present work	5
2 Literature review	7
2.1 Recommended textbooks	7
2.2 From FPF to continuum damage	8
2.3 Puck's failure criterion	12
3 The constitutive model	15
3.1 Distributed brittle damage	18
3.2 Multi-surface plasticity	23
3.3 Localized brittle damage	29
3.4 Capabilities of the constitutive model	37
3.5 Calibration	39
3.6 Implementation	43

4 Applications	53
4.1 Biaxial loading of a UD laminate	56
4.2 Test cases from the first WWFE	64
4.3 Test cases from the third WWFE	77
4.4 Mesh dependency	98
4.5 Coupon tests	103
4.6 Open hole tension tests	120
5 Summary	129
A Notations	133
B Puck's failure criterion	137
C Material parameters	139
D Mean field theory	143
E Transformations	149
F Energy dissipation	153
G Usage of the UMAT	155
Bibliography	163

Abstract

For structural analysis of laminated fiber reinforced polymer composites, a reliable constitutive model is required which describes the intra-ply behavior of the embedded plies. As it is desired to exploit the potential of laminated composites, also the response beyond elasticity has to be accounted for in such a model. Motivated by this fact, a constitutive model for the nonlinear intra-ply behavior is developed, implemented, and applied in the present work. In the formulation of this constitutive model, two major types of effects which both lead to pronounced non-linearity are distinguished as being motivated from experimental observations. These effects are *stiffness degradation* and *unrecoverable strain accumulation*.

Stiffness degradation is attributed to microscopic brittle matrix cracking, fiber/matrix debonding, as well as progressive fiber failure. Such phenomena are expected to lead to a decreased stiffness primarily, and, accordingly, respective strains are taken to be recoverable after unloading. Stiffness degradation is modeled via continuum damage mechanics, whereby the ply material behavior is featured by the behavior of an appropriate fictitious material. This way, the anisotropic effect of brittle damage is incorporated. The formulation for damage evolution consists of two different approaches. The first approach deals with stiffness degradation due to widespread, evenly distributed matrix dominated phenomena. Respective damage evolution equations are related to the material exertion predicted by recourse to Puck's failure surface. Here damage accumulation is accompanied by slight strain hardening. The second approach for damage evolution deals with stiffness degradation triggered by localized matrix dominated as well as fiber dominated phenomena. Respective damage evolution equations are formulated with respect to elastic strains. Here damage accumulation causes strain softening.

Unrecoverable strain accumulation is associated to the formation of microscopic areas with inelastically deformed matrix material. Respective strains are referred to as plastic strains since their evolution is described by two modeled plasticity mechanisms. These mechanisms treat the evolution of plastic in-plane shear strains and the evolution of plastic normal strains of the ply. The presented approach leads to a multi-surface formulation and is able to capture the ductile portion of the behavior of fiber reinforced polymer plies.

The development of the constitutive model aims at the analysis of laminated, thin-walled structures as for example used in many applications of aeronautics. Since the Finite Element Method is a state-of-the-art tool for structural analyses, the constitutive law is implemented as user defined material routine for the commercial Finite Element package *Abaqus/Standard 6.9* (*Dassault Systèmes Simulia Corp., Providence, RI, USA*). In this context also the material Jacobian matrix is derived. Furthermore, viscous regularization to alleviate convergence problems as well as a method to alleviate the well-known mesh dependency in the strain softening regime are addressed.

In order to assess the predictive capabilities of the proposed constitutive model, non-linear Finite Element simulations are conducted. Thereby different material systems, various laminate layups, complex loading scenarios, and structural responses are considered. The predictions are discussed in detail and compared to experimental results. The agreement between predictions and experimental results is shown to be good.

The proposed constitutive model offers some outstanding features concerning the simulation of laminated composites. Firstly, residual deformations are predicted which is very unlike to many other available models. Secondly, the laminate stiffness affected by anisotropic brittle damage is captured. Finally, the behavior of components in the proximity of the load carrying capacity can be simulated since strain softening is modeled as well. All the mentioned phenomena are incorporated within a single constitutive model, which is easy to calibrate and readily implemented within the Finite Element Method.

Kurzfassung

Für die Analyse von Strukturen aus laminierten Faser-Kunststoff-Verbundwerkstoffen wird ein zuverlässiges Konstitutivgesetz benötigt, das das Verhalten der eingebetteten Schichten beschreibt. Da das Potential moderner Materialsysteme weiter ausgeschöpft werden soll, muss in einem derartigen Modell auch das Verhalten über das elastische Limit hinaus erfasst werden. Dementsprechend wird in der vorliegenden Arbeit ein Konstitutivgesetz für das nichtlineare Schichtverhalten entwickelt, implementiert und angewendet. Auf Grund von experimentellen Beobachtungen werden bei der Formulierung dieses Konstitutivgesetzes zwei Effekte unterschieden, die beide zu deutlich nichtlinearem Verhalten beitragen. Diese Effekte sind *Degradation der Steifigkeit* einerseits und die *Akkumulation bleibender Verzerrungen* andererseits.

Die Degradation der Steifigkeit wird der Ausbildung von Mikrorissen in der Matrix, dem Versagen der Verbindung zwischen Faser und Matrix sowie fortschreitendem Faserbruch zugeschrieben. Da angenommen wird, dass sich derartige Phänomene ausschließlich auf die Steifigkeit des Schichtmaterials auswirken, werden entsprechende Verzerrungen als reversibel modelliert. Die Degradation der Steifigkeit selbst wird über Kontinuumschädigungsmechanik abgebildet. Um den anisotropen Charakter der Degradation zu erfassen, wird das Verhalten des Schichtmaterials durch das Verhalten eines fiktiven Materials imitiert. Die Modellierung der Degradationsevolution besteht wiederum aus zwei Ansätzen. Der erste Ansatz befasst sich mit Degradation, die von homogen verteilten, matrixdominierten Phänomenen hervorgerufen wird. Die entsprechenden Evolutionsgleichungen sind mit Bezug auf die Versagensfläche von Puck formuliert. Bei diesem ersten Ansatz geht fortschreitende Degradation mit Verfestigung einher. Der zweite Ansatz befasst sich mit Degradation in Folge von lokalisierten, matrix- und faserdominierten Phänomenen. Hier sind die Evolutionsgleichungen in

Abhängigkeit von den elastischen Verzerrungen formuliert und fortschreitende Degradation geht mit Entfestigung einher.

Die Akkumulation bleibender Verzerrungen wird mit der Ausbildung von mikroskopisch kleinen Gebieten mit stark unelastisch verformten Matrixmaterial in Zusammenhang gebracht. Bleibende Verzerrungen werden als plastische Verzerrungen bezeichnet, da ihre Entwicklung über zwei Plastizitätsmechanismen modelliert wird. Die Mechanismen befassen sich dabei mit der Entwicklung von Schiebungen einerseits und mit der Entwicklung von Schichtdehnungen andererseits. Die vorgeschlagene Zugang führt zu einer Formulierung bei der mehrere Fließflächen berücksichtigt werden. Auf diese Weise kann der duktile Anteil der Schichtantwort erfasst werden.

Das übergeordnete Ziel der Entwicklung des Konstitutivgesetzes ist es, Analysen von dünnwandigen Strukturen bestehend aus laminierten Faser-Kunststoff-Verbundwerkstoffen zu ermöglichen. Da für Strukturanalysen häufig Finite Elemente Methoden verwendet werden, wird das Konstitutivgesetz als benutzerdefiniertes Material für das kommerzielle Programm *Abaqus/Standard* implementiert. Darüber hinaus müssen besondere Maßnahmen getroffen werden, die in der vorliegenden Arbeit behandelt werden. So muss die Jacobimatrix des Materials berechnet werden. Weiterhin wird eine Methode zur Minderung der Netzabhängigkeit und viskose Regularisierung zur Minderung von Konvergenzproblemen im Entfestigungsbereich eingeführt.

Um die Vorhersagen des vorgeschlagenen Konstitutivgesetzes zu überprüfen, wurden zahlreiche nichtlineare Finite Elemente Simulationen durchgeführt. Es wurden dabei verschiedene Materialsysteme, unterschiedliche Lagenaufbauten, z.T. komplexe Belastungszenarien und Strukturantworten untersucht. Die Vorhersagen werden ausführlich diskutiert und mit experimentellen Ergebnissen verglichen. Der Vergleich mit experimentellen Ergebnissen zeigt weitgehend gute Übereinstimmung.

Das vorgeschlagene Konstitutivgesetz verfügt über einige besondere Eigenschaften. Zum einen können bleibende Verformungen vorhergesagt werden, was mit vielen anderen verfügbaren Modelle nicht möglich ist. Zum anderen wird der Effekt von anisotroper spröder Schädigung auf die Laminatsteifigkeit erfasst. Außerdem kann das Verhalten von Bauteilen bei Belastungen in der Nähe der Tragfähigkeit simuliert werden, da auch entfestigendes Verhalten modelliert ist. Alle genannten Phänomene sind in einem Konstitutivgesetz abgebildet, welches außerdem leicht zu kalibrieren und innerhalb der Finite Elemente Methode implementiert ist.

Notations

Abbreviations

FEM	finite element method
FRP	fiber reinforced polymer
FPF	first ply failure
UD	unidirectional
WWFE	world wide failure exercise
$x-y-z$	laminate coordinate system
1-2-3	ply coordinate system
$l-n-t$	fracture plane coordinate system
d_I, d_{II}	modeled damage mechanisms
p_I, p_{II}	modeled plasticity mechanisms

Subscripts

x, y, z	laminate coordinates
1, 2, 3	ply coordinates
l, n, t	fracture plane coordinates
I, II	refers to modeled plasticity or damage mechanisms

Superscripts

- (0) refers to the virgin ply material
- (el) refers to elastic strains
- (pl) refers to plastic strains
- (t) refers to “tension”
- (c) refers to “compression”
- (f) refers to “fiber”
- (m) refers to “matrix”
- (p) refers to population p of inhomogeneities

Tensors and matrices

In the present work basically two different notations are used. The engineering notation (\mathbf{a} , \mathbf{A}) is used to represent tensorial equations based on tensors of rank two and four by equations based on vectors and matrices. The vector/matrix notation ($\underline{\mathbf{a}}$, $\underline{\underline{\mathbf{A}}}$) is used for various equations where classical matrices and vectors are involved. The difference between these notations, the limited applicability of the vector/matrix notation with respect to tensorial equations as well as other details are addressed in Appendix A. The used notations are summarized in the listing below.

Engineering notation:

- \mathbf{a} , $\boldsymbol{\alpha}$... vector representations of symmetric tensors of rank two
- \mathbf{A} , \mathbf{B} ... matrix representations of tensors of rank four with minor symmetry

Vector/matrix notation:

- $\underline{\mathbf{a}}$, $\underline{\boldsymbol{\alpha}}$... vectors
- $\underline{\underline{\mathbf{A}}}$, $\underline{\underline{\mathbf{B}}}$... matrices

Coordinate systems

In the present work fiber reinforced laminates are considered which consist of many stacked plies. For each ply a local ply coordinate system 1–2–3 is defined, cf. Fig. 1, where 1 denotes the fiber direction, 2 denotes the in-plane transverse direction, and 3 denotes the out-of-plane transverse direction. The fiber orientation of a ply is defined by the angle ψ with respect to the laminate coordinate system, x – y – z . The x - and the y -axis of the laminate coordinate system denote in-plane directions, whereas the z -axis refers to the out-of-plane direction of the laminate.

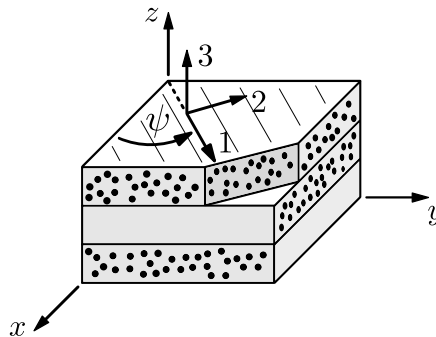


Figure 1: Laminate with global coordinate system, x – y – z ; definition of a local ply coordinate system, 1–2–3, and its fiber orientation angle, ψ , by example of the top layer.

Chapter 1

Introduction

Laminates made of fiber reinforced polymers (FRPs) have become very popular in the past years. The increased usage originates from their weight saving potential which, in turn, comes from their high weight specific stiffness and their high weight specific strength.

Traditional fields where FRP laminates have been used for years are aeronautics and astronautics. Nowadays FRP laminates are used wherever light weight paired with requirements of high stiffness and high load carrying capacity is an issue. Typical products and components made of FRP laminates are maritime vessels, road vehicles, wind turbines, fast rotating shafts, tennis rackets, frames for bicycle, etc. A prominent example of the increased useage of FRP laminates is the Airbus A380. In this aircraft interior components, fairings, as well as structural parts such as wings and spoilers are made of FRP laminates (Middendorf, 2008). In total more than 20% of the structural weight is contributed by parts made from FRPs. For the next generation of aircrafts – like the Airbus A350XWB or the Boeing Dreamliner 787 – this percentage will even exceed 50% of the total structural weight.

FRP laminates have become popular for weight saving purposes, even though their potential is not fully tapped today. To further exploit the advantages of FRP laminates, reliable methods are required which can be used for the prediction of their mechanical response. The development of such methods is the main scope of the present work, whereby applicability within the framework of the finite element method (FEM) is of major interest in order to allow for the analyses of entire structures.

The constituents of FRP laminates, their hierarchical structure, as well as their failure behavior are briefly discussed in the following Sect. 1.1. Afterwards the scope of the present work is defined in more detail in Sect. 1.2.

1.1 Fiber reinforced laminates

A FRP is a composite material made of two constituents with a topology of matrix-inclusion type. This means that one of the constituents is topologically connected, i.e. the matrix, whereas the other one is distributed in the matrix, i.e. the fibers. As matrix materials polymers such as epoxy, polyester, or phenolic resins are often used in engineering applications. The fibers are typically made of carbon or glass with a diameter of a few micrometers. With respect to the arrangement of the fibers within the matrix various specifications have been developed; in the present work, however, only continuous and unidirectionally oriented (UD) fibers are considered. The fibers represent the reinforcement phase of the composite material since they possess high stiffness and strength in their axial direction compared to the matrix material.

In order to build up a laminate from FRPs, plies (layers) with a thickness of some hundred micrometers are formed and stacked on each other. As long as the fibers are oriented unidirectionally, such plies are usually termed tapes; they possess high stiffness and strength only in fiber direction. Owing to the layered assembly, laminates with tailored mechanical properties can be created in order to meet the specific design requirements. The layup can, thereby, range from unidirectional laminates, i.e. all plies have the same fiber orientation, to multidirectional laminates with quasi-isotropic (in-plane) behavior.

Figure 1.1 illustrates the hierarchical structure of FRP laminates which is represented by the micro-scale, i.e. the length scale of the fibers (≈ 0.01 mm), the meso-scale, i.e. the length scale of the individual plies (≈ 0.1 mm), and the macro-scale, i.e. the length scale of the whole laminate or component (> 1 mm).

With respect to modeling and simulation of the behavior of FRPs, approaches based on both micro-scale and meso-scale have been proposed. In micromechanical approaches the microscopic stress and strain fields are resolved. Due to this high level of detail such approaches possess limited applicability in structural analysis as they

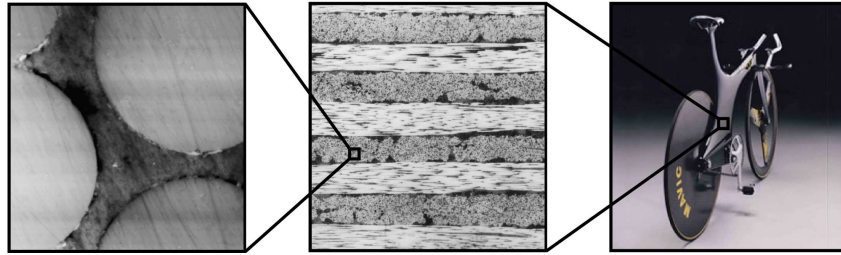


Figure 1.1: Hierarchical structure of FRP laminates; from the micro-scale, i.e. the length scale of the fibers (left), via the meso-scale, i.e. the length scale of the individual plies (middle¹⁾), towards the macro-scale, i.e. the length scale of the whole laminate or component (right)

are computationally expensive; furthermore, it is demanding to measure respective material and interface properties which are needed as model input. Nevertheless, micromechanical approaches are most useful to gain increased insight to the prevailing mechanisms. Within modeling approaches based on the meso-scale, i.e. ply-level models, the microscopic stress and strain fields are not resolved but a homogeneous ply material is modeled. As the gap to the macro-scale is rather easy to bridge, e.g. by the classical lamination theory, ply-level models are preferred in engineering applications.

Due to the hierarchical structure of conventional FRP laminates, two principle failure mechanisms are distinguished at the meso-scale. Failure of the interface between the plies is called inter-ply failure or delamination. Failure within the plies is called intra-ply failure. Intra-ply failure can be further classified in failure of the fibers, of the matrix, and of the interface between fiber and matrix. The latter two are typically not treated separately in ply-level models but are summarized as matrix dominated failure.

Within the present work only intra-ply failure is considered, i.e. perfect interfaces between the plies are assumed. Furthermore, attention is drawn to the ongoing process of material degradation which shall be termed progressive failure. The characteristics of such progressive failure of a unidirectionally reinforced ply strongly depends on its loading conditions.

¹⁾Picture taken from the paper by Nettles and Biss (1996).

If the ply is loaded by tensile stresses in fiber direction, failure is typically determined by fiber rupture. Note that first fiber breaks appear at much smaller stress levels compared to ultimate failure stress. The failure process, furthermore, involves fiber pull-out, debonding of fibers, etc. If the ply is loaded by compressive stresses in fiber direction, matrix failure due to tensile matrix stresses or fiber buckling and the formation of kink bands is observed. If the ply is loaded by tensile stresses in transverse direction, rather brittle failure mechanisms such as matrix cracking and fiber/matrix debonding are observed at the micro-scale. If the ply is loaded by in-plane shear stresses or by compressive normal stresses transverse to the fibers, interface failure and matrix shear failure determine the ultimate failure load. However, especially under shear loading considerable inelastic deformation is observed before ultimate failure occurs.

1.2 Scope of the present work

As already outlined, the present work focuses on modeling the mechanical response of UD FRP laminates with the superordinate objective to make appropriate FEM analyses of laminated components and structures possible.

To this end the following approach is chosen. First of all, the UD plies are modeled as homogeneous material, i.e. they (at least initially) are taken as transversely isotropic with the plane perpendicular to the fibers being the plane of material isotropy. Furthermore, perfect interfaces between the plies and plane stress states within the plies are assumed. The gap between the ply and laminate length scales is bridged by FEM via the intrinsic formulation of the elements that allow for layered section definitions.

Due to the outlined assumptions, it only remains to define a constitutive model for the ‘smeared out’ ply material, i.e. a constitutive model that associates stresses and the inelastic response to the strain history that the (homogeneous) ply material was subjected to. The development of such a constitutive model which accounts for non-linearity in the ply response caused by various phenomena is the scope of the present work. As it will be shown in detail in Chapter 3, the model thereby accounts for non-linearities induced by anisotropic stiffness degradation and induced by the accumulation of unrecoverable strains.

It must be noted that the constitutive model focuses on the response of plies which are embedded in laminates. Furthermore, the development of the constitutive model is not done in the framework of generalized standard materials but is motivated by engineering, phenomenological considerations. Since FEM is a state-of-the-art tool for structural analysis, the constitutive model is implemented as a user defined material within the commercial FEM package *Abaqus/Standard 6.9* (*Dassault Systèmes Simulia Corp., Providence, RI, USA*)

In order to assess the predictive capability of the proposed model, various case studies are considered. The respective predictions are compared to experimental results published in literature or to experimental results obtained by the *Polymer Competence Center Leoben GmbH (PCCL)* with specimens produced by *FACC AG*. The case studies are documented in Chapter 4. There also predictions are documented as being obtained for ‘part A’ of the third World Wide Failure Exercise (WWFE), even though the experimental results are not yet available.

Chapter 2

Literature review

In this chapter literature relevant for the present work is reviewed. In Sect. 2.1 some textbooks concerning the theories which provide the basis for the current work are recommended. In Sect. 2.2 the state-of-the-art and recent developments in modeling the behavior of UD FRP laminates are discussed. Since much research work has been published in the past decades and years, the literature review given here does not claim to be complete. Finally the failure criterion proposed by Puck is presented in Sect. 2.3 since some of his findings are crucial for the present work.

2.1 Recommended textbooks

Detailed information on FRPs, on the properties of typical matrix and fiber materials, and on the respective production processes can be found in the textbook by Schürmann (2005). The mechanics of composite materials including the classical lamination theory is discussed in the textbook by Jones (1999). More general basics of mechanics of materials can be found in the textbook by Mang and Hofstetter (2004). The finite element method is addressed in the textbook by Zienkiewicz and Taylor (2000). Elasticity theory, elastic anisotropy, and its tensorial formulation is treated in the textbook by Nye (1957). For information on plasticity theory the book by Lubliner (1990) can be consulted. The basics of damage mechanics are discussed in detail in the textbook by Lemaitre (1992). The treatment of damage mechanics and plasticity theory in the framework of FEM is addressed by the very comprehensive

lecture notes of Jirásek (2005). Computational aspects are considered in the book by Simo and Hughes (1998). Methods used in micromechanics and various formulations of mean field theories are discussed in the detailed lecture notes by Böhm (2004).

2.2 From FPF to continuum damage

First ply failure. Nowadays first ply failure (FPF) concepts are still state-of-the-art in practical engineering purposes. Such concepts assume that the laminate fails as soon as one of the individual ply stress states – estimated on basis of linear elastic ply material behavior – meets a certain failure criterion. The estimated FPF load is thereby given in terms of resultant forces and moments (or as multiplier thereof) as it is an attribute of the entire laminate in combination with the prevailing loading conditions. The advantages of FPF estimates lie in their simplicity and their low computational costs. Furthermore, they usually result in conservative failure load predictions.

Failure criteria used within FPF analysis range from the most simple maximum stress or maximum strain criterion to criteria that account for the interaction of stress components. The latter can be further classified in criteria that fit experimental data (e.g. Tsai-Hill or Tsai-Wu as documented by Jones (1999)) and such that fit experimental data with formulations motivated from physical failure mechanisms. A famous representative of the last group is the criterion developed by Puck (1996), whose findings were initiated by the work of Hashin (1980). The first WWFE has been introduced to judge the predictive capabilities of different failure criteria. It turned out that Puck's criterion is one of the most accurate methods currently available.

Continuum damage mechanics. First ply failure estimates are especially useful for initial design and optimization purposes. However, as soon as it is desired to tap the weight saving potential of FRPs, the nonlinear response affected by progressive failure is of interest. Accordingly, continuum damage mechanics have become popular for ply-level models of laminated composites.

Continuum damage mechanics was first introduced by Kachanov (1958) and Rabotnov (1969), whereby isotropic damage was modeled by scalar valued damage variables.

Following the documentation given by Lemaitre (1992), these concepts have been extended by Murakami (1981) to second-order damage tensors and by Chaboche (1978) to fourth-order damage tensors to model anisotropic damage. Note that the principle of separation of length scales should be fulfilled whenever continuum damage mechanics is applied, i.e. the characteristic length of the cracks must be sufficiently smaller than the length scale where the continuum is modeled. However, as the matrix crack length may possess the same magnitude as the ply thickness, the usage of continuum mechanics within ply-level models is not without controversy.

From the author's point of view also straightforward extensions of FPF analysis, where the ply stiffness properties are reduced selectively (Jones, 1999) or progressively degraded using degradation functions (e.g. Puck and Schürmann, 1998), can be ranked among continuum damage models. However, more sophisticated continuum damage models draw attention to thermodynamical consistency. A widely used model of the latter type has been proposed by a work group from Cachan (Allix et al., 1991; Ladevèze, 1991, 2001). Their model is based on energy potentials and accounts for intra-ply as well as inter-ply failure. The successful model has been adopted by many other authors. A model related to crack density has been proposed by Allen (1994) and Talreja (1994). Matzenmiller et al. (1995) have proposed a constitutive model that takes a FRP composite as an elastic-brittle continuum. The model accounts for different damage modes with emphasis on strain softening. With respect to the rate equations that define damage evolution, consistency with thermodynamics is addressed. Inspired by the work of Talreja, another continuum damage model has been introduced by Li et al. (1998). Based on the damage model originally proposed by Ladevèze, the effect of fiber rotation on the response of $[\pm 45]_S$ laminates is studied and modeled by Herakovich et al. (2000). Varna et al. (2001) have proposed a continuum damage model that includes also micromechanical considerations. With this model the stiffness degradation (including the change in the Poisson's ratio) caused by transverse matrix cracking is predicted successfully for various layups. A phenomenological model based on an unorthodox continuum damage approach has been proposed by Schuecker (2005) and Schuecker and Pettermann (2008a), where the anisotropic effect of damage is featured by a micromechanical method. The present work can be seen as an extension of the work of Schuecker. Predicting the in-situ strength of plies is addressed in the paper by Camanho et al. (2006). His findings are incorporated in the model proposed by Maimí et al. (2007a), where damage onset is

predicted on basis of the LaRC04 criterion. Effects of crack closure are incorporated in the model; the implementation is addressed in a separate paper (Maimí et al., 2007b). By Lapczyk and Hurtado (2007) another anisotropic damage model is presented that models the softening behavior of FRPs. Damage onset is predicted based on the criterion by Hashin (1980). Attention is drawn to the FEM appropriate implementation whereby mesh-adjusted softening and viscous regularization is utilized. The model is implemented within the FEM package *Abaqus*. With respect to strain softening the influence of the modeled shape of the used softening law is studied by Dávila et al. (2009). By Maimí et al. (2008) another continuum damage model is presented which is formulated at ‘sub-ply’ level, i.e. several elements are used through the ply thickness. The model accounts for inter-ply failure and its interaction with intra-ply failure and is able to predict periodical crack patterns. Models with special emphasis on compressive failure have been proposed e.g. by Basu et al. (2007) as well as Pineda et al. (2009), which both incorporate findings of Schapery (1995).

Pronounced inelasticity. Most of the models focussing on brittle damage mechanisms give reasonable predictions in particular when the plies are primarily loaded by transverse tensile stresses. However, when the loading conditions lead to high shear loading of the ply with respect to the principal material axes, pronounced inelastic behavior is observed. The experimental work published by Varna et al. (1999) considers damage accumulation in off-axis plies. The work implies that under loading conditions other than transverse tension the measured response cannot be explained by brittle cracking alone, i.e. mechanisms other than brittle ones are expected to become important. A similar conclusion can be drawn from the work by Lagattu and Lafarie-Frenot (2000). By means of experimental investigations it is stated that neither the evolution of matrix cracks nor variations in the micro structure can explain the pronounced nonlinear response of FRPs to shear loading. Further experimental work concerning shear loading has been published by Van Paepegem et al. (2006a). There, $[\pm 45]_{2S}$ laminates have been subjected to uniaxial tension and evidence was found for unrecoverable shear strain accumulation and degradation of the shear modulus.

The experimental work by Vogler and Kyriakides (1999) focuses on loading conditions that lead to combinations of shear loading with transverse compression. The

experimental observations imply that the effects of plastic mechanisms are important also in the case of transverse compression. Respective micromechanical simulations conducted by Hsu et al. (1999), in which two different plasticity models for the matrix material have been used, were able to explain some of the experimental observations. The numerical approach utilized by Totry et al. (2008) allowed to predict the failure locus measured by Vogler and Kyriakides. Further micromechanical simulations concerning transverse compression were performed by González and LLorca (2007), where the effect of interface failure as well as the formation of matrix shear bands has been studied.

In accordance with the above described findings, such pronounced non-linearity has been addressed by several models. For example the model proposed in the paper by Van Paepegem et al. (2006b) considers the nonlinear response observed when $[\pm 45]_{2S}$ specimens are subjected to tension. In the model two state variables have been introduced which represent the degradation of shear modulus and accumulation of unrecoverable shear strain. Another model accounting for stiffness degradation as well unrecoverable strain accumulation has been proposed by Barbero and Lonetti (2002). The accumulation of unrecoverable strains is related to the considerations of Puck for brittle failure by Schuecker and Pettermann (2008b) and Schuecker et al. (2008). In the latter work the model predictions are furthermore compared to experiments published by Varna et al. (1999).

Coupling of damage and plasticity. As the coupling of damage and plasticity within a single constitutive model is not straightforward, this topic has been addressed by several authors not only in the context of FRP composites. By Armero and Oller (2000) a general framework for coupling of damage with plasticity has been presented. In the model proposed by Hansen et al. (2001) two independent formulations for anisotropic damage and plasticity in concrete are proposed and result in a two-surface formulation. Furthermore, they give some usefull remarks considering the implementation. By Grassl and Jirásek (2006) special attention is drawn to thermodynamic aspects as well as uniqueness. In this context uniqueness implies that every thinkable strain history leads to an unique stress history which is determined by the constitutive equations.

2.3 Puck's failure criterion

In the first WWFE organized by Hinton et al. (2004), it turned out that the failure criterion proposed by Puck (1996), which was later revised by Schürmann (2005) and Knops (2008), is one of the most accurate criteria currently available. Crucial assumptions of the constitutive model, which is presented in the present work, are related to Puck's findings for brittle failure in transversely isotropic, fiber reinforced composite materials. Since plane stress states are treated exclusively at present, the criterion suitable for plane stress states is reviewed only.

The Puck criterion distinguishes between fiber failure (FF) and matrix dominated failure (MDF), i.e. inter fiber failure in terminology of Puck. Within the Puck criterion FF is evaluated by a simple maximum stress criterion. This means that for this type of failure only the stress component in fiber direction is expected to be relevant. The Puck criterion is more specialized on the prediction of MDF, where MDF is viewed as brittle failure leading to fracture in a plane parallel to the fiber direction. The orientation of the fracture plane is defined by the fracture plane angle, φ , as shown in Fig. 2.1. As it is summarized by Schürmann (2005), the Puck criterion utilizes Mohr's fracture hypothesis to evaluate MDF. Mohr's fracture hypothesis has been developed for brittle metals and was firstly applied to UD composites by Hashin (1980). The hypothesis suggests that failure occurs in that material plane which offers the lowest failure resistance against the tractions acting on the plane. To judge whether or not a potential fracture plane fails, Puck introduces a 'master failure surface'. This surface is defined in terms of the fracture plane tractions which are described in the fracture plane coordinate system, $l-n-t$, cf. Fig. 2.1. This way, critical ply load levels as well as critical fracture planes can be determined, and a failure surface for MDF is derived in $\sigma_{22}-\sigma_{12}$ ply stress space. Although the stresses in fiber direction have no influence on the fracture plane tractions, weakening factors are proposed in order to down-scale the failure surface at high longitudinal stresses. Considering FF and MDF including the weakening factors, a failure surface is defined in $\sigma_{11}-\sigma_{22}-\sigma_{12}$ stress space, which can be formally written as

$$F_P = F_P [\sigma_{11}, \sigma_{22}, \sigma_{12}] = 0 . \quad (2.1)$$

For the definition of the failure surface, the five nominal strength values, $X^{(t)}$, $X^{(c)}$, $Y^{(t)}$, $Y^{(c)}$, and S , two slope parameters, $p^{(t)}$ and $p^{(c)}$, and two weakening parameters, s

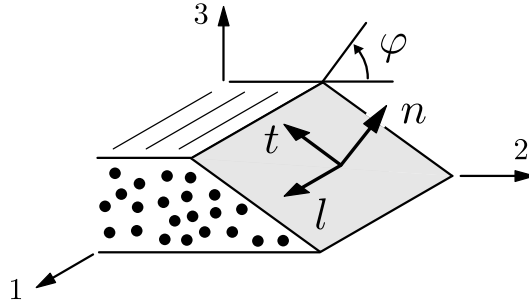


Figure 2.1: Definition of the fracture plane coordinate system, $l-n-t$, with respect to the ply coordinate system, $1-2-3$; definition of the fracture plane angle, φ .

and m , are needed. Here X is the nominal strength in fiber direction, Y is the nominal strength in (in-plane) transverse direction, and S is the nominal (in-plane) shear strength. Furthermore, the superscripts (t) and (c) refer to tensile and compressive loading conditions, respectively. Note that only two slope parameters are listed as ‘parametric coupling’ (Schürmann, 2005) is used. The equations which define Puck’s failure surface are summarized in Appendix B.

When failure is predicted, the Puck criterion provides – unlike to commonly used failure criteria – information about the orientation of the expected fracture plane. When the composite material is subjected to combinations of in-plane shear loads and transverse tensile or moderate transverse compressive loads, a fracture plane angle of $\varphi = 0$ is predicted (i.e. mode A and mode B in Puck’s terminology). In case of dominant transverse compression, fracture is predicted on inclined planes with $\varphi \neq 0$, (i.e. mode C in Puck’s terminology). In the latter case, both orientations $+\varphi$ and $-\varphi$ are equally likely to occur under plane stress conditions.

Chapter 3

The constitutive model

In the following a constitutive model for the smeared out ply material is presented. Note that plies which are embedded in a laminate are considered only. The development of the model was done under plane stress assumption as typically applicable in the analysis of laminated, thin-walled components and structures.

During loading of a laminate various phenomena may occur within the plies leading to a pronounced nonlinear response. Here not all the individual phenomena are distinguished in detail since their effects are modeled in an averaged sense. Nevertheless, in the context of material modeling at least two major types of effects should be distinguished due to their opposed characteristics. These two types are, first, stiffness degradation and, second, the accumulation of unrecoverable strains.

Stiffness degradation is attributed to microscopic brittle matrix cracking, fiber matrix debonding, and progressive fiber failure. Such phenomena are expected to lead to a decreased stiffness primarily, but corresponding strains are taken to be recoverable after unloading. Accordingly, they are termed elastic strains (superscript ‘el’) even though the underlying material behavior is non-conservative. Within the present work stiffness degradation is modeled by brittle continuum damage mechanics, i.e. by elasto-damage, but consists of two separate approaches. The first one deals with the stiffness degradation due to evenly distributed, matrix dominated phenomena. Here strain hardening is modeled as no damage localization is expected. Accordingly, the respective model concept, which was originally proposed by Schuecker and Pettermann (2006, 2008a), is denoted as ‘distributed brittle damage’.

It is presented with some modifications in Sect. 3.1. The second approach deals with stiffness degradation triggered by localized matrix dominated as well as fiber dominated phenomena. In contrast to before, strain softening is modeled leading to damage and strain localization in structural analysis. The respective model concept is denoted as ‘localized brittle damage’, which is presented in Sect. 3.3.

The accumulation of unrecoverable strains is associated to inelastic, microscopic matrix deformation. Such phenomena are accompanied by residual deformations of the specimen after unloading, e.g. observed in experimental testing when the load on the laminate induces pronounced in-plane shear stresses¹⁾ in the plies. In the following unrecoverable strains are referred to as plastic strains (superscript ‘pl’) since their evolution is described by a multi-surface plasticity model presented in Sect. 3.2.

As already outlined, the present constitutive model concerns stiffness degradation as well as plastic strain accumulation. For the purpose of their combination in a single material model, the elasto-damage model concerning stiffness degradation is enriched by the model treating the evolution of plastic strains. Accordingly, after integration of the loading history, the mechanical strain is composed of an elastic as well as a plastic contribution and reads

$$\underline{\boldsymbol{\varepsilon}} = \underline{\boldsymbol{\varepsilon}}^{(\text{el})} + \underline{\boldsymbol{\varepsilon}}^{(\text{pl})} = \underline{\underline{\mathbf{C}}} \underline{\boldsymbol{\sigma}} + \underline{\boldsymbol{\varepsilon}}^{(\text{pl})} . \quad (3.1)$$

Here $\underline{\boldsymbol{\varepsilon}}$ denotes the vector of mechanical strain components, i.e. the total strains minus thermal strains, $\underline{\boldsymbol{\varepsilon}}^{(\text{el})}$ denotes the vector of elastic strain components, and $\underline{\boldsymbol{\varepsilon}}^{(\text{pl})}$ is the vector of accumulated plastic strain components. The matrix $\underline{\underline{\mathbf{C}}}$ is the current compliance matrix of the possibly damaged ply material, and $\underline{\boldsymbol{\sigma}}$ denotes the vector of stress components. In Eqn. (3.1), both the compliance matrix of the ply material as well as the vector of plastic strain components contribute to the non-linearity of the ply behavior. The evolution of $\underline{\underline{\mathbf{C}}}$ and $\underline{\boldsymbol{\varepsilon}}^{(\text{pl})}$ as functions of the stress and strain history is described by separate phenomenological, incremental formulations.

Some crucial assumptions used in the constitutive model are based on Puck’s findings for brittle failure. Note that Puck’s criterion was reviewed in Sect. 2.3, and the equations, which describe Puck’s failure surface in the form $F_P [\sigma_{11}, \sigma_{22}, \sigma_{12}] = 0$, are given in Appendix B. Within the constitutive model the material exertion, which governs the damage evolution for matrix dominated failure modes, is assessed with

¹⁾with respect to the local ply coordinate system, i.e. the principal material axes;

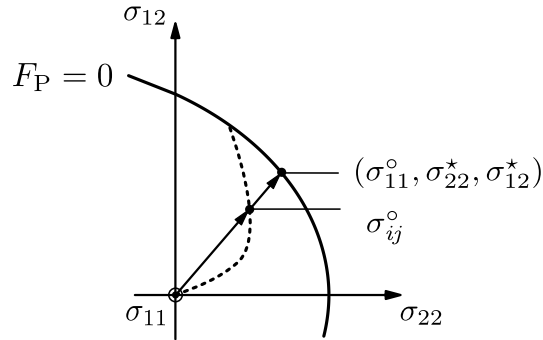


Figure 3.1: Sketch of the stress states which are needed for the definition of the factor of matrix exertion, $f_E^{(m)}$, with respect to Puck's failure surface.

recourse Puck's failure surface for plane stress states. To this end, a scalar valued factor of matrix exertion, $f_E^{(m)}$, is introduced which is independent of the loading history but depends on the current stress state only. It is computed with respect to Puck's failure surface, $F_P = 0$, from

$$\begin{pmatrix} \sigma_{22}^{\circ} \\ \sigma_{12}^{\circ} \end{pmatrix} = f_E^{(m)} \begin{pmatrix} \sigma_{22}^{\star} \\ \sigma_{12}^{\star} \end{pmatrix}, \quad (3.2)$$

where σ_{ij}° are the stress components to be assessed and the stress components σ_{22}^{\star} and σ_{12}^{\star} are computed as depicted in Fig. 3.1 so that $F_P[\sigma_{11}^{\circ}, \sigma_{22}^{\star}, \sigma_{12}^{\star}] = 0$ holds. In order to assess the fiber exertion, the factor of fiber exertion, $f_E^{(f)}$, is defined as

$$f_E^{(f)} = \max \left[\frac{\sigma_{11}}{X^{(t)}}, \frac{-\sigma_{11}}{X^{(c)}} \right] \quad (3.3)$$

with the nominal ply strength in fiber direction under tension, $X^{(t)}$, and under compression, $X^{(c)}$. Besides the material exertion, the fracture plane orientation predicted by Puck is used to identify the active damage mechanism in the present model. This is done, although – strictly speaking – the predicted orientation is only meaningful when the stress state meets the failure criterion, i.e. when $F_P[\sigma_{11}, \sigma_{22}, \sigma_{12}] = 0$ holds.

3.1 Distributed brittle damage

Within the present constitutive model the stiffness degrading effect of matrix dominated phenomena such as microscopic matrix cracking and fiber matrix debonding is modeled by continuum damage mechanics. Since respective strains are taken to be recoverable after unloading, the model can be seen as an elasto-damage approach which describes material behavior affected by progressive, fully brittle damage. Here the effect of evenly distributed phenomena is addressed. Accordingly, strain hardening is accompanied by damage evolution rather than strain softening behavior which would lead to damage and strain localization in structural analyses. Considering all these facts, this model part is referred to as ‘distributed brittle damage’.

The challenge in the formulation of a continuum damage model for FRP composites is to capture the anisotropic, i.e. direction dependent characteristics of damage by using only few, preferably scalar valued damage variables. Furthermore, the evolution of damage has to be related to the ply loading history for which an infinite number of realizations exist.

With the outlined challenge in mind, it was stated by Schuecker and Pettermann (2006) that the effect of matrix dominated phenomena on the material stiffness can be imitated by embedding fictitious inhomogeneities into the undamaged but smeared out ply material. The resulting fictitious material is then utilized in combination with a method borrowed from micromechanics in order to predict the fourth order elasticity tensor of the damaged ply. With this modeling technique, which is also used in the present work, the anisotropic nature of damage is incorporated naturally.

It is important to stress that the fictitious inhomogeneities are not intended to represent actual cracks. Accordingly, this rather unorthodox approach is not a micromechanical investigation of a damaged composite ply. Nevertheless, the incorporated damage variables can be interpreted as (i) the shape, (ii) the volume fraction, (iii) the orientation, and (iv) the assigned material properties of the fictitious inhomogeneities. These variables, which govern both the effect and the evolution of damage, are discussed next.

(i) The fictitious inhomogeneities are oblate spheroids with the axis of rotation aligned to the fracture plane normal n , cf. Fig. 2.1. Their shape is described by the aspect ratio $e^{(m)}$. This scalar variable basically sets the anisotropic characteristics of the modeled damage behavior. If $e^{(m)} = 1$ is chosen, the inhomogeneities are spheres and the Young's modulus in transverse direction and the in-plane shear modulus are equally degraded with respect to the properties of the undamaged material. If $e^{(m)} \ll 1$ is chosen, the degradation of Young's modulus in transverse direction exceeds the degradation of the in-plane shear modulus while the Poisson ratio increases slightly during damage accumulation. Comparison with experimental results, e.g. published by Varna et al. (1999, 2001), shows that penny-shaped voids with a small aspect ratio $e^{(m)}$ are suited to capture the anisotropic nature of damage correctly.

(ii) The volume fraction $\xi^{(m)}$ stands for that volume of fictitious inhomogeneities per volume ply material which are embedded in order to model the effect of matrix dominated phenomena. Since this variable represents the amount of damage, it has to be related to the ply loading. For this purpose a simple evolution equation is postulated for which it is assumed that the amount of damage is only related to the matrix exertion. Furthermore, it is assumed that no damage accumulates before a factor of matrix exertion of $f_E^{(m)} = 1$ is predicted. Finally the amount of damage $\xi^{(m)}$ is estimated for $f_E^{(m)} > 1$ by

$$\xi^{(m)} = k_d^{(m)} \left(f_E^{(m)} - 1 \right)^2, \quad (3.4)$$

The evolution parameter $k_d^{(m)}$ has to be calibrated from experimental data together with the aspect ratio $e^{(m)}$. Note that in multi-directional laminates $f_E^{(m)}$ is expected to take values only slightly larger than 1 since an increasing exertion factor produces additional damage quickly, which itself has a feedback on the prevailing ply stresses.

(iii) If damage accumulates under loading conditions for which Puck predicts a fracture plane with a fracture plane angle of $\varphi = 0$, the axis of rotation of the penny-shaped inhomogeneities is defined to be parallel to the in-plane transverse direction of the ply. The respective population of inhomogeneities is referred to as population 2 with volume fraction ξ_2 , and the damage mechanism is referred to as d_I . However, under uniaxial transverse compression, the Puck criterion predicts fracture planes

with a fracture plane angle of $\varphi = \pm\phi$, where the sign is undetermined under plane stress conditions (see Schürmann, 2005). In order to account for such inclined fracture planes, two further populations 3 and 4 are incorporated with the volume fractions ξ_3 and ξ_4 , respectively. The axis of rotation of the inhomogeneities of population 3 is modeled as being parallel to the n -axis of the fracture plane coordinate system at $\varphi = -\phi$. The same holds true for inhomogeneities of populations 4 but $\varphi = +\phi$ is used. Since both fracture plane angles $\varphi = -\phi$ and $\varphi = +\phi$ are equally likely to occur, $\xi_3 = \xi_4$ is set. The damage mechanism focusing on the effect of inclined cracking is referred to as d_{II} . Under more general loading conditions, fracture plane angles are predicted for which $0 \geq |\varphi| \geq \phi$ hold. To account for such situations, the amount of damage $\xi^{(m)}$ computed from Eqn. (3.4) is divided into the volume fractions ξ_p with $p = 2, 3, 4$ depending on the ratio $\beta = |\varphi|/\phi$. The volume fractions finally read

$$\xi_2 = (1 - \beta) \xi^{(m)} \quad \text{and} \quad \xi_3 = \xi_4 = \beta \xi^{(m)} / 2. \quad (3.5)$$

The orientation of the incorporated populations of inhomogeneities is sketched in Fig. 3.2. Also the division of amount of damage, $\xi^{(m)}$, with respect to the individual volume fractions is illustrated.

Up to now, monotonic loading conditions with unchanging fracture plane angles have been assumed (implicitly). In order to allow for arbitrary, also non-radial loading paths and to assure non-decreasing volume fractions,

$$\bar{\xi}_p = \max(\xi_p(\tau)) \quad (3.6)$$

is employed, where τ represents the exertion history and $\bar{\xi}_p$ are the volume fractions finally used for the stiffness computation. With Eqn. (3.6) the actual volume fraction $\bar{\xi}_p$ is given as the maximum of the volume fraction ξ_p predicted during the whole loading history. This way, accumulated damage remains present also when the matrix exertion is reduced, e.g. during unloading. Even though the difference between $\bar{\xi}_p$ and ξ_p is essential in the context of material modeling, the diacritic is omitted for sake of simplicity in the following.

(iv) The material properties actually assigned to the inhomogeneities depend on the current ply stress state. Under transverse tensile loads the inhomogeneities are modeled as voids, i.e. the elasticity tensor of the inhomogeneities is set to $\mathbf{E}^{(p)} \rightarrow \mathbf{0}$.

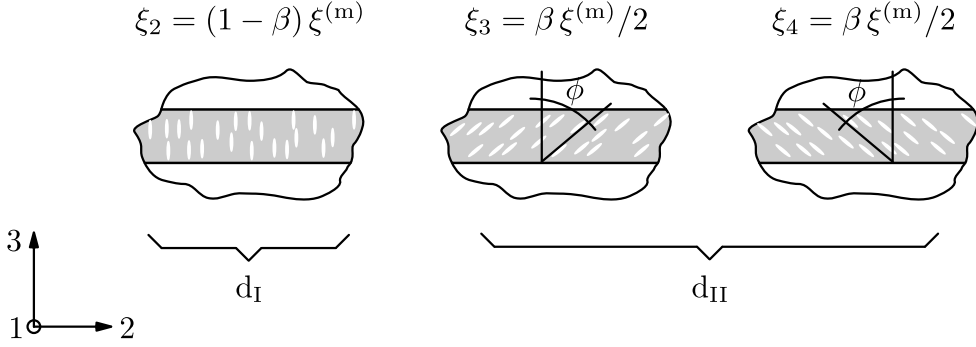


Figure 3.2: Orientation of the incorporated populations of inhomogeneities for mechanism d_I and d_{II} ; division of $\xi^{(m)}$ with respect to the individual volume fractions ξ_2 , ξ_3 , and ξ_4 .

Under transverse compressive loads a damaged composite may recover some stiffness as e.g. documented by Soden et al. (1998). This effect is captured in the model by assigning isotropic material properties to the fictitious inhomogeneities. Thereby, the young's modulus is defined as

$$E^{(p)} = E_2^{(0)}, \quad (3.7)$$

whereas the shear modulus $G^{(p)}$ is defined depending on the actual fracture plane normal tractions $\sigma_{nn}^{(p)} < 0$ in order to account for frictional effects. The shear modulus reads

$$G^{(p)} = \min \left[-\mu_d \sigma_{nn}^{(p)}, G_{12}^{(0)} \right]. \quad (3.8)$$

Here μ_d is a parameter similar to the one introduced by Schuecker and Pettermann (2006); the superscript (0) denotes undamaged ply properties. Note that the normal tractions $\sigma_{nn}^{(p)}$ are determined with respect to the fracture plane that corresponds to the population p .

The populations of fictitious inhomogeneities, once defined by their shape, their volume fractions, their orientations, and their material properties, are used to derive the fully tri-axial compliance tensor \mathbf{C} of the damaged ply material. To this end, a Mori-Tanaka-like method known from mechanics of materials (see e.g. Böhm, 2004) is used. Accordingly, the compliance tensor of the fictitious material containing p populations of inhomogeneities reads

$$\mathbf{C} = \left(\mathbf{I} + \sum_p \mathbf{D}^{(p)} \right) \mathbf{C}^{(0)}, \quad (3.9)$$

where $\mathbf{C}^{(0)}$ is the compliance tensor of the undamaged ply material and \mathbf{I} stands for the symmetric fourth order identity tensor. The tensor $\mathbf{D}^{(p)}$ denotes a fourth order tensor associated to the population p which reads

$$\mathbf{D}^{(p)} = -\xi_p \left[\left(\mathbf{E}^{(p)} - \mathbf{E}^{(0)} \right) \left(\mathbf{S}^{(p)} - \xi \left(\mathbf{S}^{(p)} - \mathbf{I} \right) \right) + \mathbf{E}^{(0)} \right]^{-1} \left(\mathbf{E}^{(p)} - \mathbf{E}^{(0)} \right) . \quad (3.10)$$

The quantity ξ_p stands for the volume fraction of the considered population p , whereas the quantity ξ denotes the total volume fraction of all inhomogeneities. Furthermore, $\mathbf{S}^{(p)}$ is Eshelby tensor associated to population p which has to be evaluated numerically (Gavazzi and Lagoudas, 1990). If inhomogeneities with zero stiffness are considered, Eqn. (3.10) reduces to

$$\mathbf{D}^{(p)} = \frac{\xi_p}{1 - \xi} \left[\mathbf{I} - \mathbf{S}^{(p)} \right]^{-1} . \quad (3.11)$$

The Eqns. (3.9) and (3.10) are derived in Appendix D. Note that all the tensors used in this section have to be defined with respect to the ply coordinate system. Information on coordinate transformations of the matrix representations can be found in Appendix E.

3.2 Multi-surface plasticity

In the section before the nonlinearity in the ply response originating from a degrading stiffness was treated. However, stiffness degradation is definitely not the only possible source for nonlinear ply behavior since also unrecoverable strains may accumulate. The existence of such unrecoverable strains can be demonstrated in experimental testing by introducing unloading loops in the test program.

Figure (3.3) shows two force–displacement curves obtained at the *PCCL*. In Fig. 3.3 (left) the response of a $[(\pm 45^\circ)_n]_S$ to uniaxial tension is documented in terms of applied force, F , versus displacement, u . Note that this experimental setup mainly induces (in-plane) shear stresses in the plies. The unloading and reloading loops which are also shown in Fig. 3.3 give rise to the assumption that the major part of the observed nonlinearity originates from unrecoverable strain accumulation.

In Fig. 3.3 (right) the response of an UD laminate to transverse compression is given again in terms of applied force, F , versus displacement, u . The measured unloading and reloading loops point out that the unrecoverable strain accumulation is of major importance also for transverse compressive loading conditions.

To model the ply response shown in Fig. 3.3 exclusively by elasto-damage may lead to a correctly predicted nonlinearity; however, the underlying mechanism would not be captured by such a model. Accordingly, in the present constitutive model unrecoverable strain accumulation and the nonlinear ply response accompanied therewith is modeled by a plasticity model. Its phenomenological formulation is presented next; its calibration is addressed in Sect. 3.5.

Within the criterion proposed by Puck (1996), failure is attributed to brittle mechanisms. Nevertheless, the present model assumes that plastic shear strains are driven by tractions acting on planes which are similarly oriented as Puck’s fracture planes. These planes are referred to as ‘shear planes’ in the following. According to such a driving mechanism, a model would be desired which is formulated with respect to tractions acting on the shear planes. However, such a formulation is demanding since the orientation of the shear planes is unknown and expected to change during loading. In order to circumvent these difficulties, a phenomenological plasticity law is developed with respect to the ply coordinate system, but the driving mechanism is kept in mind when the model is formulated. The phenomenological model assumes

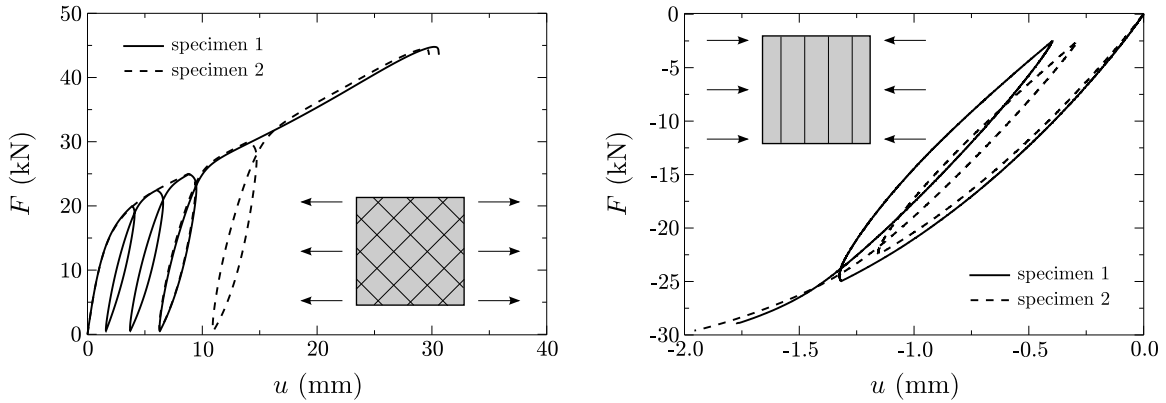


Figure 3.3: Loading, unloading, and reloading of a $[(\pm 45^\circ)_n]_S$ by uniaxial tension (left); loading, unloading, and reloading of an UD laminate by uniaxial transverse compression (right); responses are given in terms of applied force, F , versus displacement, u ; experimental data obtained by the PCCL.

that the evolution of plastic strains can be modeled by two plasticity mechanisms, referred to as p_I and p_{II} , respectively. Each mechanism is assigned to a specific type of shear plane and is primarily driven by a characteristic shear stress component. Furthermore, each mechanism is designed to represent the evolution of a characteristic plastic shear strain component which accumulates on the considered type of shear plane.

By this approach each mechanism can be formulated on its own very similar to the simple and classical one-dimensional, rate independent plasticity (Simo and Hughes, 1998). However, under general loading conditions both mechanisms can be active simultaneously.

Mechanism p_I – in-plane shear. Mechanism p_I concerns the nonlinear ply behavior observed under dominant ply shear loads. Under such loading conditions the Puck criterion predicts a non-inclined fracture plane with $\varphi = 0$ as sketched in Fig. 3.4 (left). Accordingly, it is assumed that plastic shear strains $\gamma_{12}^{(pl)}$ accumulate on such non-inclined shear planes. In the formulation of mechanism p_I , the shear stress component σ_{12} is modeled as the major driving force but also influence of the normal stress component σ_{22} on the evolution of plastic shear strains is considered. Finally

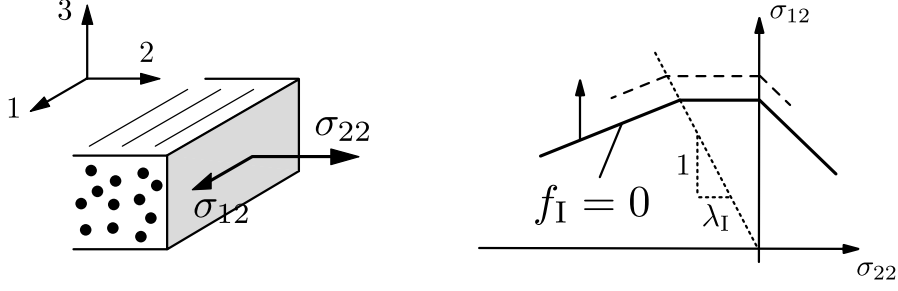


Figure 3.4: Sketch of the ‘shear plane’ of mechanism p_I (left); yield surface of mechanism p_I defined in σ_{22} - σ_{12} stress space (right).

mechanism p_I is defined with respect to the ply coordinate system by a yield surface, a flow rule, and a hardening behavior, but note that their derivation is not based on energy principles.

In Fig. 3.4 (right) the yield surface of mechanism p_I is sketched. The corresponding yield condition reads

$$f_I = \sigma_I - \tilde{\sigma}_I = 0, \quad (3.12)$$

where σ_I stands for the equivalent shear stress and $\tilde{\sigma}_I$ stands for the yield stress. The equivalent shear stress, σ_I , is defined for $\sigma_{12} \neq 0$ by

$$\sigma_I = \begin{cases} |\sigma_{12}| + \mu_I^{(t)} \sigma_{22} & r_I < 0 \\ |\sigma_{12}| & 0 \leq r_I \leq \lambda_I \\ |\sigma_{12}|(1 - \mu_I^{(c)} \lambda_I) - \mu_I^{(c)} \sigma_{22} & \lambda_I < r_I \end{cases} \quad (3.13)$$

with a stress ratio $r_I = -\sigma_{22}/|\sigma_{12}|$ and stress interaction parameters $\mu_I^{(t)}$, $\mu_I^{(c)}$, and λ_I . Regarding the modeled stress interaction, transverse tensile stresses increase the equivalent shear stress. Transverse compressive stresses up to a stress ratio of $r_I \leq \lambda_I$ do not contribute to the equivalent shear stress, whereas transverse compressive stresses satisfying $r_I > \lambda_I$ are again expected to increase the equivalent shear stress. Note that the stress component in fiber direction, σ_{11} , has no influence on mechanism p_I . The yield stress $\tilde{\sigma}_I$ is given by

$$\tilde{\sigma}_I = \begin{cases} \tilde{\sigma}_I^{(0)} + c_I \kappa_I & \kappa_I < \kappa_I^* \\ k_I (\kappa_I)^{n_I} & \kappa_I \geq \kappa_I^* \end{cases}, \quad (3.14)$$

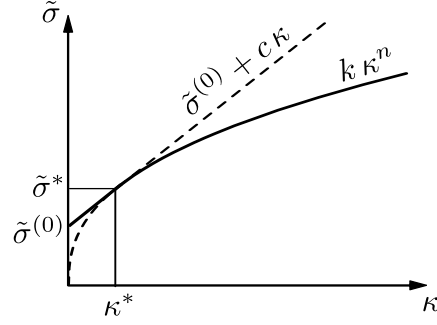


Figure 3.5: Yield stress $\tilde{\sigma}$ as function of the internal hardening variable κ .

i.e. by a Ludwik type power law which allows for a non-zero initial yield stress $\tilde{\sigma}_I^{(0)}$. Here the variable κ_I is the internal hardening variable and κ_I^* denotes the hardening where the linear law meets the power law. Furthermore, c_I is the slope in the linear region of the yield stress and k_I as well as n_I denote the power law parameters. The relation Eqn. (3.14), which is able to describe the measured hardening under pure shear loading very well, is sketched with omitted indices in Fig. 3.5. The hardening behavior itself is modeled to be linear in the amount of plastic flow, i.e. the evolutionary equation $\dot{\kappa}_I = |\dot{\gamma}_{12}^{(pl)}|$ holds for the internal hardening variable κ_I . Furthermore, a non-associated flow rule is proposed since mechanism p_I only treats the accumulation of plastic ply shear strains $\gamma_{12}^{(pl)}$. This flow rule reads

$$\dot{\gamma}_{12}^{(pl)} = \dot{\Lambda}_I \text{sign}[\sigma_{12}] , \quad (3.15)$$

where $\dot{\Lambda}_I \geq 0$ is the rate at which the plastic flow takes place. Considering all the descriptive equations given so far, the resulting hardening law reads $\dot{\kappa}_I = \dot{\Lambda}_I$.

Mechanism p_{II} – transverse compression. Mechanism p_{II} concerns the nonlinear ply behavior observed under dominant transverse compressive ply loads. Under such loading conditions the Puck criterion predicts an inclined fracture plane with $\varphi \neq 0$ as indicated in Fig. 3.6 (left). Accordingly, it is assumed that plastic shear strains $\gamma_{nt}^{(pl)}$ accumulate on inclined shear planes primarily driven by the shear stress component σ_{nt} . However, the stress components σ_{nn} and σ_{ln} are expected to influence the evolution of plastic shear strains. In order to avoid complex model formulations originating from the unknown orientation of the inclined planes, the outlined fea-

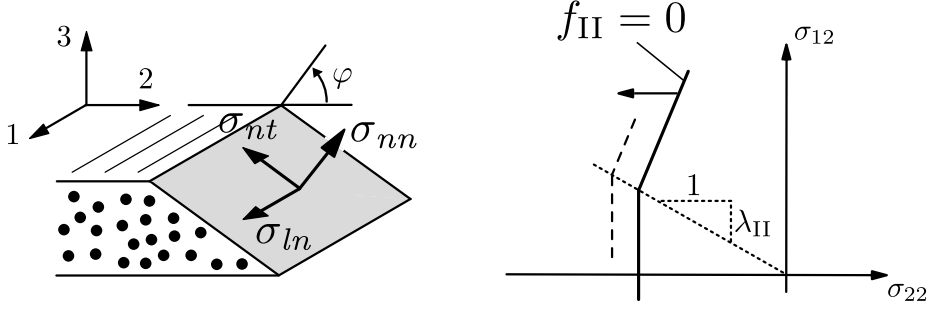


Figure 3.6: Sketch of the ‘shear plane’ of mechanism p_{II} (left); yield surface of mechanism p_{II} defined in σ_{22} - σ_{12} stress space (right).

tures are pooled together and modeled by mechanism p_{II} , which is again defined with respect to the ply coordinate system.

The respective yield surface is sketched in Fig. 3.6 (right). The yield condition reads

$$f_{II} = \sigma_{II} - \tilde{\sigma}_{II} = 0, \quad (3.16)$$

where σ_{II} is the equivalent compressive stress and $\tilde{\sigma}_{II}$ is the yield stress of mechanism p_{II} . The equivalent compressive stress, σ_{II} , is defined for $\sigma_{22} < 0$ by

$$\sigma_{II} = \begin{cases} -\sigma_{22} & r_{II} \leq \lambda_{II} \\ -\sigma_{22}(1 - \mu_{II}\lambda_{II}) + \mu_{II}|\sigma_{12}| & r_{II} > \lambda_{II} \end{cases} \quad (3.17)$$

with a stress ratio $r_{II} = -|\sigma_{12}|/\sigma_{22}$ and stress interaction parameters λ_{II} and μ_{II} . Regarding the modeled stress interaction, shear stresses satisfying $r_{II} > \lambda_{II}$ increase the equivalent compressive stress. For the definition of the yield stress $\tilde{\sigma}_{II}$ an relation equivalent to Eqn. (3.14) is used, whereby the internal hardening variable κ_{II} , the initial yield stress, $\tilde{\sigma}_{II}^{(0)}$, and the power law parameters k_{II} and n_{II} are introduced. The hardening behavior of mechanism p_{II} is modeled by the simple evolutionary equation $\dot{\kappa}_{II} = |\dot{\varepsilon}_{22}^{(pl)}|$. Here $\varepsilon^{(pl)}$ denotes the plastic in-plane transverse strain. Since mechanism p_{II} only treats plastic strains $\gamma_{nt}^{(pl)}$ and since both shear plane orientations $\pm\varphi$ occur, the flow rule defined with respect to the ply coordinate system reads

$$\begin{aligned} \dot{\varepsilon}_{22}^{(pl)} &= \dot{\Lambda}_{II}(-1), \\ \dot{\varepsilon}_{33}^{(pl)} &= \dot{\Lambda}_{II}(+1), \end{aligned} \quad (3.18)$$

where $\dot{\Lambda}_{II} \geq 0$ is the rate at which the plastic flow takes place. For mechanism p_{II} the resulting hardening law reads $\dot{\kappa}_{II} = \dot{\Lambda}_{II}$.

Interaction of the modeled mechanisms. The plastic ply behavior is modeled by separate plasticity mechanisms, each of which is defined by a yield condition, a flow rule, and a hardening law. Note that the respective loading–unloading conditions and consistency conditions, which are needed to complete the definition of the plasticity mechanisms, are left out for sake of brevity.

With respect to the implementation a standard algorithm based on elastic predictor/plastic corrector technique (Simo and Hughes, 1998) can be utilized to solve for the plastic strain increment as long as only one mechanism is active. However, elastic trial stresses which lead to $f_I > 0$ and $f_{II} > 0$ give rise to the assumption that both mechanisms are active. Accordingly, the full system of equations is considered which consists of – among others – two yield conditions and two flow rules. After convergence of the integration scheme which is based on a backward Euler method, it has to be checked if the found solution is admissible. This is done by checking whether or not the rates of the internal hardening variables of the active mechanisms are all non-negative. Also it needs to be checked whether or not the yield condition of a non-active mechanism is still not met. If the solution is found to be non-admissible, the assumption regarding the active mechanisms was wrong and the procedure has to be repeated with a modified set of active mechanisms. Finally the total rate of the plastic strain components reads

$$\dot{\underline{\epsilon}}^{(pl)} = \dot{\underline{\epsilon}}_I^{(pl)} + \dot{\underline{\epsilon}}_{II}^{(pl)} , \quad (3.19)$$

which accounts for the two contributions $\dot{\underline{\epsilon}}_I^{(pl)}$ and $\dot{\underline{\epsilon}}_{II}^{(pl)}$ from the individual mechanisms p_I and p_{II} , respectively.

3.3 Localized brittle damage

The model presented so far attributes the non-linearity in the response of laminates to the evenly degrading elastic ply properties and to the accumulation of plastic ply strains. It gives reasonable predictions as long as the ultimate load that is bearable by the plies is not reached. If the load on the laminate is increased sufficiently, heavily disintegrated material or even the formation of discrete cracks is expected locally. Such phenomena, which shall be termed as ‘localized failure’ in the following, are not incorporated in the model presented so far.

Within FEM analysis of structures modeling of localized failure is of great interest because it often determines the ultimate load which is bearable by a component. Accordingly, in the context of localized failure it is not sufficient anymore to focus on matrix dominated phenomena alone as a major part of the load is usually carried by the fibers. In order to incorporate localized failure within the present constitutive model, the effect of localized failure is taken as local stiffness degradation accompanied by strain softening behavior. Since such stiffness degradation is still modeled via brittle continuum damage mechanics, the respective modeling approach is referred to as ‘localized brittle damage’.

With the outlined approach, the localized brittle damage model can be built on top of the existing distributed brittle damage model. This is advantageous because the distributed brittle damage model has been shown to give good predictions in various case studies and it is therefore desired not to lose these predictive capabilities.

The concept of brittle damage proposed in Sect. 3.1 provides a direct link between scalar damage variables and the effective stiffness of the damaged ply material. This link based on an ‘abused’ micromechanical method is used also within the localized brittle damage model. However, in order to capture progressive fiber failure besides the matrix dominated phenomena, an additional population of fictitious inhomogeneities is introduced which is referred to as population 1. The inhomogeneities are thereby modeled independently from the loading conditions as spheroidal, oblate voids with the same aspect ratio as for matrix dominated damage, i.e. $e^{(f)} = e^{(m)}$, but with the axis of rotation aligned with the fiber direction.

Here it has to be repeated, that this method – although it was motivated by observations concerning matrix dominated phenomena – does not aim at capturing any

micromechanical details but uses the micromechanical method to represent the multi-axial effect of damage on the material behavior. Furthermore, it is rather intuitive to embed an increasing number of fictitious voids in order to model the effect of progressive fiber failure under tension. Under fiber compression, however, very complex phenomena such as fiber kinking and the formation of kink bands are observed in experimental testing. To model these phenomena via a fictitious porosity is definitely just a somewhat arbitrary modeling technique. Alternatively to the outlined approach based on the micromechanics method, damage variables could be introduced which are used to scale certain entries in the compliance matrix. This is done by many other authors.

With a relation available that links a certain amount of damage to the effective stiffness of the ply material, it remains to define damage evolution equations which are able to capture strain softening behavior for all populations of inhomogeneities. These evolution equations are introduced such that they become active only after conditions have been met which define softening onset. These onset-conditions are defined as follows.

Onset of softening material behavior due to progressive fiber failure is expected when a fiber exertion of

$$f_E^{(f)} = f_{E,c}^{(f)} \equiv 1 \quad (3.20)$$

is reached. Here the additional subscript ‘c’ indicates the critical state at softening onset. For matrix dominated phenomena it is assumed that softening behavior initiates as soon as a critical amount of matrix damage has accumulated. With the evolution equation, Eqn. (3.4) given in Sect. 3.1, the amount of damage is directly related to the factor of matrix exertion at least for simple load cases. Accordingly, onset of softening due to matrix dominated phenomena is expected when

$$f_E^{(m)} = f_{E,c}^{(m)} \equiv \sqrt{\frac{\xi_c^{(m)}}{k_d^{(m)}} + 1} \quad (3.21)$$

is reached. Here the parameter $\xi_c^{(m)}$ stands for the critical amount of damage and $k_d^{(m)}$ is the already discussed evolution parameter.

In order to define the damage evolution in the softening regime, the multi-axial stress and strain states are reduced to scalar ones by introducing equivalent stresses

and strains. This way, the influence of individual stress and strain components can be accounted for, whereas the evolution equation can be formulated in terms of a simple scalar relation. However, four different damage modes, namely fiber tension (ft), fiber compression (fc), matrix transverse tension (mt), and matrix transverse compression (mc) are distinguished. Softening behavior due to in-plane shear loading is not accounted for by an extra damage mode but is incorporated within the matrix modes (mc) and (mt). The equivalent stresses and strains for the different damage modes are given in Table 3.1 where the Macaulay operator $\langle \cdot \rangle$ defined as $\langle x \rangle = \frac{x+|x|}{2}$ is used. The outlined approach including the definitions of the equivalent quantities has some similarities to the model readily implemented in *Abaqus* and discussed by Lapczyk and Hurtado (2007).

To define the scalar relation that describes damage evolution in the softening regime, exponential softening is assumed and the relation

$$\hat{\sigma} = \hat{\sigma}_c \exp \left[-k_l (\hat{\varepsilon} - \hat{\varepsilon}_c) \right] \quad (3.22)$$

is required to hold for the equivalent stresses and strains. Here $\hat{\sigma}_c$ and $\hat{\varepsilon}_c$ refer to the equivalent stresses and equivalent strains, respectively, which are predicted at softening onset. The modeled exponential softening is depicted schematically in the left part of Fig.3.7. Note that in Eqn.(3.22) the superscripts are omitted which would explicitly denote the failure mode. Such superscripts are omitted also in the following.

Table 3.1: Definition of equivalent stresses, $\hat{\sigma}$, and equivalent strains, $\hat{\varepsilon}$, incorporated in the localized brittle damage model; failure due to shear dominated loading is accounted for by the interaction parameters $\alpha^{(mt)}$ and $\alpha^{(mc)}$.

mode	equivalent strain, $\hat{\varepsilon}$	equivalent stress, $\hat{\sigma}$
ft ($\sigma_{11} \geq 0$)	$\langle \varepsilon_{11}^{(el)} \rangle$	$\langle \sigma_{11} \rangle$
fc ($\sigma_{11} < 0$)	$\langle -\varepsilon_{11}^{(el)} \rangle$	$\langle -\sigma_{11} \rangle$
mt ($\sigma_{22} \geq 0$)	$\sqrt{\langle \varepsilon_{22}^{(el)} \rangle^2 + (\gamma_{12}^{(el)})^2}$	$(\langle \sigma_{22} \rangle \langle \varepsilon_{22}^{(el)} \rangle + \alpha^{(mt)} \sigma_{12} \gamma_{12}^{(el)}) / \hat{\varepsilon}^{(mt)}$
mc ($\sigma_{22} < 0$)	$\sqrt{\langle -\varepsilon_{22}^{(el)} \rangle^2 + (\gamma_{12}^{(el)})^2}$	$(\langle -\sigma_{22} \rangle \langle -\varepsilon_{22}^{(el)} \rangle + \alpha^{(mc)} \sigma_{12} \gamma_{12}^{(el)}) / \hat{\varepsilon}^{(mc)}$

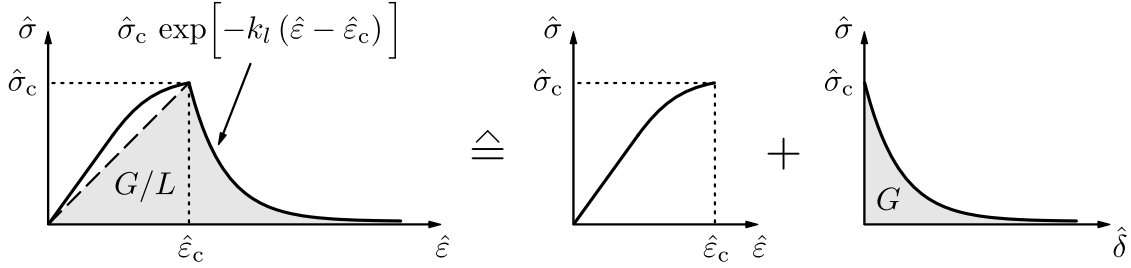


Figure 3.7: Exponential softening; relation between the equivalent stress and the equivalent strain.

With Eqn. (3.22) localized failure is modeled based on continuum damage mechanics, i.e. in terms of a stress–strain ($\hat{\sigma}$ – $\hat{\epsilon}$) relation. In order to relate this abstract formulation to quantities that can be measured by experimental testing, the requirement

$$\frac{1}{2} \hat{\sigma}_c \hat{\epsilon}_c + \int_{\hat{\epsilon}_c}^{\infty} \hat{\sigma} d\hat{\epsilon} = \frac{G}{L} \quad (3.23)$$

is introduced. Here the parameter G given in J/m^2 is associated to the energy dissipated per unit sectional area failing at the considered mode. An interpretation of the last equation is depicted in Fig. 3.7 and discussed in the following. Localized failure is usually described in terms of a stress–separation ($\hat{\sigma}$ – $\hat{\delta}$) relation, cf. Fig. 3.7 (right). This is disadvantageous in context the context of continuum damage mechanics; accordingly, the stress–separation formulation is ‘smeared out’ by means of an characteristic length L and combined with the foregoing stress–strain relation.

The parameter G has to be estimated from experimental results; how the parameter should be estimated together with the interaction parameters $\alpha^{(\text{mt})}$ and $\alpha^{(\text{mc})}$ is addressed in Sect. 3.5; the variable L represents a characteristic length which is discussed later on in this section.

With the requirement defined by Eqn. (3.23), the damage evolution variable, k_l , can be computed. When Eqn. (3.22) is plugged into Eqn. (3.23), the integral can be solved and the expression

$$k_l = \frac{2 L \hat{\sigma}_c}{2 G - L \hat{\sigma}_c \hat{\epsilon}_c} \quad (3.24)$$

is obtained. Again, the last equation has to be evaluated for all four modes.

With Eqns. (3.22) and (3.24) the softening behavior is defined in terms of equivalent stresses and strains. For implementation, however, a relation is desired that links equivalent strains – which drive damage accumulation in the softening regime – to the amount of damage. In the derivation of such a relation the effect of damage has to be incorporated as modeled by the micromechanical approach given in Sect. 3.1. However, in order to keep the derivation simple, it is assumed that the compliance matrix, $\underline{\underline{\mathbf{C}}} = [\underline{\underline{\mathbf{E}}}]^{-1}$ defined by Eqn. (3.9), can be written as

$$\underline{\underline{\mathbf{C}}} = \underline{\underline{\mathbf{C}}}^{(0)} + \underline{\underline{\mathbf{D}}} \underline{\underline{\mathbf{C}}}^{(0)} = \underline{\underline{\mathbf{C}}}^{(0)} + \frac{\xi}{1 - \xi} \underline{\underline{\mathbf{N}}}^{(0)}, \quad (3.25)$$

where ξ represents an generalized amount of damage and $\underline{\underline{\mathbf{N}}}^{(0)}$ is an auxiliary matrix. The elastic strains then read

$$\underline{\underline{\boldsymbol{\varepsilon}}}^{(\text{el})} = \underline{\underline{\mathbf{C}}}^{(0)} \underline{\underline{\boldsymbol{\sigma}}} + \frac{\xi}{1 - \xi} \underline{\underline{\mathbf{N}}}^{(0)} \underline{\underline{\boldsymbol{\sigma}}}. \quad (3.26)$$

With Eqn. (3.22) and with the assumption that

$$\underline{\underline{\boldsymbol{\sigma}}} = \frac{\hat{\sigma}}{\hat{\sigma}_c} \underline{\underline{\boldsymbol{\sigma}}}_c \quad (3.27)$$

holds in the regime after softening onset, an equation of the form

$$\xi = \frac{c \exp [k_l \hat{\varepsilon}_c] - \hat{\varepsilon} \exp [k_l \hat{\varepsilon}]}{(c - n) \exp [k_l \hat{\varepsilon}_c] - \hat{\varepsilon} \exp [k_l \hat{\varepsilon}]} \quad \text{for} \quad \hat{\varepsilon} > \hat{\varepsilon}_c \quad (3.28)$$

can be obtained from Eqn. (3.26). Note that due to the assumptions made during the derivation of the last equation, in general the requirements such as given in Eqn. (3.23) will be fulfilled in an approximate manner only. However, it can be shown that Eqn. (3.28) represents an exact solution for simple load cases. The scalars c and n introduced in Eqn. (3.28) depend on the stress states at softening onset, $\underline{\underline{\boldsymbol{\sigma}}}_c$, the virgin ply properties, and the Eshelby tensors. Note that all the incorporated variables depend on the load history prior to softening onset only.

As before, Eqn. (3.28) has to be specialized with respect to the actual failure mode. In case of mode (ft) or (fc), the generalized amount of damage ξ represents $\xi^{(\text{f})} = \xi_1$. In case of mode (mt) or (mc), ξ represents $\xi^{(\text{m})}$. With the volume fractions computed from Eqn. (3.28) the same procedure as discussed in Sect. 3.1 subsequent to Eqn. (3.4) has to be carried out in order to compute the individual volume fractions ξ_p of the populations $p = 1, 2, 3, 4$. These volume fractions ξ_p are then used to estimate the actual stiffness of the smeared out ply material.

Inobjectivity. It is rather popular to circumvent the usage of sophisticated methods from fracture mechanics by introducing strain softening in the material model. Nevertheless, straightforward strain softening has some severe drawbacks. The most pronounced one is the inobjectivity introduced by strain softening continua, which makes the simulation results dependent on the finite element discretization. This, of course, is unacceptable.

In order to avoid this undesired behavior, localization limiters or the approach of mesh adjusted softening have been proposed in the literature. In the present work the latter approach is used. Following the lecture notes by Jirásek (2005), mesh adjusted softening was first introduced by Pietruszczak and Mróz (1981) within softening plasticity but it is more often referenced to the crack models by Bažant and Oh (1983). Mesh adjusted softening is based on the introduction of a characteristic length L in the stress strain relation and is described in more detail in the following.

If strain softening without special treatment is used, it is natural in a FEM simulation that deformation concentrates in a band which is as narrow as possible. The total width of the band is basically determined by the FEM element size, FEM element type, FEM element integration scheme, alignment of the FEM element edges with respect to the localization band, and the shape of the FEM elements. The basic idea of mesh adjusted softening is to make the total amount of energy dissipated by the localization band independent of its actual width. Accordingly, in each Gauss point that is part of the localization band, the modeled stress–strain relation is enriched by an characteristic length, cf. Eqn. (3.23). This length can be interpreted as an effective width of the numerical localization band and ideally accounts for all the dependencies listed above.

The estimation of the characteristic length is far from being trivial due to its various dependencies. Numerous approaches were proposed in the literature, here, the following approach is applied. For shell elements with linear displacement interpolation functions, the square root of the element’s (membrane) area is used as the characteristic length. For shell elements with quadratic interpolation functions, the square root of the element’s area divided by the number of integration points is used. This very simplistic approach seems to be sufficient since the model part that incorporates strain softening possesses strong approximate character anyway. Note that

with this approach the mesh dependency is in general not fully avoided but it is strongly reduced. The mesh dependency is addressed in the examples of Sect. 4.4.

Note that due to the characteristic length, L , the modeled stress–strain relation in the softening regime is dependent on the local element size. Hence, the size of the elements, in which softening takes place, cannot be chosen totally arbitrary anymore as a too coarse mesh results in an effective stress-strain curve with a positive initial slope.

Viscous regularization. Pronounced nonlinear material behavior – and especially strain softening – leads to convergence problems in implicit FEM programs such as *Abaqus/Standard*. The convergence behavior can be improved by using viscous regularization.

Within the present constitutive model viscous regularization is incorporated adopted from proposals by Lapczyk and Hurtado (2007), which in turn is a generalization of the work of Duvaut and Lions (1979). Viscous regularization is defined by the rate equation

$$\dot{\xi}_p^{(v)} = \frac{1}{\eta_p} (\xi_p^{(nv)} - \xi_p^{(v)}) , \quad (3.29)$$

where $\xi_p^{(nv)}$ and $\xi_p^{(v)}$ are the volume fractions of population p in the non-viscous and the viscous system, respectively. The parameter η_p represents the viscosity coefficient associated to population p .

In equation Eqn. (3.29) special superscripts have been used to point out the difference between the state variables of the viscous and the non-viscous system, respectively. The non-viscous damage variables refer thereby to the outcome of the procedure described Sect. 3.1, where no special superscripts have been used. The viscous damage variables are the ones which are finally used to compute the actual stiffness of the ply material. For sake of simplicity the superscripts (nv) and (v) are omitted in the remaining sections.

The advantage of viscous regularization is that for sufficiently small time increments the entries of the material Jacobian matrix remain positive also in the softening regime. At the same time, the results are not compromised as long as the viscosity parameters are chosen small compared to the characteristic simulation time. Nevertheless, when the simulation results are interpreted one should keep in mind that vis-

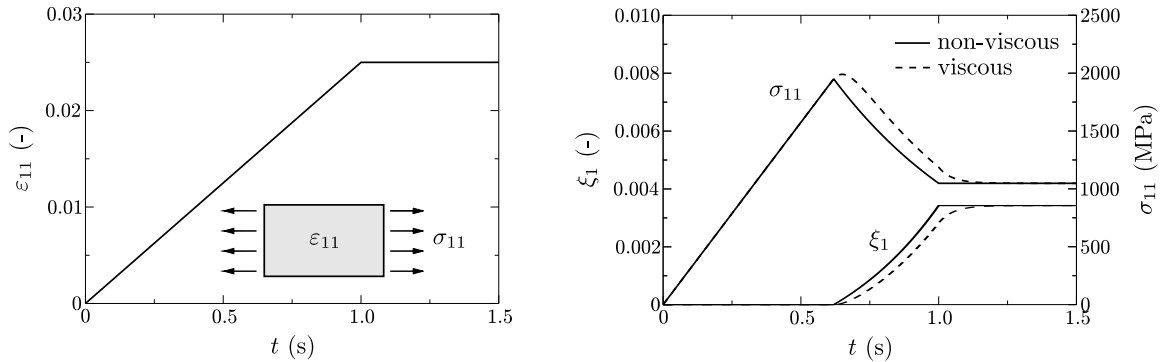


Figure 3.8: Effect of viscous regularization on the material response by example of uniaxial tension.

cus regularization increases the amount of dissipated energy. Furthermore, viscous regularization increases the peak stresses, slows down the rate of damage accumulation and retards localization. In general, with viscous regularization the material behavior becomes dependent on the deformation rates.

The effect of viscous regularization is demonstrated schematically by studying the modeled material response to uniaxial tension. The load is introduced in deformation controlled manner such that it results in a strain history as depicted in Fig. 3.8 (left). In the right diagram of Fig. 3.8, the accumulated damage as well as the stress response is plotted versus the simulation time for the non-viscous and the viscous system. The response of the viscous system is notably smoother; finally, however, the same stress and strain state is reached.

3.4 Capabilities of the constitutive model

The phenomenological constitutive model is developed to predict non-linear intra-ply behavior under consideration of stiffness degradation and plastic strain accumulation. The proposed constitutive model offers some outstanding features when it is used for simulating the response of a laminate. On the one hand, the laminate stiffness affected by the anisotropic stiffness degradation of the individual plies is modeled. On the other hand, residual deformations after unloading are predicted. Furthermore, also the load carrying capacity of components can be estimated since also strain softening behavior is incorporated.

Nevertheless, effects disregarded during the formulation of the constitutive model naturally result in some limitations. The limitations of the current constitutive model are discussed in Sect. 3.4.1.

For example within the test cases of the first and the third WWFE, the response of a uniformly loaded laminate has to be predicted without any geometrical specifications of the structure. Generally speaking, in such simulations meso-scale material models which account for strain softening cannot be used since strain localization is a feature of the structure rather than of the laminate. Accordingly, in Sect. 3.4.2 it is addressed how the present constitutive model can be applied without using the feature of localized failure.

3.4.1 Limitations concerning the model

In the present work perfect interfaces between the plies are assumed. In order to account for delamination, which is defined as failure of the ply interface, a combination of the constitutive model with an interface formulation is desirable. Whether or not such a straightforward combination is possible within the limits of applicability of both approaches has to be answered in future work. Furthermore, the present constitutive model should not be used if out of plane stresses are expected to have a pronounced influence on the laminate's nonlinear behavior.

The model is based on small strain theory, an assumption that may be violated locally in some cases due to finite deformations. Finite deformations can lead to a change of the fiber orientation, which in turn can change the laminate stiffness prevailing in

the main loading direction. Such fiber rotation is not accounted for. This might be a reason for the overestimated non-linearity observed in some test cases (cf. test case 1 in Sect. 4.2). Furthermore, rate dependent material behavior, ply thickness effects, the influence of the stacking sequence, and in-situ effects are not explicitly captured by the current model.

3.4.2 Limitations concerning the simulation

When the response of uniformly loaded laminates is simulated, the usage of the strain softening model has to be avoided. To this end, such simulations are conducted by means of single shell elements and the simulations are stopped as soon as certain conditions are met. The conditions and interpretations of respective simulation stops are discussed next.

Fiber failure in multi-directional and UD laminates. When a fiber exertion of $f_E^{(f)} = 1$ is reached in any material point of a laminate, the simulations will be stopped. This is associated with ultimate failure of the uniformly loaded laminate.

Allowable amount of matrix damage in multi-directional laminates. When a total amount of matrix damage of $\xi^{(m)} = \sum_{i=2}^4 \xi_i = \xi_a^{(m)}$ is reached, the simulations will be stopped. The fulfillment of this condition is associated with severe disintegration of the laminate. However, in experiments an increase of the applied stress beyond such damage states may be possible in some cases. Note that the choice of the allowable amount of matrix damage, $\xi_a^{(m)}$, is challenging since it may depend on various parameters such as e.g. the ply thickness.

Allowable amount of matrix damage in UD laminates. In case of UD laminates simulations are stopped when a material exertion of $f_E^{(m)} = 1$ is reached. This means that no distributed damage is expected to accumulate in case of UD laminates before ultimate failure occurs. All observed non-linearity in the response of UD laminates is attributed to plastic strain accumulation.

3.5 Calibration

The constitutive model is based on mechanisms which mimic the behavior of the ply material qualitatively. For quantitative predictions calibration of the model parameters with respect to the considered ply material system is inevitable. For a detailed calibration of all the incorporated parameters, some elaborate experimental data would be desired. However, for basic calibration which is sufficient for practical usage, several model parameters can be estimated from plausible assumptions or from experience, but at least the following material data is needed. (i) The ply stiffness of the undamaged material, (ii) the nominal ply strength values, (iii) the parameters describing Puck's failure surface, (iv) the coefficients of thermal expansion and the laminate's stress free temperature, (v) a shear stress–shear strain curve due to simple (in-plane) shear loading, (vi) a stress–strain curve due to uniaxial transverse (in-plane) compression, and (vii) the four parameters concerning energy dissipation if also strain softening is simulated. Note that the material properties (i) to (iv) are data as being required for classical first ply failure analyses in which usually linear elastic material behavior is assumed. A possible procedure for basic calibration is described in the next paragraphs.

Distributed brittle damage. The two most important parameters of the distributed damage model, i.e. the aspect ratio $e^{(m)}$ and the damage evolution parameter $k_d^{(m)}$, cannot be calibrated independently of each other. To identify them from experiments, data extracted from unloading curves such as the degradation of the engineering moduli as function of the measured strain could be used, i.e. relations reading $E_2 = E_2(\varepsilon_{22})$ and $G_{12} = G_{12}(\gamma_{12})$. As this data may be unavailable, the following approach is selected. On the one hand, a small aspect ratio is proposed in order to model crack like voids; for polymers reinforced by unidirectional fibers an aspect ratio of $e^{(m)} \approx 0.01$ is recommended. On the other hand, the evolution parameter $k_d^{(m)}$ is calibrated so that the transmitted ply stresses do not markedly increase after damage onset in case of uniaxial transverse tension.

For multi-directional laminates a good estimation of the maximum allowable amount of matrix damage, $\xi_a^{(m)}$, is known from experience, i.e. from the comparison of predictions with experimental results for various case studies, to be $\xi_a^{(m)} \approx 0.1$. If

uni-directional laminates are analyzed, the maximum allowable amount of matrix damage is set to $\xi_a^{(m)} = 0.0$ as already discussed in Sect. 3.4. As soon as the softening model is used, the maximum allowable amount of matrix damage becomes obsolete, but then the critical damage amount that triggers softening onset, $\xi_c^{(m)}$, needs to be defined. It turns out that this value has to be smaller, i.e. $\xi_c^{(m)} < \xi_a^{(m)}$. The difference between $\xi_a^{(m)}$ and $\xi_c^{(m)}$ can be interpreted as follows. The parameter $\xi_a^{(m)}$, which by the way is of low physical relevance, is used to roughly estimate the load carrying capacity of a uniformly loaded laminates determined by matrix dominated phenomena. Its choice is challenging as it depends on various other parameters. The parameter $\xi_c^{(m)}$ triggers softening onset due to localized matrix dominated phenomena; the effect of such softening behavior on the response of the component is then a result of the FEM simulation. However, onset of softening due to matrix dominated phenomena usually does lead to failure of the component. Accordingly, it is natural to allow more matrix damage in simulations where no strain softening is considered compared to simulations where localized failure due matrix dominated phenomena is incorporated. To complete the material data for the damage model, $\mu_d = 10$ is recommended which is of the same magnitude as proposed by Schuecker and Pettermann (2008b).

Multi-surface plasticity. In the present model the non-linearity observed before reaching the nominal ply strength is attributed to plastic strain accumulation. Accordingly, the hardening behavior can be calibrated from the measured stress–strain data, whereby all parameters of Eqn. (3.14) need to be determined for both plasticity mechanisms. The parameters k and n can be determined by a least squares regression. With a reasonably chosen auxiliary parameter κ^* and due to the requirement of a smooth hardening behavior, the yield stress of the virgin material $\tilde{\sigma}^{(0)}$ can be computed.

The two stress interaction parameters, λ_I and λ_{II} , for the model of plastic strain accumulation can be calibrated from biaxial test data. If such data is not available, the usage of $\lambda_I = 1.50$ and $\lambda_{II} = 0.25$, is recommended. In order to avoid the onset of mechanism p_I under uniaxial transverse loading and to avoid the onset of mechanism p_{II} under pure shear loading, the interactions parameters $\mu_I^{(t)}$, $\mu_I^{(c)}$, and μ_{II} have to satisfy

$$\mu_I^{(t)} \leq \frac{\tilde{\sigma}_I^{(0)}}{a Y^{(t)}} \quad , \quad \mu_I^{(c)} \leq \frac{\tilde{\sigma}_I^{(0)}}{a Y^{(c)}} \quad , \quad \mu_{II} \leq \frac{\tilde{\sigma}_{II}^{(0)}}{a S} \quad , \quad (3.30)$$

where the auxiliary parameter a reads

$$a = \sqrt{\frac{\xi_a^{(m)}}{k_d^{(m)}} + 1} . \quad (3.31)$$

By Schuecker and Pettermann (2008b) the approximation $\mu_I^{(t)} = p^{(t)}$ has been suggested, where $p^{(t)}$ stands for one of Puck's slope parameter. This approximation satisfies the first requirement in Eqn. (3.30) for common material systems, but it tends to overestimate the influence of transverse tensile stresses and smaller values are recommended. For the interaction parameters $\mu_I^{(c)}$ and μ_{II} , the values close to the maximum allowable ones from Eqn. (3.30) are recommended.

Localized brittle damage. If strain softening is simulated, the parameters $G^{(ft)}$, $G^{(fc)}$, $G^{(mt)}$, and $G^{(mc)}$ as well as the interaction parameters $\alpha^{(mt)}$ and $\alpha^{(mc)}$ need to be estimated from experimental test results. For this purpose it is assumed that the specific fracture energies $G^{(ft)}$, $G^{(fc)}$, $G^{(mt)}$, and $G^{(mc)}$ can be directly obtained from experiments concerning uniaxial tension in fiber direction, uniaxial compression in fiber direction, uniaxial tension in transverse direction, uniaxial compression in transverse direction. Furthermore, it is assumed that the specific fracture energy $G^{(ps)}$ corresponding to localized matrix dominated failure under pure (in-plane) shear loading can be measured. Note that these measured specific fracture energies are incorporated into the formulation for localized failure based on elasto-damage, cf. Eqn. (3.23). This is done even though the measured specific fracture energies may be affected by distributed damage or other inelastic processes.

Especially under compressive loading conditions such tests are difficult to perform and, accordingly, the expertise of other work groups needs to be trusted. For information on possible experimental setups cf. e.g. the papers by Pinho et al. (2006, 2009); for analytical considerations see e.g. the paper by Bažant et al. (1999) or by Maimí et al. (2007b). Typical values of the specific fracture energies can be found in Table C.7.

Due to the definitions from Sect. 3.3, the interaction parameters $\alpha^{(mt)}$ and $\alpha^{(mc)}$ define the fracture energy at pure shear loading compared to the fracture energy at uniaxial transverse loading. Hence, they should not be estimated independently but a transition condition can be used. This transition condition states that the response to

pure shear loading in combination with infinitesimal transverse tension is the same as the response as pure shear loading in combination with infinitesimal transverse compression. The interaction parameters finally read

$$\alpha^{(mt)} = \frac{G^{(mt)}}{G^{(ps)}} \quad \text{and} \quad \alpha^{(mc)} = \frac{G^{(mc)}}{G^{(ps)}} . \quad (3.32)$$

If strain softening is simulated, some modifications of the above calibration scheme are recommended. Most important, the stiffness recovery parameter must be set to $\mu_d = 0$, cf. Eqn. (3.8), in order to allow for a completely damaged material. Motivated by numerical aspects, it is furthermore recommended to use $s = 1$ and $m = 1$ for the weakening parameters due to stresses in fiber direction. Finally it is repeated that the requirements given in Eqn. (3.30) have to be fulfilled also when peak stresses are increased due to viscous regularization.

3.6 Implementation

The development of the constitutive model aims at the analysis of laminated, thin-walled structures. Since FEM is a state-of-the-art tool for structural analysis, the constitutive law is implemented as User defined MATERIAL routine (UMAT) for the commercial FEM package Abaqus/Standard 6.9.

The material model and also its implementation is based on small strain assumption. Furthermore, the material model has been derived for plane stress states, an assumption that gave reason to implement the model for stress states as being handled by shell elements with layered section definitions.

Altogether, the present approach can be sketched as done in Fig. 3.9. In an FEM analysis, the UMAT representing the constitutive model of the ‘smeared out’ ply material is called in each Gauss point throughout the ply thickness. The shell elements with layered section definitions, in turn, are used to build up the FEM model of considered structure.

Within classical nonlinear FEM, Newton-Raphson algorithms are employed to solve for the global equilibrium. Such algorithms lead to incremental, iterative solution schemes. This means that the load is incrementally applied to the structure, whereas global equilibrium that corresponds to the currently applied load and the other boundary conditions has to be found iteratively. In each iteration of each load increment of the solution scheme and at each Gauss point for which the user material is employed, the user subroutine UMAT is called.

At each call the UMAT is provided with quantities that characterize the state reached at the end of the previous load increment²⁾, i.e. basically the stress state, ${}^0\boldsymbol{\sigma}$, the strain state, ${}^0\boldsymbol{\xi}$, and the material state monitored throughout the FEM analysis by solution dependent state variables, ${}^0\boldsymbol{g}$. The main task of the UMAT is to compute the stress state, $\boldsymbol{\sigma}$, which is induced by an prescribed strain increment³⁾, $\Delta\boldsymbol{\xi}$, and the resulting strain state,

$$\boldsymbol{\xi} = {}^0\boldsymbol{\xi} + \Delta\boldsymbol{\xi} . \quad (3.33)$$

²⁾Quantities that belong to the ‘beginning of the load increment’, i.e. the end of the previous load increment, are denoted by an leftsided superscript ${}^0(\cdot)$, whereas quantities with no specific index refer to the ‘end of the increment’.

³⁾within the framework of ‘displacement controlled’ FEM

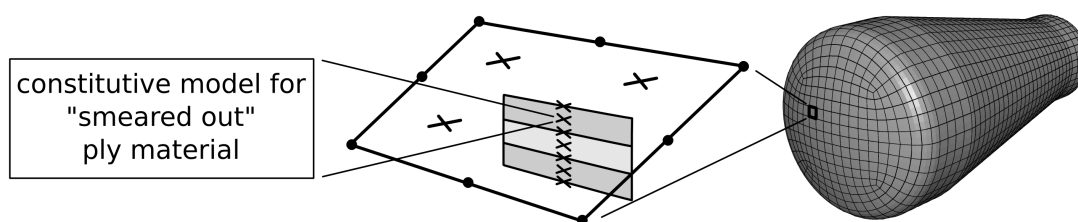


Figure 3.9: Sketch of the present approach. The constitutive model for the smeared out ply material (left) is applied in each Gauss point throughout the ply thickness; the shell elements with layered section definitions (middle) are used to build up the FEM model (right).

To this end, in general, rate equations that define the material behavior have to be integrated and a respective change in the material state has to be monitored by an update of the solution dependent state variables. Furthermore, the material Jacobian has to be computed as it is needed by the global Newton-Raphson algorithm.

The strain contributions which are passed into the `UMAT` are the mechanical strains, i.e. total strains minus thermal strains. This fact makes it possible to simulate temperature loads or to account for residual ply stresses from curing independent of the implemented material model. This holds true as long as the coefficients of thermal expansion are independent of the actual material state and as long as some stress free temperature of the laminate is available.

In the next paragraphs the numerical procedure for integration of the present constitutive law is sketched. Afterwards the implementation of viscous regularization is discussed and the material Jacobian is derived. Finally some comments are given concerning the user interface with `Abaqus/Standard`.

3.6.1 Numerical solution procedure

In the present constitutive law two types of effects, which are attributed to different phenomena, are modeled. Both effects contribute to the non-linearity in the response of the ply material. Brittle damage is reflected by a change in the elasticity matrix $\underline{\underline{E}}$ of the smeared out ply material, whereas the incorporated plasticity model leads to plastic strain increments, $\Delta \underline{\underline{\varepsilon}}^{(pl)}$. Accordingly, after appropriate integration of the constitutive equations,

$$\underline{\underline{\sigma}} = \underline{\underline{E}} \underline{\underline{\varepsilon}}^{(el)} = \underline{\underline{E}} (\underline{\underline{\varepsilon}} - \underline{\underline{\varepsilon}}^{(pl)}) \quad (3.34)$$

$$= \underline{\underline{E}} (({}^0 \underline{\underline{\varepsilon}} + \Delta \underline{\underline{\varepsilon}}) - ({}^0 \underline{\underline{\varepsilon}}^{(pl)} + \Delta \underline{\underline{\varepsilon}}^{(pl)})) \quad (3.35)$$

is required to hold at the end of an increment. In the present model plasticity is defined by the rate equations given in Sect.3.2. Distributed brittle damage is modeled with respect to the stress state, cf. Sect.3.1, whereas the localized brittle damage is modeled with respect to the elastic strain state, cf. Sect.3.3. Furthermore, all model parts are driven by nominal stresses and strains, which is in contrast to the commonly used effective stress and strain concept known in context of damage mechanics⁴), see e.g. Lemaitre (1992).

In order to compute the unknown quantities $\underline{\underline{\sigma}}$, $\underline{\underline{E}}$, and $\Delta \underline{\underline{\varepsilon}}^{(pl)}$, an implicit numerical procedure tailored to the particular needs of the actual formulation of the model is developed. The numerical procedure is built up of several hierarchically arranged levels of operations. In order to present the hierarchical structure of the procedure in a clear manner, the main task of each level is given next; afterwards each level is treated separately. Note that the numerical procedure is designed to handle different variants of the material model, i.e. elastic, elasto-plastic, and elasto-damage, and the elasto-plasto-damage model. As the first three are subsets of the latter one, the procedure is described in a simplified manner only for the elasto-plasto-damage model.

On top of the hierarchy, preparatory and closing computations enclose a subincrementation, in which the prescribed strain increment is divided into equal subincrements (Level 0). Within the subincrementation an iterative scheme is called which is ba-

⁴) In the frame work of damage mechanics, effective stresses term stresses transmitted by the undamaged material which remains between the effective damage zones; in the framework of micromechanics, effective stresses term nominal stresses.

sically used to solve for the unknown damage state (Level 1). Again, within this iterative scheme a subprocedure is called for stress and plastic strain computation (Level 2).

Level 0. At beginning of a UMAT call, the state reached at the previous increment is read and the incorporated variables are initialized. Subsequently, the unknown stress and material state of the non-viscous system, i.e. without viscous regularization, induced by the prescribed strain increment $\Delta\boldsymbol{\varepsilon}$ needs to be computed. As the strain increment $\Delta\boldsymbol{\varepsilon}$ may be large especially in the first equilibrium iterations, this computation is done within a subincrementation that splits the original strain increment $\Delta\boldsymbol{\varepsilon}$ into equal subincrements $\Delta\Delta\boldsymbol{\varepsilon}$. The subincrements are then applied consecutively (index k); the operations conducted within each cycle of the subincrementation are described in the next paragraph (Level 1). At the end of the subincrementation the state of the non-viscous system is known. If viscous regularization is used, $\boldsymbol{\sigma}$, $\underline{\underline{\boldsymbol{E}}}$, and $\boldsymbol{\varepsilon}^{(pl)}$ of the viscous system (clarifying superscripts omitted) is computed next. Afterwards the material Jacobian matrix, $\underline{\underline{\boldsymbol{T}}}$, the engineering elastic constants of the damaged material, the exertion factors, the energy densities, and other usefull quantities are computed. Also the softening parameters are updated as they depend on the loading history. Finally, the status variables are updated. Therewith, a single call of the UMAT is closed.

Level 1. Here the unknown damage state of the non-viscous system induced by an subincrement ${}^k\Delta\Delta\boldsymbol{\varepsilon}$ is computed. To this end, trial stress and plastic strains are computed using ${}^{k-1}\underline{\underline{\boldsymbol{E}}}$ from the last subincrement first (cf. Level 2). Afterwards it is determined whether or not the damage state is expected to change. If so, the governing system of equations is solved iteratively (index n), which can be, therefore, conceptionally written as

$$F[{}^{n-1}\xi^{(m)}] - {}^n\xi^{(m)} = 0 . \quad (3.36)$$

Here the total amount of matrix damage, $\xi^{(m)}$, is used as the control variable⁵⁾. In each cycle of the iteration, the elasticity matrix of the damaged material ${}^n\underline{\underline{\boldsymbol{E}}} = \underline{\underline{\boldsymbol{E}}}[\xi^{(m)}]$ is computed. Aftwards, stresses and plastic strains are computed (cf. again Level 2)

⁵⁾Note that the left superscript corresponding to the subincrement k for Level 0 is omitted in Eqn. (3.36) for sake of simplicity.

and the damage state of iteration n is predicted including the total amount of matrix damage ${}^n\zeta^{(m)}$. However, in order to improve the convergence behavior of the iteration, information from previous iteration cycles is also used for the estimation of the new damage state ${}^n\zeta^{(m)}$. Finally, the iteration is stated to be converged when the change in the amount of matrix damage as well as the change in the stress components are sufficiently small, i.e. $|{}^n\zeta^{(m)} - {}^{n-1}\zeta^{(m)}| < \delta_\xi$ and $\|{}^n\boldsymbol{\sigma} - {}^{n-1}\boldsymbol{\sigma}\| < \delta_\sigma$ hold where δ_ξ and δ_σ are suitable convergence thresholds.

Level 2. Here stresses, ${}^n\boldsymbol{\sigma}$, and the plastic strains, ${}^n\boldsymbol{\varepsilon}^{(pl)}$, are computed from a given stiffness matrix, ${}^n\boldsymbol{E}$, and a given strain subincrement, ${}^k\Delta\Delta\boldsymbol{\varepsilon}$. For this purpose a predictor/corrector algorithm is applied, cf. e.g. Simo and Hughes (1998). Thereby, classical trial stresses are computed first, i.e. ${}^n\boldsymbol{\varepsilon}^{(pl)} = {}^{n-1}\boldsymbol{\varepsilon}^{(pl)}$ is used for stress computation. The trial stresses are also used to define the set of active plasticity mechanisms. Afterwards, a Newton iteration is initiated to solve for the consistency parameters that guarantee $f_a = 0$ at the end of the increment, where f denote the yield functions and a corresponds to the active mechanisms. Within each loop of this Newton iteration, corrections $\Delta\dot{\Lambda}_a$ of consistency parameters are computed. After convergence of the Newton iteration, it has to be verified whether or not the found solution is admissible. This is done by checking if the rates of the internal hardening variables are all non-negative and by checking if $f_i \leq 0$ still holds true for the inactive mechanisms i . If the solution is found to be non-admissible, the assumption regarding the active mechanisms was wrong and the Newton iteration has to be initiated again with a modified set of active mechanisms.

3.6.2 Viscous regularization

The rate equation (3.29) which defines viscous regularization has to be integrated numerically. To this end, the rate $\dot{\xi}_p^{(v)}$ is replaced by the finite difference approximation (backward in time)

$$\dot{\xi}_p^{(v)} \approx \frac{\xi_p^{(v)} - {}^0\xi_p^{(v)}}{\Delta t} \quad (3.37)$$

with respect to a simulation (pseudo) time t . With Eqn. (3.29) this results in the simple integration scheme

$$\xi_p^{(v)} = \frac{1}{1 + \Delta t/\eta_p} \left(\frac{\Delta t}{\eta_p} \xi_p^{(nv)} + {}^0\xi_p^{(v)} \right). \quad (3.38)$$

In the last two equations the superscripts (nv) and (v) have been used to point out the difference between the state variables of the viscous and the non-viscous system, respectively. For sake of simplicity the superscripts (nv) and (v) are again omitted in the remaining sections.

3.6.3 Tangent operator

In the course of the global equilibrium iterations of the FEM program, the tangential stiffness matrix of the structure is assembled and used to estimate corrections for the displacement field. In that stiffness matrix, the material behavior is incorporated via the material Jacobian matrix, $\underline{\underline{\mathbf{T}}}$, which is termed tangent operator in the following. The consistent computation of $\underline{\underline{\mathbf{T}}}$, which has to be done by the material routine, is one prerequisite for quadratic convergence of the global Newton-Raphson iteration. In this context consistent means that in the derivation of the tangent operator the features of the actually implemented algorithm are accounted for.

The consistent tangent operator, $\underline{\underline{\mathbf{T}}} = [T_{ij}]$, of the constitutive model defines the change in the i -th stress component at the end of the strain increment caused by an infinitesimal perturbation of the j -th component of the strain increment vector (see Abaqus/Standard User's Manual, 2009). With $\underline{\underline{\boldsymbol{\sigma}}} = [\sigma_i]$ being the stress components computed by the implemented algorithm, i.e.

$$\sigma_i = {}^0\sigma_i + \Delta\sigma_i, \quad (3.39)$$

and $\underline{\underline{\boldsymbol{\varepsilon}}} = [\varepsilon_j]$ being the input to the algorithm, i.e.

$$\varepsilon_j = {}^0\varepsilon_j + \Delta\varepsilon_j, \quad (3.40)$$

the consistent tangent operator can be written as

$$T_{ij} = \frac{d(^0\sigma_i + \Delta\sigma_i)}{d(^0\varepsilon_j + \Delta\varepsilon_j)} = \frac{d(\Delta\sigma_i)}{d(\Delta\varepsilon_j)}. \quad (3.41)$$

This definition already reveals the procedure for the derivation of the tangent operator. First the relation between stresses and strains is expressed on basis of the implemented incremental equations. Afterwards total derivatives are computed and rearranged in order to end up with a single expression for the desired tangent operator. The derivation of the tangent operator for the present constitutive law is outlined next.

The mechanical strain, which is composed of an elastic and a plastic contribution, reads

$$\boldsymbol{\varepsilon} = \boldsymbol{\varepsilon}^{(\text{el})} + \boldsymbol{\varepsilon}^{(\text{pl})} = \underset{\approx}{\mathbf{C}} \boldsymbol{\sigma} + \boldsymbol{\varepsilon}^{(\text{pl})}. \quad (3.42)$$

Its total derivative reads

$$d\boldsymbol{\varepsilon} = \underset{\approx}{\mathbf{C}} d\boldsymbol{\sigma} + d\underset{\approx}{\mathbf{C}} \boldsymbol{\sigma} + d\boldsymbol{\varepsilon}^{(\text{pl})}, \quad (3.43)$$

where $\underset{\approx}{\mathbf{C}}$ is the compliance matrix of the possibly damaged ply material. To obtain the tangent operator from Eqn.(3.43), the second and the third term need to be expressed in terms of $d\boldsymbol{\sigma}$ and $d\boldsymbol{\varepsilon}$, respectively.

If all the incorporated inhomogeneities are voids, the compliance matrix, $\underset{\approx}{\mathbf{C}} = [\underset{\approx}{\mathbf{E}}]^{-1}$, defined by Eqn. (3.9) can be written as

$$\underset{\approx}{\mathbf{C}} = \underset{\approx}{\mathbf{C}}^{(0)} + \sum_p \underset{\approx}{\mathbf{D}}^{(p)} \underset{\approx}{\mathbf{C}}^{(0)} = \underset{\approx}{\mathbf{C}}^{(0)} + \sum_p h^{(p)} \underset{\approx}{\mathbf{Z}}^{(p)} \quad (3.44)$$

with a scalar function $h^{(p)} = h^{(p)}[\xi_1, \xi_2, \xi_3, \xi_4]$ and an auxiliary matrix $\underset{\approx}{\mathbf{Z}}^{(p)}$. Since $d\underset{\approx}{\mathbf{Z}}^{(p)} = 0$ for void populations, it holds

$$d\underset{\approx}{\mathbf{C}} = \sum_p dh^{(p)} \underset{\approx}{\mathbf{Z}}^{(p)} \quad \text{and} \quad d\underset{\approx}{\mathbf{C}} \boldsymbol{\sigma} = \sum_p dh^{(p)} \underset{\approx}{\mathbf{Z}}^{(p)} \boldsymbol{\sigma}, \quad (3.45)$$

respectively. The scalar function $h^{(p)}$ depends on the volume fractions ξ_p , which, in turn, are related to the stress and elastic strain increments by means of the damage evolution equations. Accordingly, the total derivative of $h^{(p)}$ can be written as

$$dh^{(p)} = \mathbf{a}^{(p)} \cdot d\boldsymbol{\sigma} + \mathbf{b}^{(p)} \cdot d\boldsymbol{\varepsilon}^{(\text{el})}, \quad (3.46)$$

where $\mathbf{a}^{(p)}$ and $\mathbf{b}^{(p)}$ account for contributions from the distributed and the localized damage model, respectively. Note that in the last equation also viscous regularization and the derivatives of the factors of exertion are incorporated. Due to the last two equations, the second term of Eqn. (3.43) reads

$$d\underset{\approx}{\mathbf{C}} \boldsymbol{\sigma} = \sum_p (\underset{\approx}{\mathbf{Z}}^{(p)} \boldsymbol{\sigma}) \mathbf{a}^{(p)} \cdot d\boldsymbol{\sigma} + \sum_p (\underset{\approx}{\mathbf{Z}}^{(p)} \boldsymbol{\sigma}) \mathbf{b}^{(p)} \cdot d\boldsymbol{\varepsilon}^{(\text{el})} = \underset{\approx}{\mathbf{A}} d\boldsymbol{\sigma} + \underset{\approx}{\mathbf{B}} d\boldsymbol{\varepsilon}^{(\text{el})}, \quad (3.47)$$

where the matrices $\underset{\approx}{\mathbf{A}}$ and $\underset{\approx}{\mathbf{B}}$ have been introduced for sake of brevity. If also populations with non-zero stiffness are modeled, $\underset{\approx}{\mathbf{A}}$ and $\underset{\approx}{\mathbf{B}}$ are computed in an approximate manner only as $d\underset{\approx}{\mathbf{Z}}^{(p)} \approx 0$ and $d\beta \approx 0$, cf. Eqn. (3.5), is assumed. Consequently, the tangent operator is not fully consistent in such situations.

With respect to the third term of Eqn. (3.43), the plasticity model has to be considered. To this end the plastic strain is written as

$$\boldsymbol{\varepsilon}^{(\text{pl})} = {}^0\boldsymbol{\varepsilon}^{(\text{pl})} + \Delta\boldsymbol{\varepsilon}_{\text{I}}^{(\text{pl})} + \Delta\boldsymbol{\varepsilon}_{\text{II}}^{(\text{pl})} = {}^0\boldsymbol{\varepsilon}^{(\text{pl})} + \Delta\Lambda_{\text{I}} \frac{\partial g_{\text{I}}}{\partial \boldsymbol{\sigma}} + \Delta\Lambda_{\text{II}} \frac{\partial g_{\text{II}}}{\partial \boldsymbol{\sigma}}, \quad (3.48)$$

where $\partial g_{\text{I}}/\partial \boldsymbol{\sigma}$ and $\partial g_{\text{II}}/\partial \boldsymbol{\sigma}$ have been introduced in order to define the direction of the plastic flow with respect to the actual stress state. Due to the specific non-associated flow rules the total derivative reads

$$d\boldsymbol{\varepsilon}^{(\text{pl})} = d\Delta\Lambda_{\text{I}} \frac{\partial g_{\text{I}}}{\partial \boldsymbol{\sigma}} + d\Delta\Lambda_{\text{II}} \frac{\partial g_{\text{II}}}{\partial \boldsymbol{\sigma}}. \quad (3.49)$$

If both plasticity mechanisms are active, the unknowns $d\Delta\Lambda_{\text{I}}$ and $d\Delta\Lambda_{\text{II}}$ can be eliminated by means of the requirements $df_{\text{I}} = 0$ and $df_{\text{II}} = 0$. Finally it holds

$$d\boldsymbol{\varepsilon}^{(\text{pl})} = \left(\frac{\partial g_{\text{I}}}{\partial \boldsymbol{\sigma}} \left[\frac{\partial \sigma_{\text{I}}}{\partial \boldsymbol{\sigma}} \right]^{\text{T}} \left[\frac{\partial \tilde{\sigma}_{\text{I}}}{\partial \kappa_{\text{I}}} \right]^{-1} + \frac{\partial g_{\text{II}}}{\partial \boldsymbol{\sigma}} \left[\frac{\partial \sigma_{\text{II}}}{\partial \boldsymbol{\sigma}} \right]^{\text{T}} \left[\frac{\partial \tilde{\sigma}_{\text{II}}}{\partial \kappa_{\text{II}}} \right]^{-1} \right) d\boldsymbol{\sigma} = \underset{\approx}{\mathbf{P}} d\boldsymbol{\sigma}, \quad (3.50)$$

where the matrix $\underset{\approx}{\mathbf{P}}$ has been introduced. Therewith, the derivative of the elastic strain can be written as

$$d\boldsymbol{\varepsilon}^{(\text{el})} = d\boldsymbol{\varepsilon} - d\boldsymbol{\varepsilon}^{(\text{pl})} = d\boldsymbol{\varepsilon} - \underset{\approx}{\mathbf{P}} d\boldsymbol{\sigma}. \quad (3.51)$$

Plugging the intermediate results obtained before into Eqn. (3.43) yields

$$d\boldsymbol{\varepsilon} = \underset{\approx}{\mathbf{A}} d\boldsymbol{\sigma} + \underset{\approx}{\mathbf{B}} d\boldsymbol{\varepsilon} - \underset{\approx}{\mathbf{B}} \underset{\approx}{\mathbf{P}} d\boldsymbol{\sigma} + \underset{\approx}{\mathbf{C}} d\boldsymbol{\sigma} + \underset{\approx}{\mathbf{P}} d\boldsymbol{\sigma}. \quad (3.52)$$

This equation can be rearranged and it follows the tangent operator as

$$\underset{\approx}{\mathbf{T}} = \left[\underset{\approx}{\mathbf{A}} - \underset{\approx}{\mathbf{B}} \underset{\approx}{\mathbf{P}} + \underset{\approx}{\mathbf{C}} + \underset{\approx}{\mathbf{P}} \right]^{-1} \left(\underset{\approx}{\mathbf{I}} - \underset{\approx}{\mathbf{B}} \right), \quad (3.53)$$

which is computed at the end of the numerical solution procedure described before. When neither damage nor plastic strains accumulate, e.g. in case of unloading, the last equation degenerates and the secant stiffness matrix is obtained as expected,

$$\underline{\underline{\mathbf{T}}} = \left[\underline{\underline{\mathbf{C}}} \right]^{-1} \underline{\underline{\mathbf{I}}} = \underline{\underline{\mathbf{E}}} . \quad (3.54)$$

Chapter 4

Applications

The capabilities of the proposed constitutive model are assessed by comparing its predictions to experimental measurements. For this purpose laminates subjected to homogeneous loading conditions, coupon tests, and other components are considered. Emphasis is placed on studying various loading conditions which lead to pronounced damage accumulation and/or drive the evolution of plastic strains. Furthermore, characteristic examples are discussed in which the expected effects can be studied in a decoupled manner.

To judge the quality of the constitutive model is a difficult task. Even if the nonlinear response is predicted correctly for a given load case, it is not evident whether or not the constitutive law captures the underlying phenomena. Furthermore, one is not able to consider all possible loading scenarios as an infinite number of them exist. However, a large amount of experimental data treated with statistical methods would be preferable for a well-founded assessment of the predictions. As such an amount of data is not available, at least various loading scenarios are considered in the present work in order to increase the confidence in the model predictions.

For calibration of the constitutive model the procedure outlined in Sect. 3.5 is followed. However, peculiarities are discussed in the respective sections. The used material data is summarized in the tables of Appendix C.

For all predictions presented in the following sections, the FEM software **Abaqus/Standard** is utilized in combination with the implemented constitutive model. To

simulate the response of laminates subjected to homogeneous loading conditions, a single shell element with a layered section definition is used.

When multi-directional laminates are considered, residual stresses from curing are taken into account at ply level. To this end, the laminate is cooled down from the stress free temperature, T_{sf} , which is given as part of the material data, to a temperature of 20°C. Note that such residual stresses can affect the load level of damage onset considerably.

The documentation of the predictions is mainly done in terms of stress–strain curves and, additionally, in terms of curves presenting the evolution of brittle damage and of plastic strains.

In the following Sect. 4.1 the predictions are compared to experimental results published by Vogler and Kyriakides (1999). The experiments concern an UD laminate under biaxial loading. Under such loading conditions the constitutive model predicts plastic strain accumulation only, what makes the experimental results best suited to study the capabilities of the plasticity model.

In Sect. 4.2 some laminate tests from the first WWFE (Hinton et al., 2004) are considered. One of these examples is a $[0^\circ/90^\circ]_S$ laminate subjected to uniaxial tension, where only brittle damage is predicted by the constitutive model. This decoupling makes the test case very useful for assessing the predictions of the model for distributed damage.

In Sect. 4.3 the predictions are documented as obtained for the test cases of part A of the third WWFE (Kaddour et al., 2010), even though experimental results are not yet available. The test cases are discussed here since the author, C. Schuecker, and H.E. Pettermann submitted a contributing paper (Flatscher et al., 2009b), which is currently in review. The test cases of the third WWFE consider uni-directional laminates under biaxial loads, laminates under various loading conditions, and open hole tests. Note that some test cases obviously aim at effects which are not incorporated in the actual version of the model.

In Sect. 4.4 the dependency of the simulation results on the FEM discretization is addressed. Mesh dependency occurs only in the softening regime, but it is alleviated in the present model by means of mesh adjusted softening. Mesh dependency is studied

by simulating rupture of a composite strip which possesses a small imperfection in order to trigger the localization, whereby various FEM discretizations are considered.

In Sect. 4.5 the coupon tests conducted at the *PCCL* are analyzed. These tests are primarily designed to assess the predictions of the plasticity model. Accordingly, coupons with various layups were subjected to compression so that the resulting ply stress states are composed of transverse compressive and in-plane shear stresses.

In Sect. 4.6 a very challenging open hole tension test is simulated. Even though the geometry of the considered specimen is simple, the study can definitely be seen as a structural FEM analysis. The results are discussed and compared qualitatively to publications of various authors.

4.1 Biaxial loading of a UD laminate

In this section predictions published by Flatscher et al. (2009a) are compared to measurements by Vogler and Kyriakides (1999), who studied the nonlinear response of UD laminates made of AS4/PEEK. The experiments were conducted with small coupons tested in a biaxial testing facility, whereby the loading was introduced in a stress controlled manner. The performed experiments can be classified as follows. First, the response to simple shear and uniaxial transverse compression was measured. Second, proportional ply loading was applied in biaxial testing, where the stress ratios, $-\sigma_{22}/\sigma_{12}$, were kept constant during loading. The investigated stress ratios range from $-\sigma_{22}/\sigma_{12} = 0.98$ to 7.17, where for the shear stress $\sigma_{12} > 0$ holds. Third, non-proportional loading was performed by applying preloads leading to constant ply shear stresses, $\check{\sigma}_{12}$, and constant transverse compressive stresses, $\check{\sigma}_{22}$, respectively. Subsequently, the other stress component of interest was ramped up until ultimate failure. The magnitude of the preloads ranges from $\check{\sigma}_{12}/S = 0.54$ to 0.84 in case of preceding shear loads and from $-\check{\sigma}_{22}/Y^{(c)} = 0.21$ to 0.68 in case of preceding compressive loads, respectively. Here, S denotes the shear strength and $Y^{(c)}$ denotes the transverse compression strength of the UD laminate. The applied proportional and non-proportional ply loading paths are sketched in Fig. 4.1.

Calibration. In order to employ the constitutive model, it is calibrated with respect to the considered material system. To this end, the procedure outline in Sect. 3.5 is followed. However, some peculiarities are discussed in the following.

In the present model all non-linearity in the response of homogeneous loaded UD laminates is related to plastic strain accumulation. Hence, no damage accumulation is modeled but immediate failure of the UD laminate is expected when a material exertion of $f_E^{(m)} = 1$ or $f_E^{(f)} = 1$ is reached. Consequently, the damage parameters are not required for this case study. The number of relevant model parameters is further reduced since no transverse tension is considered. The required material parameters are calibrated or estimated as follows.

The thermo-elastic properties and values defining the nominal strength of AS4/PEEK can be found in Tabs. C.1, C.2, and C.3. Respective data is taken from the paper by Hsu et al. (1999) except for the in-plane shear modulus of the ply, G_{12} ,

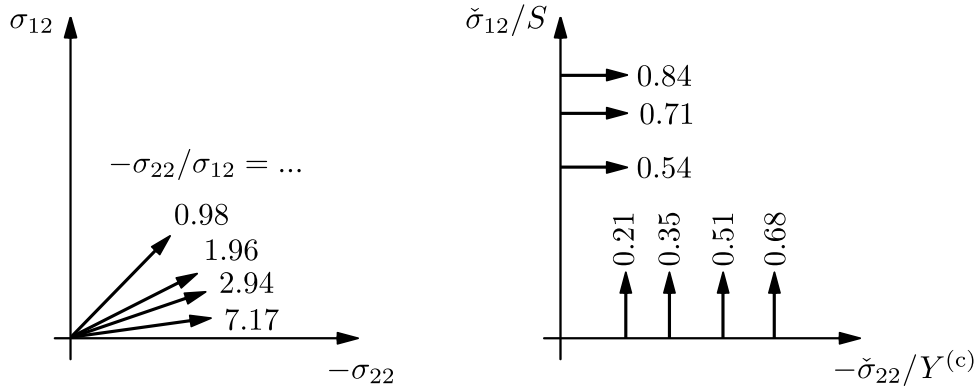


Figure 4.1: Sketch of the proportional (left) and non-proportional (right) ply loading paths considered by Vogler and Kyriakides (1999).

which is slightly reduced in accordance with the initial shear stiffness measured by Vogler and Kyriakides (1999). The strength data is extracted from the measured response to simple shear and uniaxial transverse compression. The Puck parameter $p^{(c)}$ can be estimated from the measured ultimate failure stress states since it just describes the inclination of the failure surface given the σ_{22} – σ_{12} stress space at $\sigma_{22} = 0$ towards the compressive side. This approach results in a choice of $p^{(c)} = 0.15$, cf. Table C.4, which is lower than the recommendations given by Puck et al. (2002). Note that in the predictions discussed below this parameter affects only the predicted ultimate failure stresses but has no influence in the predicted strain paths. In the present analyses the parameter $p^{(c)}$ is the only Puck parameter needed.

The hardening behavior is calibrated based on the stress–strain curves from simple shear and uniaxial transverse compression. The respective parameters are summarized in Table C.5.

Finally, the four interaction parameters λ_{I} , λ_{II} , $\mu_{\text{I}}^{(c)}$, and μ_{II} are calibrated. These parameters can be found in Table C.6. The parameter λ_{I} defines the stress ratio, at which transverse compressive stresses start to amplify the evolution of plastic shear strains. Therefore, the parameter can be estimated by inspection of the shear stress–shear strain curves measured under proportional loads. At a stress ratio of $-\sigma_{22}/\sigma_{12} = 0.98$ no increased, actually, a reduced plastic shear strain evolution is observed. At a stress ratio of $-\sigma_{22}/\sigma_{12} = 1.96$, already a slightly increased evolution is measured. Accordingly, an interaction parameter of $\lambda_{\text{I}} = 1.5$ is chosen. The

parameter λ_{II} is defined in a similar manner by reference to the influence of shear stresses on the evolution plastic normal strains. Inspection of the transverse stress–transverse strain curves measured under proportional loading, leads to a choice of $\lambda_{II} = 0.25$.

Obviously, a part of experimental data is used to estimate the parameters λ_I and λ_{II} although the same data is used to assess to quality of the model predictions. However, this seems to be of minor relevance since the considered predictions are insensitive to a change of parameters λ_I and λ_{II} . If no biaxial data is available to calibrate the model, it is recommended to use similar values as estimated above.

The remaining parameters $\mu_I^{(c)}$ and μ_{II} are computed from the inequalities given by the Eqn. (3.30), whereby values close to the maximum allowable ones are used for the present predictions.

Results. In Fig. 4.2 the response measured by Vogler and Kyriakides (1999) (dashed lines) as well as the model predictions (solid lines) for proportional loading are given in terms of engineering shear strain, γ_{12} , versus transverse strain, $-\varepsilon_{22}$. Note that the curves which were used for calibration are not shown. It can be seen that the highly nonlinear (bi-axial) strain response is predicted correctly by the model. The predicted ultimate strains slightly exceed the measured values; this becomes obvious when the end points of the predicted curves are compared to the measured ones. The mismatch originates from overestimated ultimate stresses. However, for a stress ratio of $-\sigma_{22}/\sigma_{12} = 0.98$, the predicted ultimate strains are underestimated. The latter discrepancy is caused by the exhausted hardening observed in the experimental testing, i.e. the shear strains increase while the stresses remain almost constant before ultimate failure. The strain states which are predicted when the measured ultimate stresses are applied are marked by circles. These circles correlate very well with the measured ultimate strain states, i.e. the end points of the measured strain paths.

In Fig. 4.3 the shear stress, σ_{12} , is plotted versus the engineering shear strain, γ_{12} . There also the stress–strain state experimentally measured at ultimate failure due to simple shear loading is indicated by ‘+’; the respective curve is not shown. For a stress ratio of $-\sigma_{22}/\sigma_{12} = 0.98$, the measured shear stress–shear strain curve is slightly shifted to higher stresses compared to the curve measured under simple shear. This effect is not incorporated in the current model; nevertheless, an increased strength –

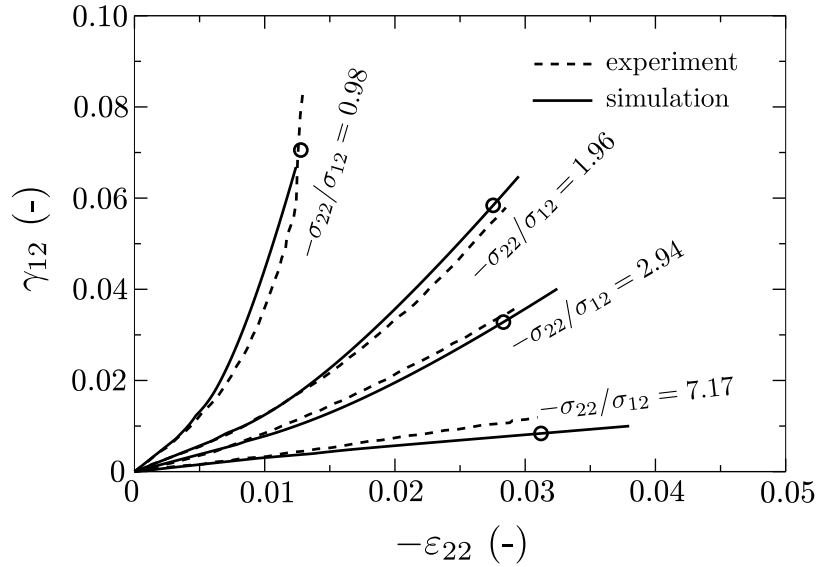


Figure 4.2: Nonlinear strain response of a UD laminate made up of AS4/PEEK to biaxial proportional loading with various stress ratios, $-\sigma_{22}/\sigma_{12}$; engineering shear strain, γ_{12} , versus transverse strain, $-\epsilon_{22}$; experimental data measured by Vogler and Kyriakides (1999) (dashed lines) and model predictions (solid lines); circles indicate strain states which are predicted when the measured ultimate stresses are applied.

which results in a higher ultimate shear strain – is predicted correctly. By a further increase of the stress ratio, the shear stress–shear strain curves shift to lower stresses. At the same time, ultimate stresses as well as ultimate strains decrease, cf. the end points of the curves. This behavior is predicted correctly by the model as well.

In Fig. 4.4 the transverse stress, $-\sigma_{22}$, is plotted versus the transverse strain, $-\epsilon_{22}$. The stress–strain curve measured under uniaxial transverse compression is not shown, but the stress–strain state experimentally measured at ultimate failure is indicated by ‘ \times ’. It can be seen that a reduction of the stress ratio $-\sigma_{22}/\sigma_{12}$ decreases the ultimate stresses and the ultimate strains compared to the values measured under uniaxial transverse compression, cf. again the end points of the curves. This behavior is captured by the model.

The strain response to the non-proportional loading conditions is given for preceding transverse compression in Fig. 4.5. Here the predicted strain paths correlate well with the measurements. The strain states which are predicted when the measured ultimate

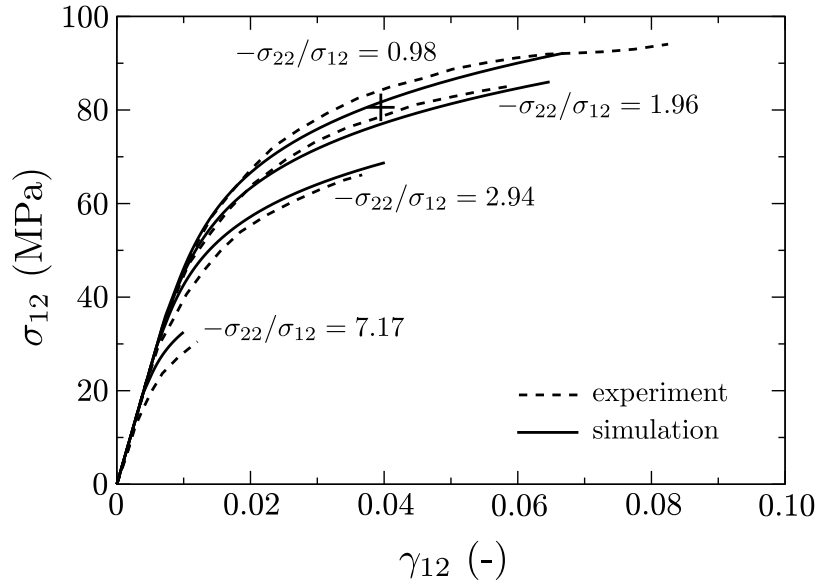


Figure 4.3: Nonlinear response of a UD laminate made up of AS4/PEEK to biaxial proportional loading with various stress ratios, $-\sigma_{22}/\sigma_{12}$; shear stress, σ_{12} , versus engineering shear strain, γ_{12} ; experimental data measured by Vogler and Kyriakides (1999) (dashed lines) and model predictions (solid lines); the state which is measured at failure due to simple shear load is indicated by ‘+’.

stresses are applied (circles) correlate well with the measured ultimate strains apart from the preload of $-\check{\sigma}_{22}/Y^{(c)} = 0.51$. The same holds true for the predicted ultimate strains. The discrepancy in the case of $-\check{\sigma}_{22}/Y^{(c)} = 0.51$ again originates from the exhausted hardening, i.e. in experimental testing the shear strains increase at almost constant stresses.

For preceding shear loads, the strain response is given in Fig. 4.6. Here the qualitative behavior is predicted correctly but the predicted paths differ somewhat from the measured ones. From stress–strain curves, which are not shown here, it can be concluded that this discrepancy originates from underestimated shear strains. The transverse strains correlate well with the measurements. The same tendency holds for the strain states which are predicted when the measured ultimate stresses are applied. Note that it is arguable whether or not the shear strains are subject to creep effects which are not incorporated in the current model.

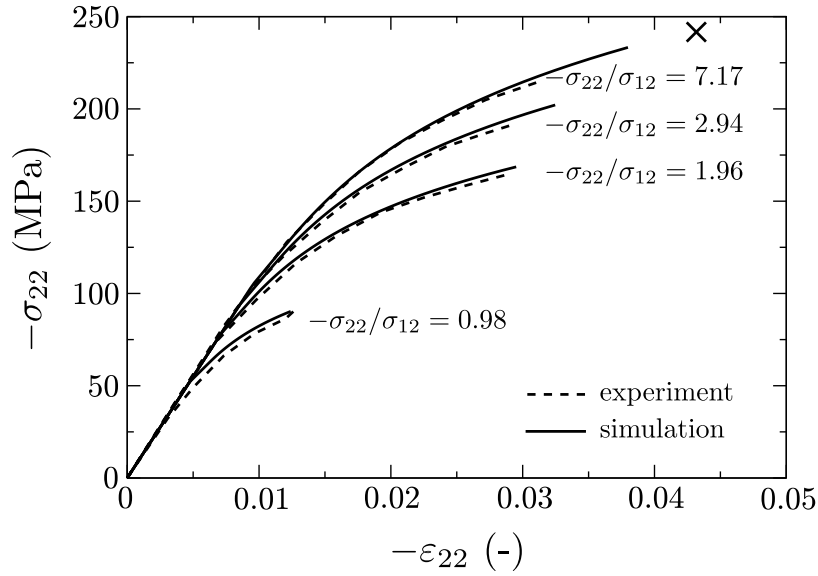


Figure 4.4: Nonlinear response of a UD laminate made up of AS4/PEEK to biaxial proportional loading with various stress ratios, $-\sigma_{22}/\sigma_{12}$; transverse compressive stress, $-\sigma_{22}$, versus transverse strain, $-\varepsilon_{22}$; experimental data measured by Vogler and Kyriakides (1999) (dashed lines) and model predictions (solid lines); the state which is measured at ultimate failure due to uniaxial transverse compression is indicated by ‘×’.

Discussion. The comparison of the model predictions to the experimental data shows good agreement. The highly nonlinear strain response of the UD laminate is predicted correctly. This holds true for the proportional as well as the non-proportional ply load cases. Furthermore, the strain states which are predicted when the measured ultimate stresses are applied correlate well with the measured ultimate strains. Note that both plasticity mechanisms are activated in all the considered load cases except for simple shear loading and uniaxial transverse compression.

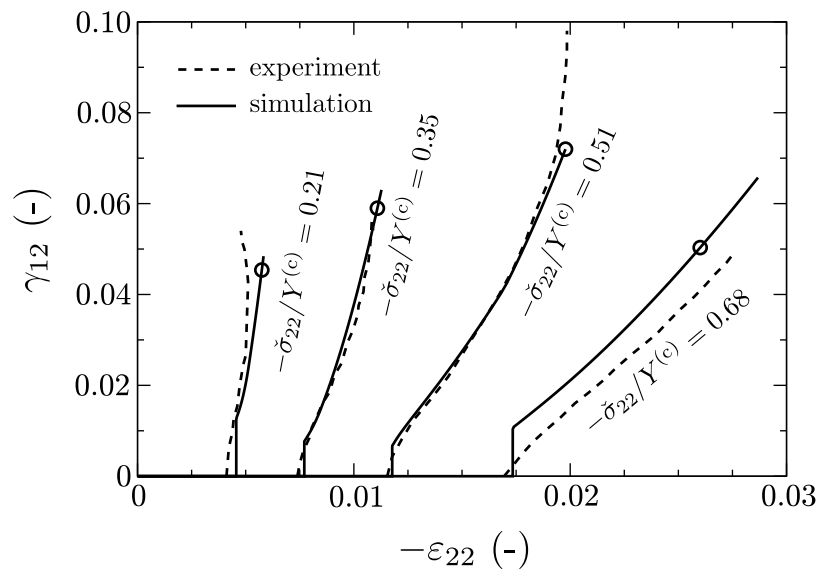


Figure 4.5: Nonlinear response of a UD laminate made up of AS4/PEEK under biaxial non-proportional loading; preceding loads are applied to impose constant transverse stresses, $-\check{\sigma}_{22}$; engineering shear strain, γ_{12} , versus transverse strain, $-\varepsilon_{22}$; experimental data measured by Vogler and Kyriakides (1999) (dashed lines) and model predictions (solid lines); circles indicate strain states which are predicted when the measured ultimate stresses are applied.

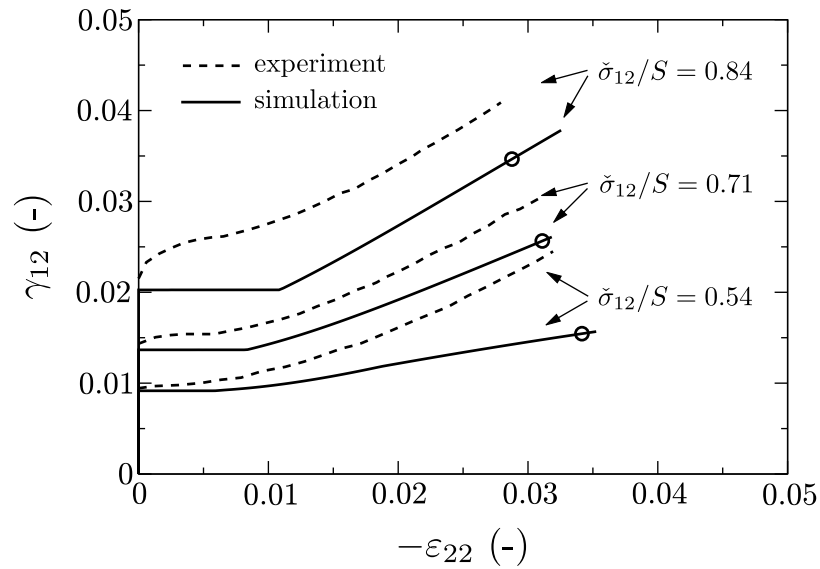


Figure 4.6: Nonlinear response of a UD laminate made up of AS4/PEEK under biaxial non-proportional loading; preceding loads are applied to impose constant shear stresses, $\check{\sigma}_{12}$; engineering shear strain, γ_{12} , versus transverse strain, $-\epsilon_{22}$; experimental data measured by Vogler and Kyriakides (1999) (dashed lines) and model predictions (solid lines); circles indicate strain states which are predicted when the measured ultimate stresses are applied.

4.2 Test cases from the first WWFE

In this section the test cases of the first world wide failure exercise (Hinton et al., 2004) focusing on nonlinear laminate behavior are studied. The test cases consider laminates with different layups made of AS4/3501-6 or glass/epoxy subjected to uniaxial or biaxial loads. Apart from a coupon test with a cross ply laminate (test case 7), the loading conditions are realized by subjecting tubular specimens to combinations of internal pressure and axial loads. In case of biaxial loading the stress ratio $\sigma_{yy} : \sigma_{xx}$, which gives the ratio of hoop to axial laminate stresses, is kept fixed. Note that the x -axis of the laminate coordinate system is parallel to the axis of the tube; the x -axis in turn is used for the definition of the fiber orientation angle. The tubular specimens possess a diameter of typically 100 mm and a wall thickness of approximately 1 mm unless otherwise noted. Some of the tubes are lined with additional layers in order to avoid premature leakage failure. For a more detailed description of the actual specimens and the experimental setups the comprehensive introductory paper by Soden et al. (2002) can be consulted. There also the experimental results are summarized with references to the sources of the experimental data.

All the test cases considered in the present work are listed in table Table 4.1. The numbering is not consistent with the WWFE but the ‘figure numbers’ given in Table 4.1 refer to the paper by Soden et al. (2002).

For each test case studied in the following, the predictions are obtained from simulations with single shell elements and layered section definitions. Residual stresses from curing are taken in account by simulating a cooling-down from the given stress free temperature, T_{sf} , to a temperature of 20°C. The predictions are documented in terms of stress–strain curves, whereby load levels that correspond to onset of the modeled mechanisms are marked by different symbols. Additionally, the conditions are given which have triggered the simulations to stop. Load levels concerning important observations from the experiments are indicated by horizontal lines.

Some of the test cases of the first WWFE have been investigated in the thesis by Schuecker (2005). However, the model has changed substantially in the last years and so it is definitely worth to redo the analysis.

Calibration. The considered test cases focus on the two material systems, namely AS4/3501-6 and glass/epoxy. The constitutive model has to be calibrated with respect to these material systems before it can be employed for quantitative predictions. Accordingly, the procedure outlined in Sect. 3.5 is followed.

From the detailed material data provided within the first WWFE (Soden et al., 1998), the ply stiffness of the undamaged material, the coefficients of thermal expansion and the stress free temperature as well as values for the nominal ply strength are used directly for model calibration. The respective parameters are listed in Tabs. C.1, C.2, and C.3, respectively. Additionally, the parameters which describe Puck's failure surface are needed. Since these data has not been provided, the slope parameters $p^{(t)}$ and $p^{(c)}$ are estimated following the guidelines given by Puck et al. (2002); the weakening parameters s and m concerning high stress in fiber direction are chosen as suggested by Schürmann (2005). The parameters describing Puck's failure surface are listed in Table C.4. From the shear stress–shear strain curves under simple (in-plane) shear loading and from the stress–strain curves under uniaxial transverse (in-plane) compression provided within the first WWFE, the parameters of the modified power laws are extracted and summarized in Table C.5. All remaining model parameters, which are estimated according to the procedure proposed in Sect. 3.5, are listed in Table C.6.

Table 4.1: Test cases of the first WWFE considered in the present work; the layup is defined with respect to the x -axis; the given stress ratio $\sigma_{yy} : \sigma_{xx}$ defines the applied loading (a positive sign indicates ‘tension’); the ‘figure’ entries refer to the paper by Soden et al. (2002) in which the experimental results are presented.

test case	system	layup	$\sigma_{yy} : \sigma_{xx}$	figure	specimen
1	glass/epoxy	$[\pm 55^\circ]_S$	1 : 0	8	tube
2	glass/epoxy	$[\pm 55^\circ]_S$	2 : 1	9	tube
3	glass/epoxy	$[\pm 45^\circ]_S$	1 : 1	13	tube
4	glass/epoxy	$[\pm 45^\circ]_S$	1 : -1	14	tube
5	AS4/3501-6	$[90^\circ/\pm 45^\circ/0^\circ]_S$	20 : 1	11	tube
6	AS4/3501-6	$[90^\circ/\pm 45^\circ/0^\circ]_S$	2 : 1	12	tube
7	glass/epoxy	$[0^\circ/90^\circ]_S$	0 : 1	16	coupon

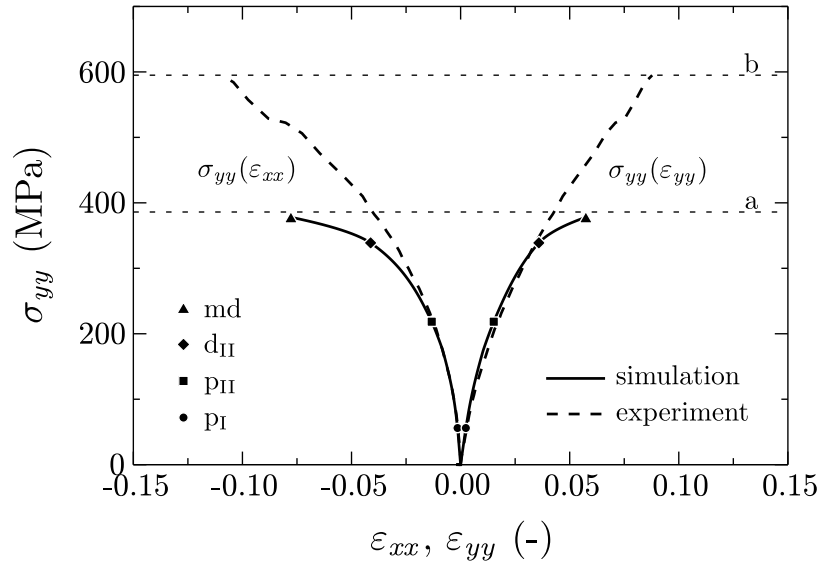


Figure 4.7: Test case 1 of the first WWFE. Response of a $[\pm 55^\circ]_S$ laminate made of glass/epoxy to uniaxial tension ($\sigma_{yy} : \sigma_{xx} = 1 : 0$); predictions and experimental results (Soden et al., 2002) are plotted in terms of laminate stress, σ_{yy} , versus laminate strains, ε_{xx} and ε_{yy} .

Test case 1 considers a $[\pm 55^\circ]_S$ laminate made of glass/epoxy subjected to a laminate stress ratio of $\sigma_{yy} : \sigma_{xx} = 1 : 0$. In order to achieve the desired stress ratio in the tube walls, internal pressure is applied but the pressure in axial direction is carried by separate pistons. Tests are performed on tubes with and without additional plastic liners. The predicted (solid line) and measured laminate response (dashed line) can be seen in Fig. 4.7, where the laminate stress, σ_{yy} , is plotted versus the laminate strains, ε_{xx} and ε_{yy} .

From the experiments it is reported that there was considerable variation (up to $\pm 20\%$) in the readings from individual strain gages applied on different positions on the same tubular specimen. In Fig. 4.7 only one selected stress–strain curve obtained with a lined tube is documented, which is reported to be on the lower strain bound of the results. Further comments from experimental testing concern ‘weeping of unlined tubes’ (horizontal line a) and ‘fracture of lined tubes’ (horizontal line b). No comments are made on observations regarding ultimate failure. In the simulations the onset of plasticity mechanism p_I (\bullet) is followed by plasticity mechanism p_{II} (\blacksquare) and damage mechanism d_{II} (\blacklozenge). Finally, ultimate failure is predicted because the

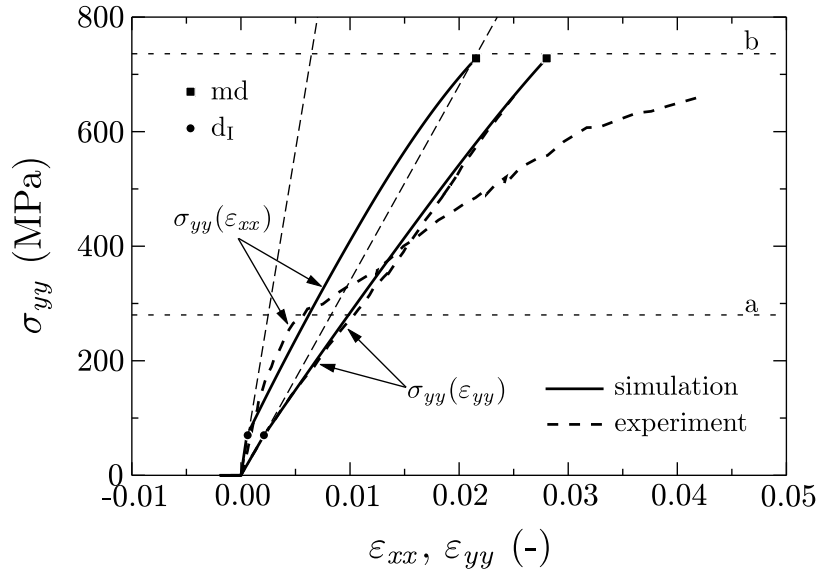


Figure 4.8: Test case 2 of the first WWFE. Response of a $[\pm 55^\circ]_S$ laminate made of glass/epoxy to biaxial loading ($\sigma_{yy} : \sigma_{xx} = 2 : 1$); predictions and experimental results (Soden et al., 2002) are plotted in terms of laminate stress, σ_{yy} , versus laminate strains, ε_{xx} and ε_{yy} .

maximum allowable damage amount (\blacktriangle) is reached. Obviously, the nonlinearity is overestimated compared to the measured curve being on the lower strain bound of the results; the reason for this is not clear by now. Interestingly, damage onset followed by ultimate failure is predicted at load levels where leakage failure of the unlined tubes makes further pressurization of the tube impossible in experimental testing.

Test case 2 considers a $[\pm 55^\circ]_S$ laminate made of glass/epoxy subjected to a laminate stress ratio of $\sigma_{yy} : \sigma_{xx} = 2 : 1$. The experimental results are obtained from tests with similar tubes as used in test case 1 but with enclosed end caps. The predicted (solid line) and the measured laminate response (dashed line) obtained with a lined specimen can be seen in Fig. 4.8.

The measured stress–strain curves end before the load of ultimate fracture is reached because of premature strain gage failure. Again, notable variation in the strain gage readings is reported, especially with respect to strain in the axial direction. It is further reported that the shape of stress–strain curves is different from results of other investigators who use different types of glass/epoxy and different specimen

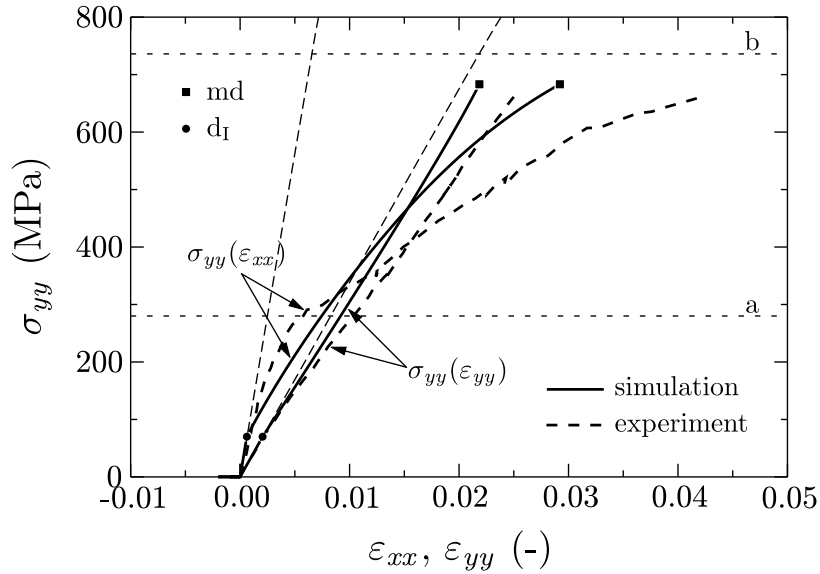


Figure 4.9: Test case 2 of the first WWFE. Response of a laminate made of glass/epoxy to biaxial loading ($\sigma_{yy} : \sigma_{xx} = 2 : 1$); predictions for a $[\pm 56^\circ]_S$ laminate are compared to experimental results (Soden et al., 2002) obtained with a $[\pm 55^\circ]_S$ laminate; the response is documented in terms of laminate stress, σ_{yy} , versus laminate strains, ε_{xx} and ε_{yy} .

geometries. For more details on the different sources of the experimental data the reader is again referred to the paper by Soden et al. (2002). Further observations from experimental testing concern ‘weeping of unlined tubes’ (a) and ‘fracture of lined tubes’ (b). In the experiments failure occurs due to extensive cracking parallel and across the fibers. In the simulation damage mechanism d_I (\bullet) becomes active already at low loads. Note that this damage onset is strongly influenced, i.e. shifted to lower stresses, by the modeled residual stresses from curing. Ultimate failure is predicted because the maximum allowable damage amount is reached (\blacksquare). However, the fiber exertion is already high ($f_E^{(f)} = 0.83$) at the respective load level. The correlation between predictions and measurement is not satisfactory. As already noted by Puck and Schürmann (2002), the discrepancy might originate from the sensitivity of the experimental setup to the fiber orientation. To demonstrate the significant impact of a slightly changed fiber orientation, in Fig. 4.9 predictions for a $[\pm 56^\circ]_S$ laminate are compared to the same experimental results. The correlation is considerably increased; the kink in the stress–strain response observed at the load level of

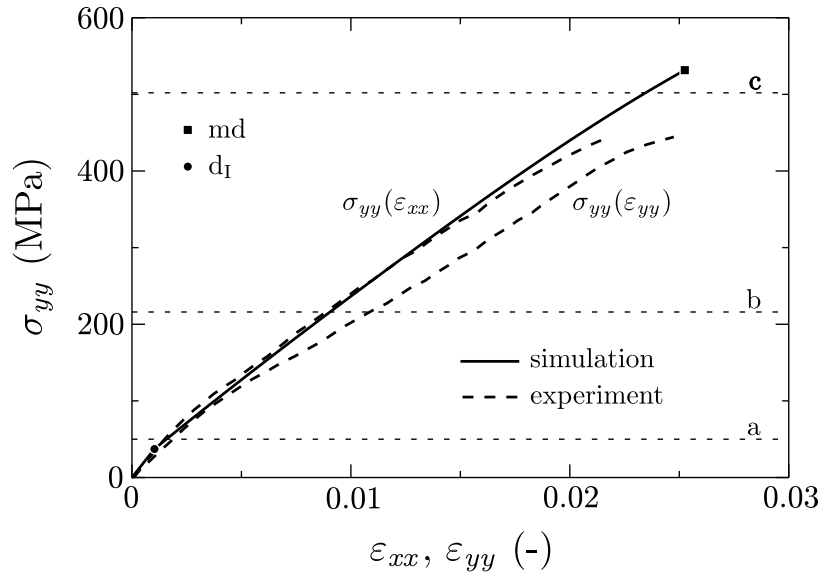


Figure 4.10: Test case 3 of the first WWFE. Response of a $[\pm 45^\circ]_S$ laminate made of glass/epoxy to biaxial tensile loading ($\sigma_{yy} : \sigma_{xx} = 1 : 1$); predictions and experimental results (Soden et al., 2002) are plotted in terms of laminate stress, σ_{yy} , versus laminate strains, ε_{xx} and ε_{yy} .

leakage failure (horizontal line a), however, is still not predicted. Note that up to this load level already nonlinear behavior is observed. This becomes most obvious when the curves are compared to the linear elastic response (thin dashed line) also plotted in Fig. 4.9.

Test case 3 considers a $[\pm 45^\circ]_S$ laminate made of glass/epoxy subjected to a laminate stress ratio of $\sigma_{yy} : \sigma_{xx} = 1 : 1$. The predicted (solid line) and the measured response obtained with a lined specimen (dashed line) can be seen in Fig. 4.10.

Again, severe variation of individual strain gage readings (up to 22%) is reported. Furthermore, as reported by Soden et al. (2002) it is not clear to the investigators why the measured axial strain differs from the measured hoop strain. Further observations from experimental testing concern the estimated ‘onset of matrix cracking’ (a), the ‘leakage of unlined tubes’ (b), and ‘fiber failure of lined tubes’ (c). In the simulations onset of damage mechanism $d_I(\bullet)$ is predicted; ultimate failure is predicted because the maximum allowable matrix damage is reached (\blacksquare). Again, the fiber exertion is

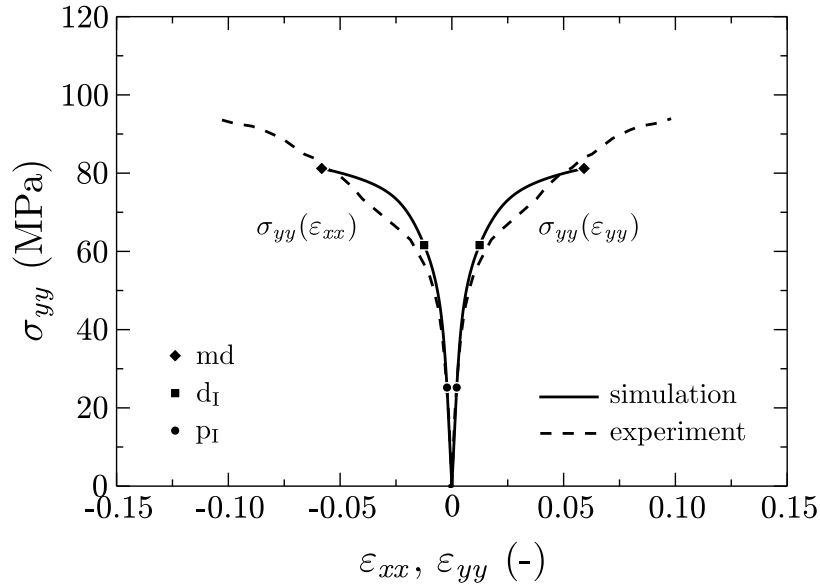


Figure 4.11: Test case 4 of the first WWFE. Response of a $[\pm 45^\circ]_S$ laminate made of glass/epoxy to biaxial loading ($\sigma_{yy} : \sigma_{xx} = 1 : -1$); predictions and experimental results (Soden et al., 2002) are plotted in terms of laminate stress, σ_{yy} , versus laminate strains, ε_{xx} and ε_{yy} .

high ($f_E^{(f)} = 0.80$) at the respective load level. The correlation with the measured response is satisfactory.

Test case 4 considers a $[\pm 45^\circ]_S$ laminate made of glass/epoxy subjected to a stress ratio of $\sigma_{yy} : \sigma_{xx} = 1 : -1$. To achieve the desired loading conditions, tubes are pressurized and axially compressed. The tubes are of the same diameter as before but they possess a wall thickness of typically 5.9 mm in order to avoid buckling.

In Fig. 4.11 the predicted response (solid line) is compared to the measured response (dashed line) obtained with a lined specimen. It is reported that the measured stresses and strains refer to the inside surface of the relatively thick-walled tube. No additional observations are reported. In the simulations onset of plasticity mechanism p_I (\bullet) is followed by damage d_I (\blacksquare). Finally the maximum allowable amount of damage (\blacklozenge) is reached. Keeping in mind the obviously quite demanding experimental setup, the correlation between measurement and prediction is not too bad. However, onset of damage might be predicted too late at too high loads.

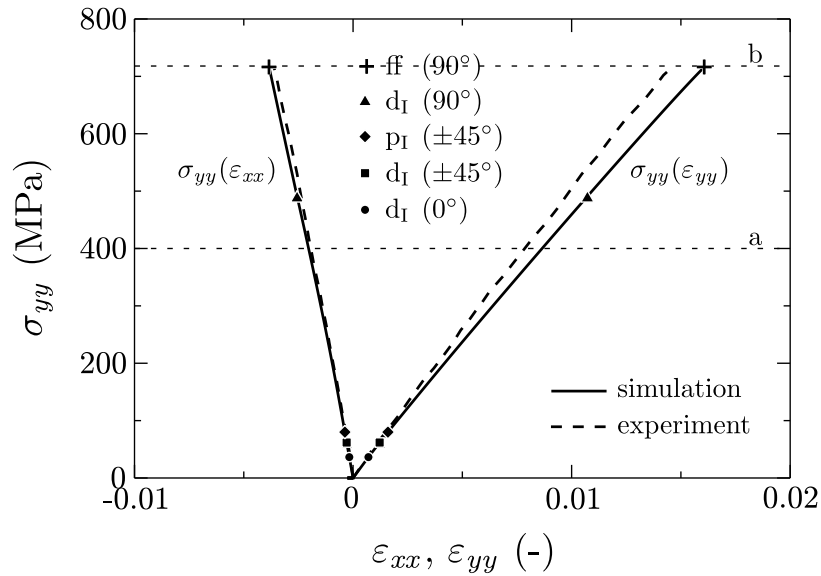


Figure 4.12: Test case 5 of the first WWFE. Response of a $[90^\circ/\pm 45^\circ/0^\circ]_S$ laminate made of AS4/3501-6 to almost uniaxial tensile loading ($\sigma_{yy} : \sigma_{xx} = 20 : 1$); predictions and experimental results (Soden et al., 2002) are plotted in terms of laminate stress, σ_{yy} , versus laminate strains, ε_{xx} and ε_{yy} .

Test case 5 considers a quasi-isotropic $[90^\circ/\pm 45^\circ/0^\circ]_S$ laminate made of AS4/3501-6. The tubes used in the experiments are subjected to internal pressure leading to an effective laminate stress ratio of $\sigma_{yy} : \sigma_{xx} = 20 : 1$.

In Fig. 4.12 the predicted (solid line) and measured laminate response (dashed line) is shown. Additional observations from experiments concern ‘possible matrix cracking’ (a) and final fiber failure (b). In the simulations a number of mechanisms become active; consecutively, onset of d_I in 0° -plies, onset of d_I in $\pm 45^\circ$ -plies, onset of p_I in $\pm 45^\circ$ -plies, and onset of d_I in 90° -plies is predicted. Finally fiber failure in 90° -plies is predicted. Even though several mechanisms are active, they do not strongly affect the overall laminate response. Finally ultimate failure due to fiber fracture (+) is predicted. Obviously, the strain in the main loading direction (ε_{yy}) is slightly overestimated; the ultimate failure stress is predicted correctly.

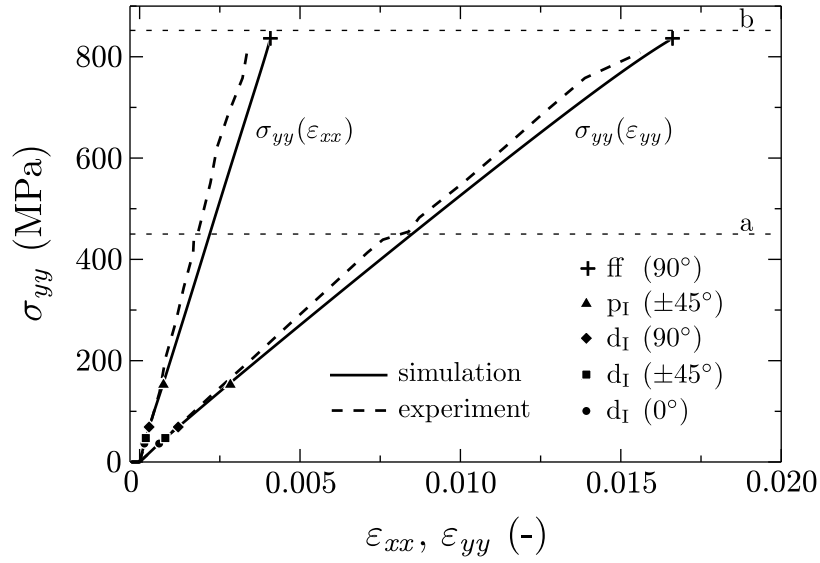


Figure 4.13: Test case 6 of the first WWFE. Response of a $[90^\circ/\pm 45^\circ/0^\circ]_S$ laminate made of AS4/3501-6 to biaxial tensile loading ($\sigma_{yy} : \sigma_{xx} = 2 : 1$); predictions and experimental results (Soden et al., 2002) are plotted in terms of laminate stress, σ_{yy} , versus laminate strains, ε_{xx} and ε_{yy} .

Test case 6 considers a quasi-isotropic $[90^\circ/\pm 45^\circ/0^\circ]_S$ laminate made of AS4/3501-6. Similar tubes as in the test case before are utilized but a stress ratio of $\sigma_{yy} : \sigma_{xx} = 2 : 1$ is applied. In Fig. 4.13 the predicted (solid line) and measured laminate response (dashed line) is shown.

Observations from experiments (Soden et al., 2002) concern ‘possible matrix cracking’ (a) and ‘final failure’ (b). In the simulations a number of mechanisms become active (see Fig. 4.13); however, the damage and the plastic strain accumulation do not affect the overall laminate response significantly. Finally ultimate failure due to fiber failure is predicted. The correlation with the experimental results is satisfactory.

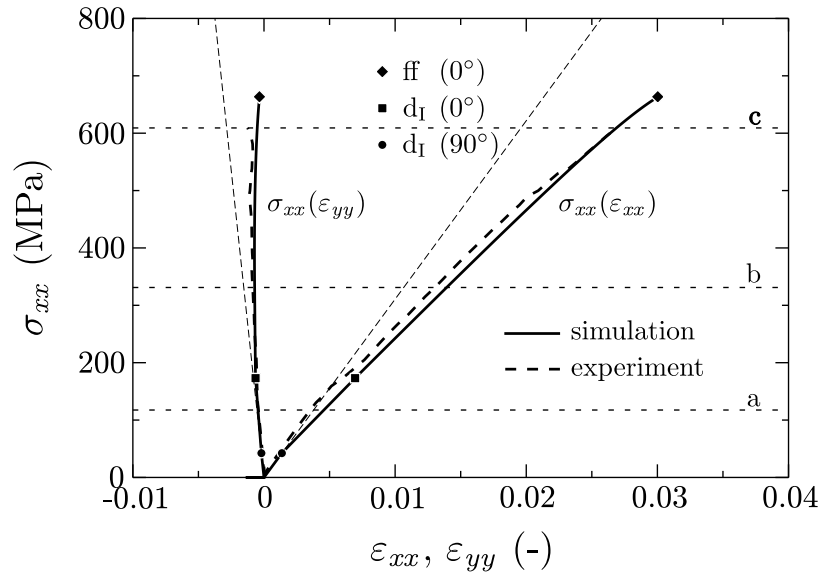


Figure 4.14: Test case 7 of the first WWFE. Response of a $[0^\circ/90^\circ]_S$ laminate made of glass/epoxy to biaxial tensile loading ($\sigma_{yy} : \sigma_{xx} = 0 : 1$); predictions and experimental results (Soden et al., 2002) are plotted in terms of laminate stress, σ_{yy} , versus laminate strains, ε_{xx} and ε_{yy} .

Test case 7 considers a $[0^\circ/90^\circ]_S$ laminate made of glass/epoxy which is uniaxially loaded, i.e. $\sigma_{yy} : \sigma_{xx} = 0 : 1$. This test case is also addressed by Flatscher et al. (2009c). In contrast to the test cases before, the experimental results are obtained from coupon tests. The response is plotted in Fig. 4.14 in form of applied stress, σ_{xx} , versus the overall laminate strain in loading direction, ε_{xx} , and in direction transverse to the loading, ε_{yy} , respectively. Besides the predicted response (solid line) and the experimental results (dashed line), the linear elastic response (thin dashed line) is shown.

Observations from experimental testing (Soden et al., 2002) concern ‘onset of matrix cracking’ (a), ‘onset of longitudinal splitting’ (b), and ‘fiber failure’ (c). In the simulation onset of damage accumulation (\bullet) is predicted first in the 90° -plies. Note that this load corresponds to the first ply failure load of the laminate, which is again strongly influenced by the residual stresses from curing. At load levels marked by squares (\blacksquare) also the 0° -plies start to experience damage, cf. longitudinal splitting. The ultimate failure of the laminate (\blacklozenge) is predicted due to fracturing fibers in 0° -

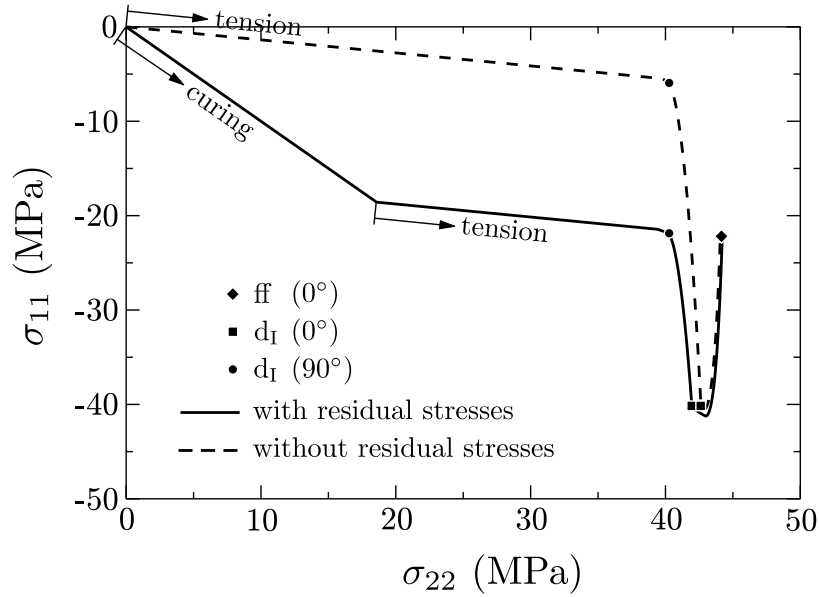


Figure 4.15: Predicted stress path in a 90° -ply of $[0^\circ/90^\circ]_S$ laminate made of glass/epoxy and subjected to uniaxial tension; results with and without accounting for residual stresses from curing.

plies. The agreement between experimental result and prediction is good; also the behavior of the laminate in transverse direction is captured well.

Even though the non-linearity in the overall laminate behavior is not pronounced, the predicted damage accumulation is accompanied by severe stress redistribution. This is demonstrated in Fig. 4.15, where the σ_{11} - σ_{22} stress path predicted in a 90° -ply is plotted. There σ_{11} denotes the ply stress component in fiber direction and σ_{22} denotes the ply stress component in direction transverse to the fibers. The solid line corresponds to a simulation in which residual stresses from curing have been taken into account; the dashed line presents predictions in which residual stresses have been disregarded. Independent of the consideration of residual stresses, the same ply stress state is reached in the 90° -plies when fiber failure occurs in 0° -plies.

Discussion. The agreement between predictions and experimental result is satisfactory. Furthermore, onset of mechanisms such as damage is nicely predicted before noticeably effects are reported in the experiments. However, also some discrepancies have been found. Some discrepancies, of course, may originate from shortcomings of

the model. However, at this point it shall be repeated that the same model with the material data as given in Appendix C was used for all predictions without additional modifications. Another source of errors is the possibly inaccurate material data used for modeling compared to the specifications of the material actually used in testing. Here it should be noted that some of the experimental data has been collected from different investigators. Furthermore, geometrical effects and the boundary conditions prevailing in the experiments might have affected the measured laminate response but they are not accounted for in the simulations. Finally, the experimental results might suffer from errors in measurement as well, particularly due the very demanding experimental setups.

4.3 Test cases from the third WWFE

In the following the predictions to the test cases of the third WWFE are studied although the experimental results are not yet available. For most of the test cases the predicted response is given in terms of stress–strain curves with plot ranges consistent with the required specifications of the WWFE. Additionally, the evolution of the normalized damage variables, i.e. the ratios $\xi_p/\xi_a^{(m)}$, as well as the evolution of the internal hardening variables, κ_i , are plotted if the corresponding mechanism is activated. Note that the mentioned model variables are predicted for individual plies. The (normalized) damage variables should not be interpreted as crack density, however, a non-trivial relation between the damage variables and crack density is expected to exist. The internal hardening variables are equivalent to the corresponding accumulated plastic strain components. For each load case, the condition is given which triggers the simulation to stop.

Calibration. Within the third WWFE the four material systems AS4/3501-6, glass/epoxy, G4-800/5260, and IM7/8552 are considered. From the detailed material data provided within the third WWFE (Kaddour et al., 2010), the ply stiffness of the undamaged material, the parameters defining the thermal behavior, and values of the nominal ply strength are listed in Tabs. C.1, C.2, and C.3, respectively. This data is used directly as model input. Additionally, the parameters which describe Puck’s failure surface are needed. Since these data has not been provided, the slope parameters $p^{(t)}$ and $p^{(c)}$ are estimated following the guidelines given by Puck et al. (2002); the weakening parameters s and m concerning high stress in fiber direction are chosen as suggested by Schürmann (2005). The parameters describing Puck’s failure surface are listed in Table C.4. From the shear stress–shear strain curves under simple (in-plane) shear loading and from the stress–strain curves under uniaxial transverse (in-plane) compression provided within the third WWFE, the parameters of the modified power laws are extracted and summarized in Table C.5. All remaining model parameters, which are estimated according to the procedure proposed in Sect. 3.5, are listed in Table C.6.

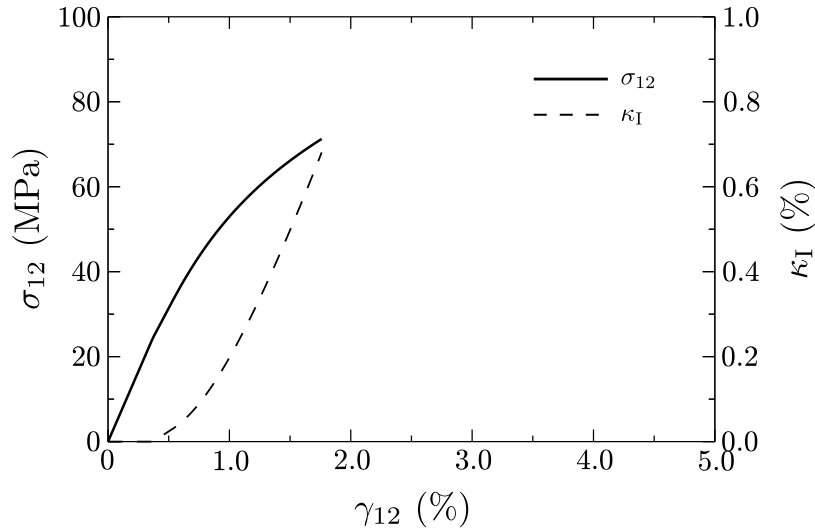


Figure 4.16: Test case 1 of the third WWFE. Shear loading of a UD laminate made of AS4/3501-6 under presence of a constant transverse tensile stress of $\sigma_{22} = +14$ MPa; ply shear stress, σ_{12} , and internal hardening variable, κ_1 , plotted versus engineering ply shear strain, γ_{12} .

Test case 1 considers a UD laminate made of AS4/3501-6, which is subjected to a non-proportional load. The loading is composed of a constant transverse tensile stress of $\sigma_{22} = \sigma_{yy} = +14$ MPa and a ramped up shear stress, $\sigma_{12} = \sigma_{xy}$. The predicted laminate response can be seen in Fig. 4.16 where the ply shear stress is plotted versus the engineering shear strain (solid line). The evolution of the internal hardening variable, κ_1 , is also shown with respect to the predicted shear strain.

During loading, plasticity mechanism p_I gets activated at $\sigma_{12} = 25$ MPa resulting in the accumulation of plastic shear strains. The parameter $\mu_1^{(t)}$ affects the predicted response since transverse tensile stresses are present, however, the effect of stress interaction is not pronounced. The simulation is stopped because a matrix exertion of $f_E^{(m)} = 1$ is reached at $\sigma_{12} = 71$ MPa. It is expected that in experimental testing the load cannot be increased significantly beyond this load level. Note that no damage accumulation is predicted for test case 1, but plastic strains accumulate.

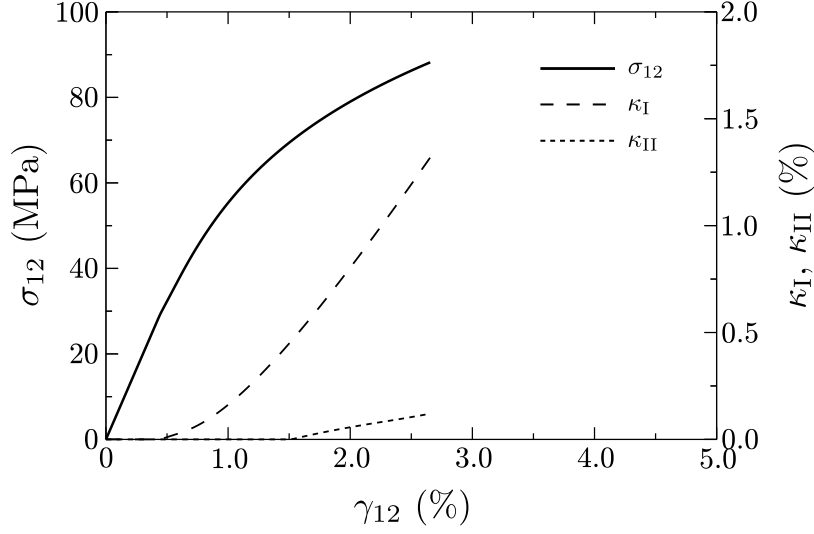


Figure 4.17: Test case 2 of the third WWFE. Shear loading of a UD laminate made of AS4/3501-6 under presence of a constant transverse compressive stress of $\sigma_{22} = -34.5$ MPa; ply shear stress, σ_{12} , and internal hardening variables, κ_I and κ_{II} , plotted versus engineering ply shear strain, γ_{12} .

Test case 2 considers a UD laminate made of AS4/3501-6 which is subjected to a non-proportional load. The loading is composed of a constant transverse compressive stress of $\sigma_{22} = \sigma_{yy} = -34.5$ MPa and a ramped up shear stress, $\sigma_{12} = \sigma_{xy}$. The predicted material response can be seen in Fig.4.17 where the ply shear stress is plotted versus the engineering shear strain of the ply (solid line). The evolution of the internal hardening variables, κ_I and κ_{II} , is also shown with respect to the predicted shear strain.

During loading, plasticity mechanism p_I gets activated at $\sigma_{12} = 30$ MPa. Since $-\sigma_{22}/\tilde{\sigma}_I^{(0)} < \lambda_I$ holds, the normal stresses do not enhance the accumulation of plastic shear strains. However, a matrix exertion of $f_E^{(m)} = 1$ is delayed to higher shear stresses compared to pure shear loading. At a shear load of $\sigma_{12} = 70$ MPa, also plasticity mechanism p_{II} gets activated resulting in the accumulation of plastic normal strains. Stress interaction in mechanism p_{II} is accounted for by the parameter μ_{II} . The simulation is stopped because a matrix exertion of $f_E^{(m)} = 1$ is reached at $\sigma_{12} = 88$ MPa. It is expected that in experimental testing the load cannot be increased significantly beyond this load level. Similar to the test case before no damage accumulation is predicted but plastic strains accumulate.

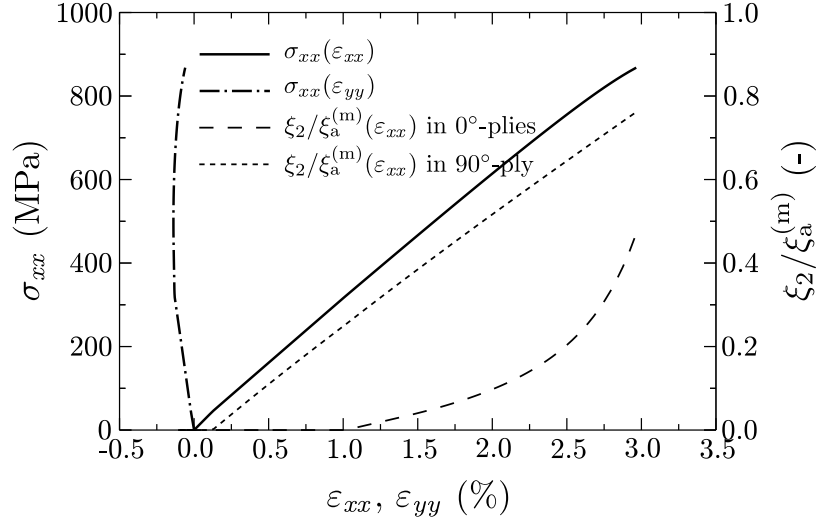


Figure 4.18: Test case 3 of the third WWFE. Uniaxial loading of a laminate, layup $[0^\circ/90^\circ/0^\circ]$, ply thickness $t_p = 0.125$ mm, material system glass/epoxy; the loading direction coincides with the orientation of fibers in 0° -plies and with the x -axis; laminate stress, σ_{xx} , plotted versus predicted laminate strains, ε_{xx} and ε_{yy} ; normalized damage variables, $\xi_2/\xi_a^{(m)}$, predicted for 0° -plies and 90° -ply plotted versus laminate strain, ε_{xx} (the plot range is not consistent with the required specifications).

Test case 3 considers a $[0^\circ/90^\circ/0^\circ]$ laminate made of glass/epoxy. The ply thickness is $t_p = 0.125$ mm. The laminate is uni-axially loaded; the direction of the applied tensile load coincides with the fiber direction in 0° -plies, i.e. the x -direction. The predicted laminate response can be seen in Fig.4.18, where the laminate stress is plotted versus the laminate strains in loading direction (solid line) and transverse direction (chain dotted line). The evolution of the normalized damage variables, $\xi_2/\xi_a^{(m)}$, is plotted versus the laminate strain in loading direction.

During loading, damage mechanism d_I gets activated at $\sigma_{xx} = 47$ MPa in the 90° -plies. Nevertheless, this damage accumulation has almost no effect on the predicted laminate response. At a load of $\sigma_{xx} = 317$ MPa, also the 0° -plies experience matrix damage (d_I) due to constrained Poisson effects. The latter mechanism primarily affects the predicted strain in transverse direction. The simulation is stopped because a fiber exertion of $f_E^{(f)} = 1$, i.e. fiber failure is predicted in the 0° -plies at $\sigma_{xx} = 868$ MPa. This is associated with ultimate failure.

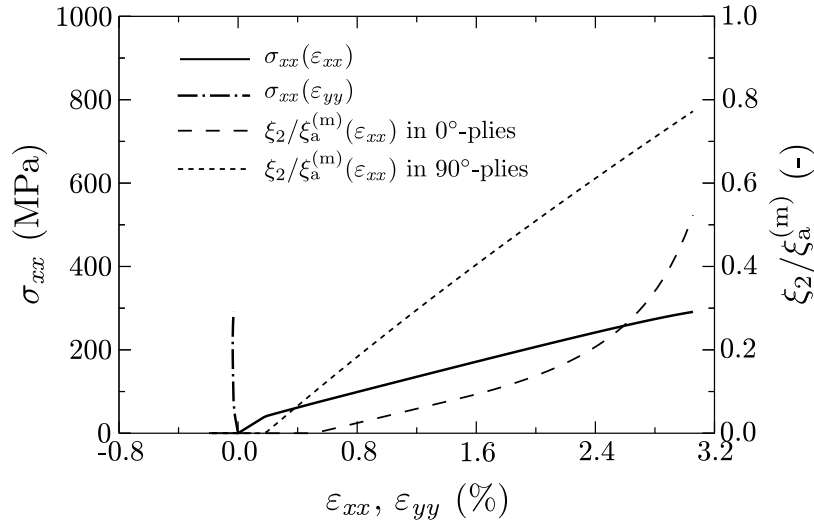


Figure 4.19: Test case 4 of the third WWFE. Uniaxial loading of a laminate, layup $[0^\circ/90^\circ_8/0^\circ]$, ply thickness $t_p = 0.125$ mm, material system glass/epoxy; the loading direction coincides with the orientation of fibers in 0° -plies and with the x -axis; laminate stress, σ_{xx} , plotted versus predicted laminate strains, ε_{xx} and ε_{yy} ; normalized damage variables, $\xi_2/\xi_a^{(m)}$, predicted for 0° -plies and 90° -plies plotted versus laminate strain, ε_{xx} .

Test case 4 considers a $[0^\circ/90^\circ_8/0^\circ]$ laminate made of glass/epoxy. The ply thickness is $t_p = 0.125$ mm. The laminate is uniaxially loaded; the direction of the applied tensile load coincides with the fiber direction in 0° -plies, i.e. the x -direction. The predicted laminate response can be seen in Fig. 4.19 where the laminate stress is plotted versus the laminate strains in loading (solid line) and transverse direction (chain dotted line). The evolution of the normalized damage variables, $\xi_2/\xi_a^{(m)}$, is plotted versus the predicted laminate strain in loading direction.

The onset of damage accumulation (d_I) at $\sigma_{xx} = 42$ MPa in the 90° -plies causes a severe reduction in the laminate stiffness. At a load of $\sigma_{xx} = 74$ MPa, also the 0° -plies experience damage (d_I). This has some effect on the predicted strain in transverse direction. No plastic strains are predicted in test case 4. The simulation is stopped because a fiber exertion of $f_E^{(f)} = 1$ is reached in the 0° -plies at $\sigma_{xx} = 291$ MPa. This is associated with ultimate failure of the laminate.

Test case 5 considers a $[0_2^{\circ}/90^{\circ}]_{2S}$ laminate made of AS4/3501-6. The ply thickness is $t_p = 0.125$ mm. Test case 5 aims at the variation of the coefficients of thermal expansion (CTEs) of a laminate with crack density (or with the amount of damage). No information on the loading scenario under which the cracks are to be formed is provided. Furthermore, the quantity ‘crack density’ neither defines clearly the damage state of a laminate nor the damage state of a ply. Thus, the following approach is chosen.

First of all, the laminate is cooled down from the stress free temperature of $T_{sf} = 177^{\circ}\text{C}$ to the room temperature of 20°C in order to account for residual stresses at ply level. Second, damage accumulation is triggered by subjecting the laminate to a further change of temperature, ΔT (with respect to room temperature), or by subjecting the laminate to uniaxial tensile stresses in x -direction and y -direction, respectively. The material parameters are assumed to be temperature independent although unreasonable large changes of temperature up to $\Delta T = -273$ K are considered. In case of the tensile loadings, $\sigma_{xx} < 1300$ MPa and $\sigma_{yy} < 545$ MPa is maintained to avoid the prediction of a fiber exertion of $f_E^{(f)} = 1$, i.e. of fiber failure. After damage accumulation caused by the tensile loading, the laminate is unloaded again. For all the selected loading scenarios, the predicted damage originates from the activation of mechanism d_I . Finally, a temperature load of $\Delta T = +1$ K is applied for the prediction of the CTEs in x -direction and y -direction.

In Fig. 4.20, the predicted CTEs of the laminate are plotted versus the applied temperature change. The evolution of the normalized damage variables, $\xi_2/\xi_a^{(m)}$, is also shown. At a temperature change of $\Delta T = 0$ K, i.e. at room temperature, the CTEs of the undamaged laminate can be seen since stresses from curing are too low to trigger damage accumulation. At an applied temperature change of $\Delta T \approx -20$ K, damage (d_I) starts to accumulate in 90° -plies and primarily affects the predicted CTE in x -direction, α_{xx} . Starting from a temperature change of $\Delta T \approx -40$ K, also 0° -plies experience damage (d_I). The latter mechanism primarily affects the predicted CTE in y -direction, α_{yy} . As can be seen in Fig. 4.20, damage accumulation results in a decrease of the CTEs of the laminate.

The predicted laminate’s CTEs are plotted versus the tensile stresses in x -direction applied in the load excursion in Fig. 4.21 and versus the tensile stresses in y -direction applied in the load excursion in Fig. 4.22, respectively. In Fig. 4.21 and Fig. 4.22, also

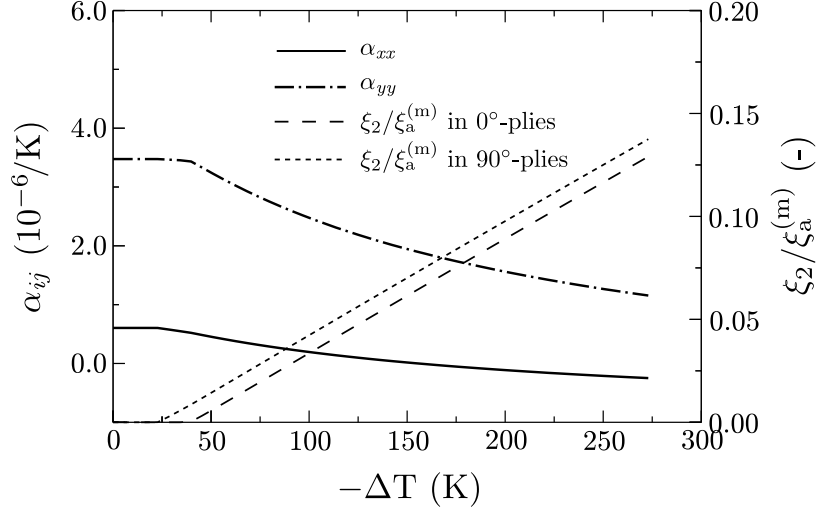


Figure 4.20: Test case 5 of the third WWFE. Influence of damage on the laminate's coefficients of thermal expansion, layup $[0_2^{\circ}/90^{\circ}]_{2S}$, ply thickness $t_p = 0.125$ mm, material system AS4/3501-6; the x -axis coincides with the fiber orientation in 0° -plies; predicted coefficients of thermal expansion of the laminate, α_{xx} and α_{yy} , and normalized damage variables, $\xi_2/\xi_a^{(m)}$, predicted for 0° -plies and 90° -plies plotted versus applied temperature difference, ΔT (the plot range is not consistent with the required specifications).

the evolution of the normalized damage variables is shown. As before, an increasing amount of damage gives rise to decreasing CTEs, whereas, damage accumulation in 90° -plies primarily affects the predicted CTE in x -direction, α_{xx} . Damage accumulation in 0° -plies primarily affects the predicted CTE in y -direction, α_{yy} .

In Fig. 4.23, the predicted CTEs of the laminate are plotted versus a laminate averaged normalized damage variable, $\check{\xi}^{(m)}/\xi_a^{(m)}$. The averaged damage variable in the laminate is computed with respect to the damage variables predicted for the plies by

$$\check{\xi}^{(m)} = \frac{2}{3}\xi_2^{(0^{\circ}\text{-plies})} + \frac{1}{3}\xi_2^{(90^{\circ}\text{-plies})}, \quad (4.1)$$

in the sense of thickness weighting. In Fig. 4.23 it becomes obvious that both predicted CTEs are affected by damage accumulation. The influence of the loading type which causes the damage, however, is not pronounced since the finally reached ply stress states are similar.

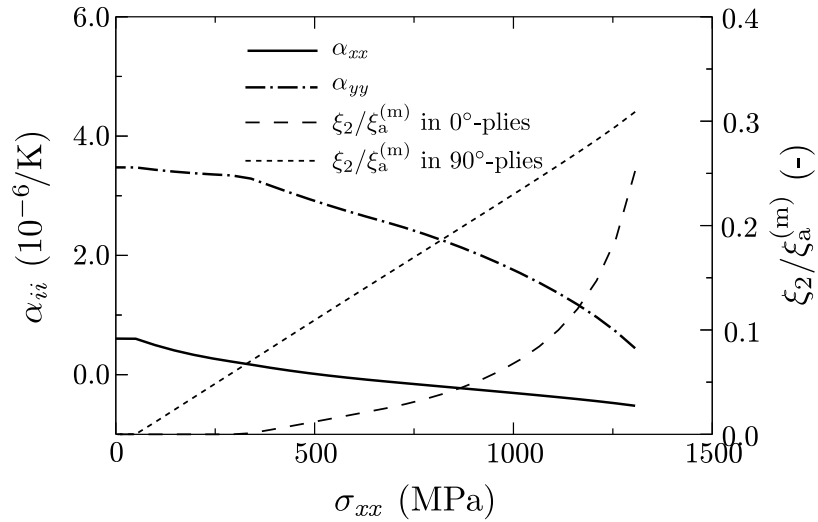


Figure 4.21: Test case 5 of the third WWFE. Influence of damage on the laminate's coefficients of thermal expansion, layup $[0_2^{\circ}/90^{\circ}]_{2S}$, ply thickness $t_p = 0.125$ mm, material system AS4/3501-6; the x -axis coincides with the fiber orientation in 0° -plies; coefficients of thermal expansion predicted for the laminate, α_{xx} and α_{yy} , and normalized damage variables, $\xi_2/\xi_a^{(m)}$, predicted for 0° -plies and 90° -plies plotted versus the laminate stress, σ_{xx} , applied in the load excursion (the plot range is not consistent with the required specifications).

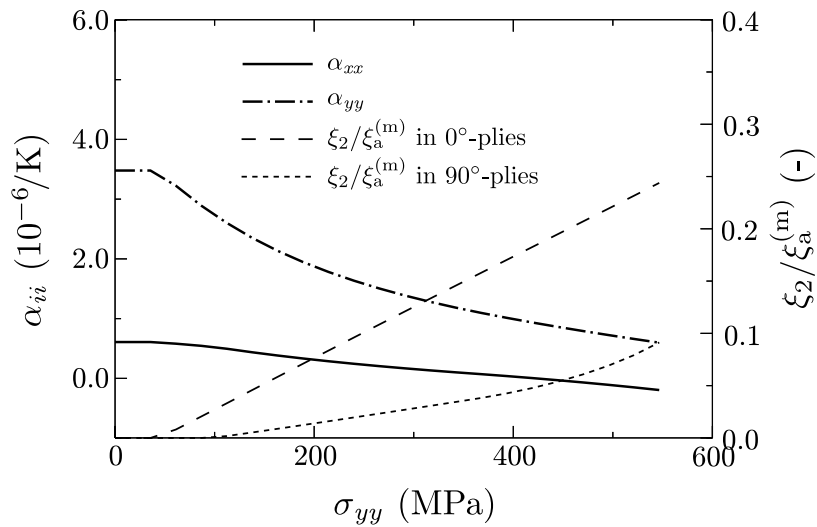


Figure 4.22: Test case 5 of the third WWFE. Influence of damage on the laminate's coefficients of thermal expansion, layup $[0_2^\circ/90^\circ]_{2S}$, ply thickness $t_p = 0.125$ mm, material system AS4/3501-6; the x -axis coincides with the fiber orientation in 0° -plies; predicted coefficients of thermal expansion of the laminate, α_{xx} and α_{yy} , and normalized damage variables, $\xi_2/\xi_a^{(m)}$, predicted for 0° -plies and 90° -plies plotted versus the laminate stress, σ_{yy} (the plot range is not consistent with the required specifications).

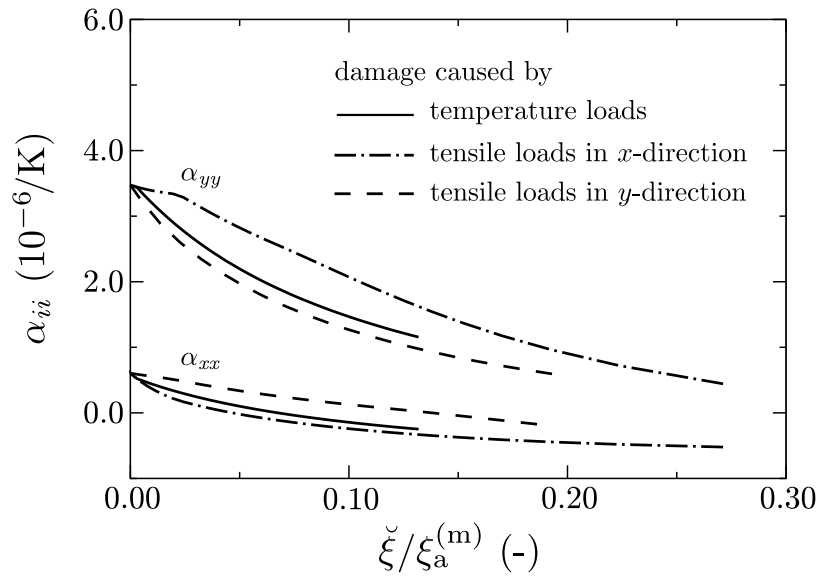


Figure 4.23: Test case 5 of the third WWFE. Influence of damage caused by various types of loads on the laminate's coefficients of thermal expansion, layup $[0_2^{\circ}/90^{\circ}]_{2S}$, ply thickness $t_p = 0.125$ mm, material system AS4/3501-6; the x -axis coincides with the fiber orientation in 0° -plies; predicted coefficients of thermal expansion of the laminate, α_{xx} and α_{yy} , plotted versus the normalized damage variable within the laminate, $\check{\xi}^{(m)}/\xi_a^{(m)}$.

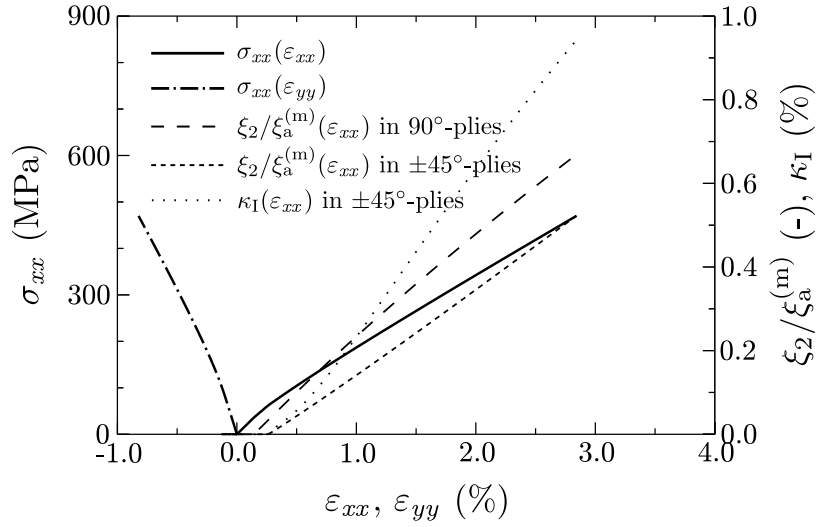


Figure 4.24: Test case 6 of the third WWFE. Uniaxial loading of a laminate, layup $[0^\circ/90^\circ/-45^\circ/+45]_S$, ply thickness $t_p = 0.5$ mm, material system glass/epoxy; the loading direction coincides with the orientation of fibers in 0° -plies and with the x -axis; laminate stress, σ_{xx} , plotted versus predicted laminate strains, ε_{xx} and ε_{yy} ; normalized damage variables, $\xi_2/\xi_a^{(m)}$, predicted for 90° -plies and $\pm 45^\circ$ -plies plotted versus laminate strain, ε_{xx} ; internal hardening variable, κ_I , predicted for $\pm 45^\circ$ -plies plotted versus laminate strain, ε_{xx} .

Test case 6 considers a $[0^\circ/90^\circ/-45^\circ/+45]_S$ laminate made of glass/epoxy with a ply thickness of $t_p = 0.5$ mm. The laminate is loaded by uniaxial tension. The predicted laminate response can be seen in Fig. 4.24 where the laminate stress is plotted versus the laminate strains in loading (solid line) and transverse direction (chain dashed line). The evolution of the normalized damage variables, $\xi_2/\xi_a^{(m)}$, and of the internal hardening variable, κ_I , are plotted versus the predicted strain in loading direction.

At a tensile load of $\sigma_{xx} = 40$ MPa, damage (d_I) starts to accumulate in 90° -plies. At a load of $\sigma_{xx} \approx 65$ MPa, both plastic strains (p_I) and damage (d_I) start to accumulate in the $\pm 45^\circ$ -plies. The activation of the mentioned mechanisms has some impact on the laminate response, i.e. a slightly decreased laminate stiffness is predicted. The simulation is stopped because of predicted fiber failure, i.e. a fiber exertion of $f_E^{(f)} = 1$ is reached in the 0° -plies at $\sigma_{xx} = 470$ MPa. It is expected that in experimental testing the applied stress cannot be increased beyond this load level.

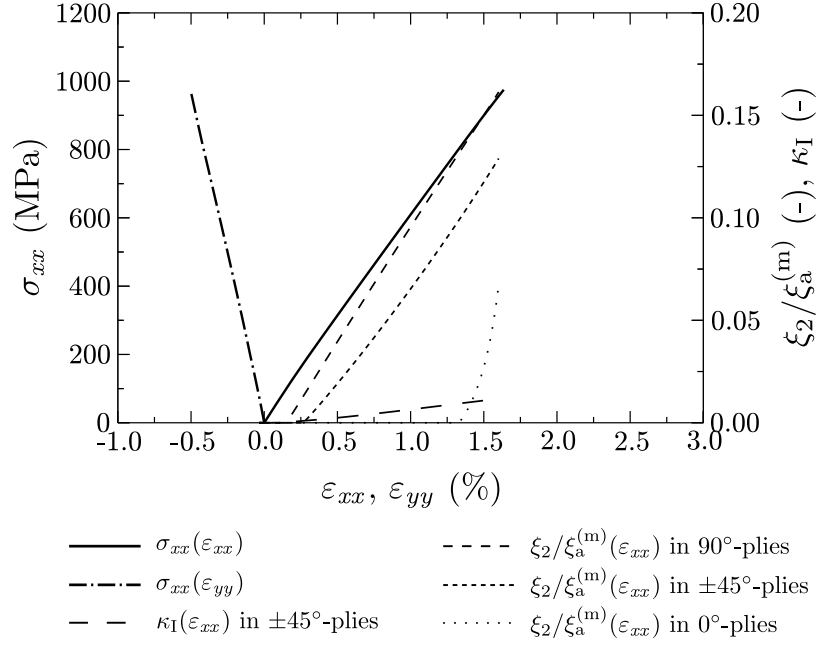


Figure 4.25: Test case 7 and 8 of the third WWFE. Uniaxial loading of laminates, layups $[0^\circ / -45^\circ / +45^\circ / 90^\circ]_S$ and $[+45^\circ / 0^\circ / 90^\circ / -45^\circ]_S$, ply thickness $t_p = 0.14$ mm, material system G4-800/5260; the loading direction coincides with the orientation of fibers in 0° -plies and with the x -axis; laminate stress, σ_{xx} , plotted versus predicted laminate strains, ε_{xx} and ε_{yy} ; internal hardening variables, κ_I , predicted for $\pm 45^\circ$ -plies plotted versus laminate strain, ε_{xx} ; normalized damage variables, $\xi_2/\xi_a^{(m)}$, predicted for 90° -plies, $\pm 45^\circ$ -plies, and 0° -plies plotted versus laminate strain, ε_{xx} .

Test cases 7 and 8 focus on uniaxially loaded laminates made of the material system G4-800/5260. For test case 7, a $[0^\circ / -45^\circ / +45^\circ / 90^\circ]_S$ layup, for test case 8, a $[+45^\circ / 0^\circ / 90^\circ / -45^\circ]_S$ layup is defined. The ply thickness is $t_p = 0.14$ mm in both test cases.

The effect of the stacking sequence is not captured explicitly in the present model. Thus, the same stress–strain curves are predicted for both test cases, cf. Fig. 4.25. Also the evolution of the normalized damage variables, $\xi_2/\xi_a^{(m)}$, and the evolution of the internal hardening variable, κ_I , are plotted versus the predicted strain in loading direction.

At a tensile load of $\sigma_{xx} = 64$ MPa, plasticity mechanism p_I is activated which results in the evolution of little plastic shear strains in the $\pm 45^\circ$ -plies. Consecutively, the 90° -plies ($\sigma_{xx} = 129$ MPa), the $\pm 45^\circ$ -plies ($\sigma_{xx} = 193$ MPa), and the 0° -plies ($\sigma_{xx} = 825$ MPa) experience damage (d_I). Finally, the simulation is stopped because fiber failure is predicted, i.e. a fiber exertion of $f_E^{(f)} = 1$ is reached in the 0° -plies at a tensile load of $\sigma_{xx} = 975$ MPa which is associated with ultimate failure of the laminate. Although various mechanisms are activated, the predicted response of the laminate is almost linear.

Test case 9 focuses on a $[+30^\circ/90^\circ/-30^\circ/90]_S$ laminate made of glass/epoxy. The ply thickness is $t_p = 0.25$ mm. The participants of the third WWFE are asked to apply a laminate bending moment M_{xx} . As long as Poisson effects are neglected, such a bending moment causes bending deformation with respect to the y -axis and, furthermore, induces laminate stresses σ_{xx} only. The experimental data may be measured from four point bending tests, but no corresponding geometrical information is provided. Hence, the following two simulations are carried out considering infinite plates but different boundary conditions.

In the first simulation, $M_{yy} = 0$ is assured as the Poisson effects are not constrained and also the bending of the plate with respect to the x -axis is simulated. These boundary conditions give rise to a deformed shape of a hyperbolic type and are referred to as ‘type 1’. By this approach, constraints in the experiment possibly caused by loading and supporting devices are not taken into account. In the second simulation, the boundary conditions are chosen such that bending of the plate with respect to the x -axis is suppressed. Consequently, these boundary conditions induce an additional (reaction) bending moment $M_{yy} > 0$ and, therefore, strongly constrain the deformation of the plate. These boundary conditions are referred to as ‘type 2’.

The predicted response of the plate is shown for the boundary conditions of type 1 in Fig. 4.26 and the boundary conditions of type 2 in Fig. 4.27. In both cases, the bending moment per unit width of the laminate is plotted versus the normal surface strains in the x -direction and the y -direction. Both surfaces A ($\sigma_{xx} > 0$) and B ($\sigma_{xx} < 0$) of the plate are considered. Additionally, unloading curves are shown. The evolution of damage variables and of the internal hardening variables are not shown.

If the boundary conditions of type 1 are applied, all mechanisms, i.e. d_I , d_{II} , p_I , and p_{II} , get activated during bending of the laminate. The simulation is already stopped at $M_{xx} = 331$ Nm/m because fiber failure, i.e. a fiber exertion of $f_E^{(f)} = 1$, is predicted in the ‘compressed’ -30° -ply.

The situation is very similar when the boundary conditions of type 2 are applied, although the plate shows much stiffer behavior. Nevertheless, the simulation is stopped at $M_{xx} = 369$ Nm/m (where a reaction bending moment of $M_{yy} = 108$ Nm/m is induced) because fiber failure, i.e. a fiber exertion of $f_E^{(f)} = 1$, is predicted in the ‘compressed’ 30° -ply. In Table 4.2 one can see for both types of boundary conditions

which mechanisms are predicted to be active when the load level corresponding to fiber failure is reached.

It is not obvious from the predictions of the present model whether the bending moment can be increased beyond this magnitude of loading, at least the occurrence of delaminations and severe disintegration of the laminate is expected. From the unloading curves at an intermediate load level it can be seen that the plate will remain curved after unloading. This effect is not that pronounced when the boundary conditions of type 2 are utilized. From the simulations it can be concluded, that the boundary conditions which are employed in the experimental testing will strongly influence the measurements. For more specific predictions, detailed geometrical data of the experimental setup should be used.

Table 4.2: Test case 10 of the third WWFE. Active (1) and not active (0) mechanisms predicted with type 1/type 2 boundary conditions when the load level corresponding to fiber failure is reached.

		d_I	d_{II}	p_I	p_{II}
tension	+30°-ply	1/1	0/0	1/1	0/0
	90°-ply	1/1	0/0	1/0	0/0
	-30°-ply	0/1	0/0	1/1	0/0
	90°-ply	1/1	0/0	1/0	0/0
compression	90°-ply	0/0	0/0	0/0	0/0
	-30°-ply	1/0	0/0	1/1	0/0
	90°-ply	1/1	1/1	1/0	1/1
	+30°-ply	1/1	1/1	1/1	1/1

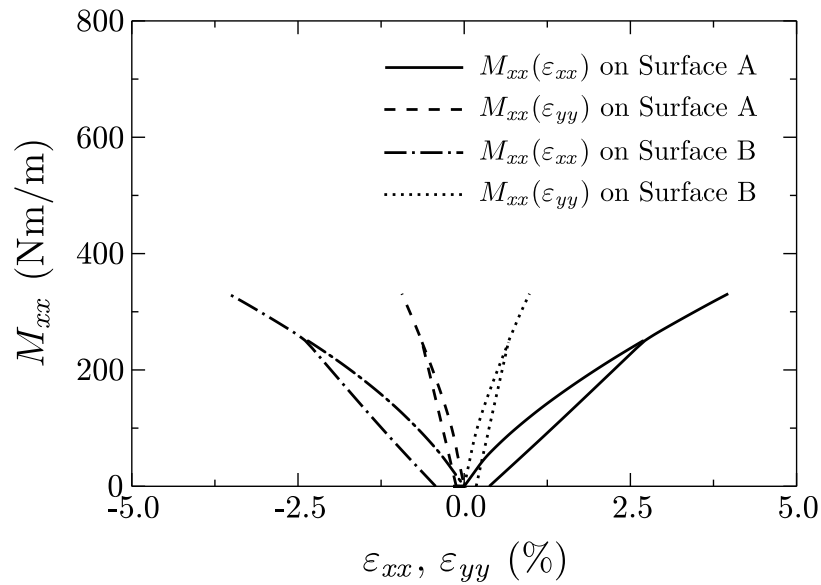


Figure 4.26: Test case 9 of the third WWFE. Bending of a laminated plate, layup $[+30^\circ/90^\circ/-30^\circ/90]_S$, ply thickness $t_p = 0.25$ mm, material system glass/epoxy; infinite plate with boundary conditions of type 1 ($M_{yy} = 0$), the deformed shape is of hyperbolic type; the x -axis coincides with the fiber orientation in 0° -plies; bending moment, M_{xx} , plotted versus surface strains, ε_{xx} and ε_{yy} , predicted for plate surfaces A and B.

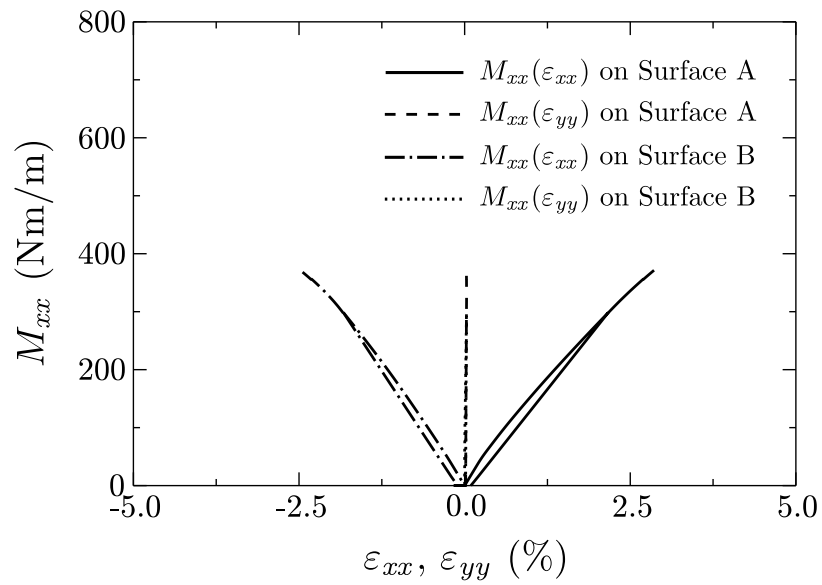


Figure 4.27: Test case 9 of the third WWFE. Bending of a laminated plate, layup $[+30^\circ/90^\circ/-30^\circ/90^\circ]_S$, ply thickness $t_p = 0.25$ mm, material system glass/epoxy; infinite plate with boundary conditions of type 2 ($M_{yy} > 0$), the deformed shape is of cylindrical type; the x -axis coincides with the fiber orientation in 0° -plies; bending moment, M_{xx} , plotted versus surface strains, ε_{xx} and ε_{yy} , predicted for plate surfaces A and B.

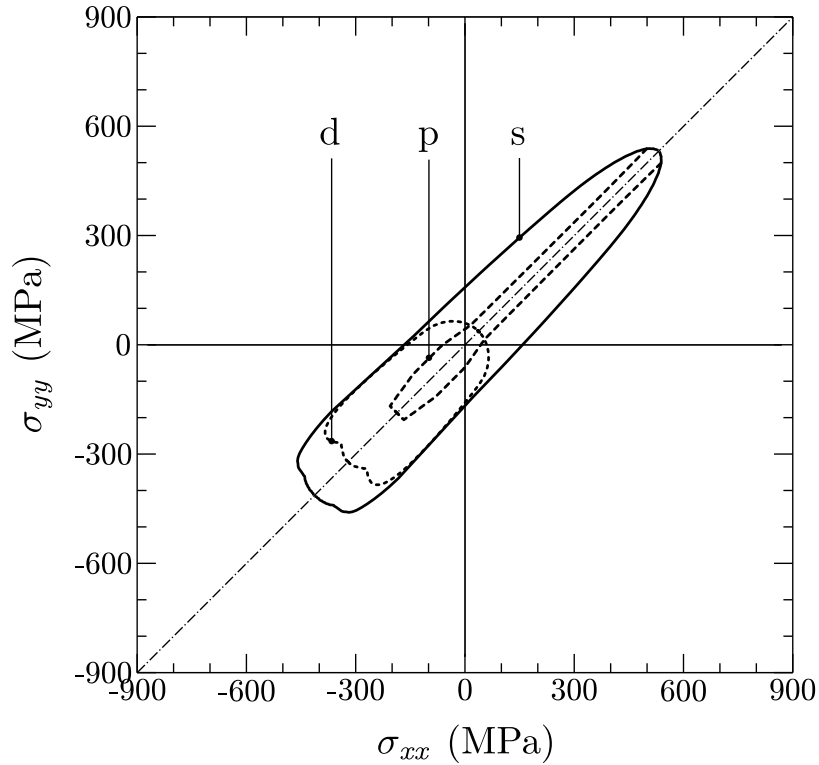


Figure 4.28: Test case 10 of the third WWFE. Biaxial damage and failure envelopes of a laminate, layup $[\pm 45^\circ]_S$, ply thickness $t_p = 0.25$ mm, material system glass/epoxy; the envelope illustrates the onset of damage (d), onset of plastic strain accumulation (p), and the simulation stop (s) with respect to laminate stresses; only one symmetric half of each envelope is shown, the other half is replaced by several prescribed loading paths.

Test case 10 considers a $[\pm 45^\circ]_S$ laminate made of glass/epoxy. The ply thickness is $t_p = 0.25$ mm. The laminate is subjected to proportional (in stress space) biaxial loads and the participants are asked to plot damage onset envelopes and failure envelopes. The predictions are given with respect to laminate stresses in Fig. 4.28 and with respect to laminate strains in Fig. 4.29. The envelopes depict the onset of damage (either one of mechanism d_I or d_{II}), the onset of plastic strain accumulation (either one of mechanism p_I or p_{II}), and the state where the simulations are stopped. All simulations are stopped because the allowable amount of damage is reached.

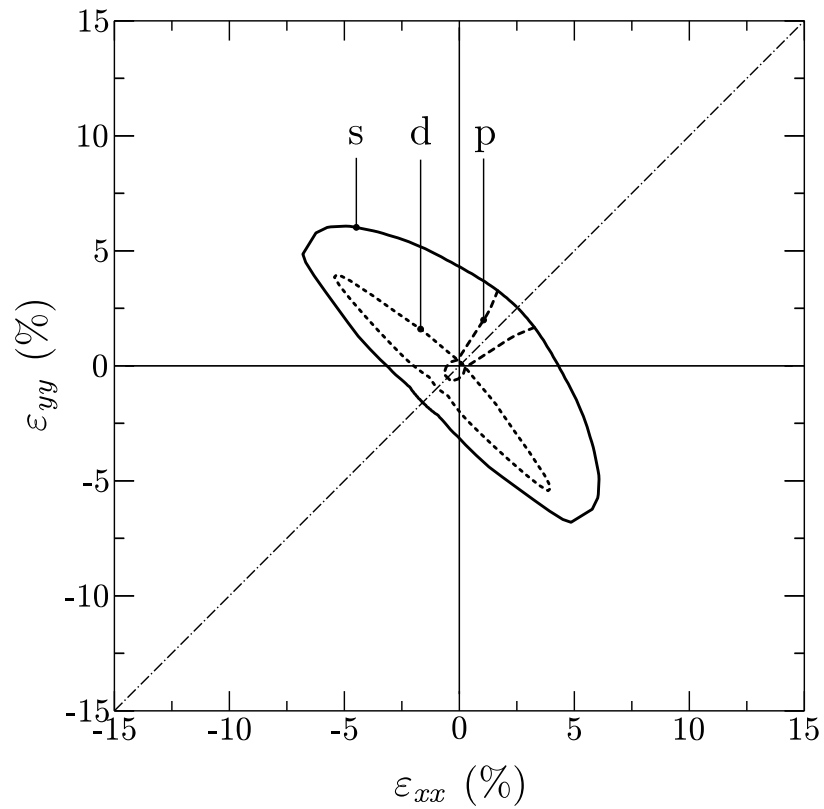


Figure 4.29: Test case 10 of the third WWFE. Biaxial damage and failure envelopes of a laminate, layup $[\pm 45^\circ]_s$, ply thickness $t_p = 0.25$ mm, material system glass/epoxy; the envelope illustrates the onset of damage (d), onset of plastic strain accumulation (p), and the simulation stop (s) with respect to laminate strains; only one symmetric half of each envelope is shown, the other half is replaced by several strain paths which result from the radial stress loadings.

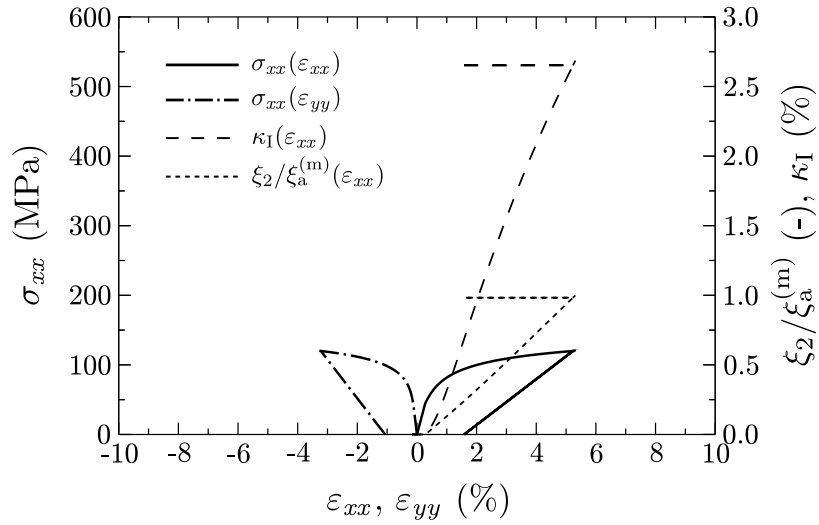


Figure 4.30: Test case 11 of the third WWFE. Uniaxial loading, unloading, and reloading of a laminate, layup $[\pm 50^\circ]_{3S}$, ply thickness $t_p = 0.2$ mm, material system glass/epoxy; laminate stress, σ_{xx} , plotted versus predicted laminate strains, ε_{xx} and ε_{yy} ; internal hardening variable, κ_I , and normalized damage variable, $\xi_2/\xi_a^{(m)}$, plotted versus laminate strain, ε_{xx} .

Test case 11 considers a $[\pm 50^\circ]_{3S}$ laminate made of glass/epoxy. The ply thickness is $t_p = 0.2$ mm. First, the laminate is subjected to a uniaxial tensile stress of $\sigma_{xx} = 120$ MPa. Subsequently, the laminate is unloaded and loaded again until failure is predicted. The predicted laminate response is shown in Fig. 4.30 where the laminate stress is plotted versus the laminate strain in loading (solid line) and transverse direction (chain dashed line). The evolution of the normalized damage variable, $\xi_2/\xi_a^{(m)}$, and the evolution of the internal hardening variable, κ_I , are plotted versus the predicted strain in loading direction. During the first loading, mechanisms p_I ($\sigma_{xx} = 44$ MPa) and d_I ($\sigma_{xx} = 46$ MPa) get activated at almost the same load level. At a load of $\sigma_{xx} = 120$ MPa, already a considerable amount of damage and large plastic shear strains have accumulated. During unloading and reloading up to a loading of $\sigma_{xx} = 120$ MPa, no change of the model variables is predicted, cf. Fig. 4.30. However, after a further increase of the applied load the allowable amount of damage is reached at $\sigma_{xx} = 120.2$ MPa. At this state of damage, disintegration is expected but a load increase may be possible.

Test cases 12 and 13 are dealing with strength predictions of open hole compression and tension tests, respectively. The material system considered is IM7/8552. For test case 12, a $[+45^\circ/90^\circ/-45^\circ/0]_S$ layup with a ply thickness of $t_p = 0.5$ mm is defined and a variation of the hole diameter is asked for. The width of the specimen is computed from the diameter of the hole by a fixed factor. For test case 13, a $[+45_m^\circ/90_m^\circ/-45_m^\circ/0_m]_S$ layup with m plies of thickness $t_p = 0.125$ mm is defined, the number of plies m is asked to be varied. The diameter of the hole and the width of the plate are constant. For test cases 12 and 13, the loading direction coincides with the fiber direction in 0° -plies.

Test cases 12 and 13, obviously, aim at the investigation of size effects and ply thickness effects. However, as long as the model for distributed damage and plastic strain accumulation is used without the model for localized damage, the same strength values are predicted for all considered geometries. This means that in the case of compression an applied compressive stress of $\sigma_{xx} = -191.5$ MPa results in the first appearance of a predicted fiber exertion of $f_E^{(f)} = 1$ in one Gauss point of a 0° -ply. In the case of tension a critical stress of $\sigma_{xx} = +308$ MPa is predicted in the FEM analysis. These values are not associated with the ultimate failure of the laminate, but the simulations have to be stopped as progressive fiber failure is not accounted for in the simulations. Open hole tension tests including the simulation of damage localization are addressed in more detail in Sect. 4.6, whereby also various layups are studied.

Discussion. In this section the test cases of the third WWFE have been studied. The predictions are presented although some test cases obviously aim at effects such as size effects, which are not incorporated in the actual version of the model. Furthermore, experimental results are not yet available. Hence, the quality of the predictions cannot be assessed at present.

4.4 Mesh dependency

As already outlined in Sect. 3.3, formulations based on standard strain softening continua are known to introduce severe mesh dependency in the predicted structural response. In the present work this unacceptable behavior is alleviated by the simple approach of mesh adjusted softening. Within this approach a characteristic length is incorporated in the modeled stress strain relation, cf. Eqn. (3.23) in Sect. 3.3. The characteristic length can be interpreted as the width of the localization zone in the FEM mesh.

In the following the mesh dependency is addressed via a simple example consisting of a single ply with the dimensions $2a \times a$ subjected to uniaxial tension. The fibers of the single ply are oriented in loading direction, i.e. parallel to the edge of length $2a$. The material properties are taken as given for IM7/8552 in Appendix C. It is important to note that not the process of localization is of interest here but the effect of a localization zone in combination with various FEM discretizations on the predicted response is studied. In order to trigger the strain localization, an imperfection is introduced in the middle of the single ply by reducing the section thickness of elements across the hole ply width. Apart from the case where 3-node triangular shell elements are used, the ply is discretized by 4-node quadrilateral shell elements with reduced integration. In order to avoid hour-glassing, the enhanced hourglass formulation available in **Abaqus** is used. Furthermore, the **Abaqus** option ***STABILIZE** and a whiff of viscous regularization is utilized in order to improve the convergence behavior. Finally, FEM simulations with **Abaqus** in combination with the implemented constitutive model are conducted for several dimensions and for various FEM discretizations. As long as elements with a quadratic shape are used, the influence of the absolute element size and the influence of the orientation of the FEM mesh with respect to the damage zone remain to be studied. This is done in the following.

The first set of simulations addresses mesh size dependency. To this end the dimension of the ply is varied, i.e. $a = 1, 2, 4$ mm is assumed, and each geometry is discretized by three different structured FEM meshes. The respective responses can be seen in Figs. 4.31, 4.32, and 4.33. For the smallest specimen investigated, i.e. 2×1 mm, rather compliant structural response is observed. With increased specimen size snap back behavior is expected but snap back cannot be simulated under displacement

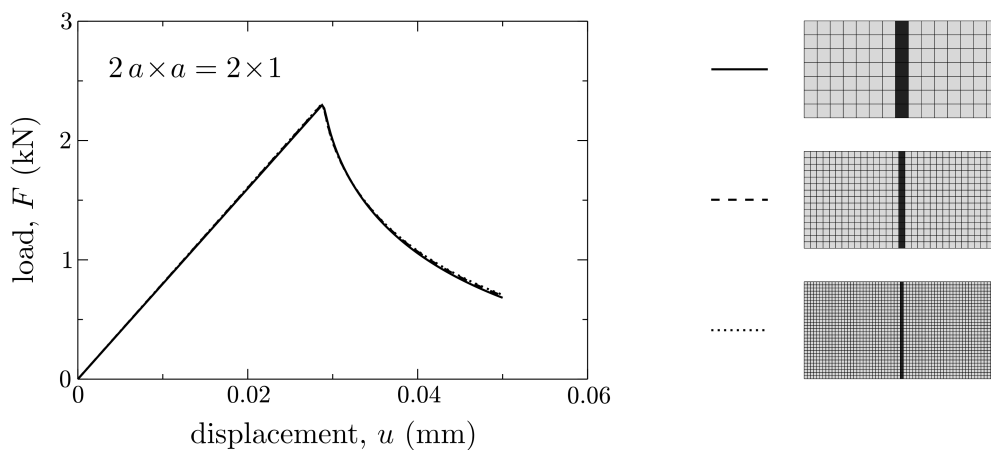


Figure 4.31: Effect of the discretization on the predicted response of a single ply to uniaxial tension; $a = 1$ mm; fibers parallel to the loading direction; localization triggered by a reduced section thickness across entire ply width.

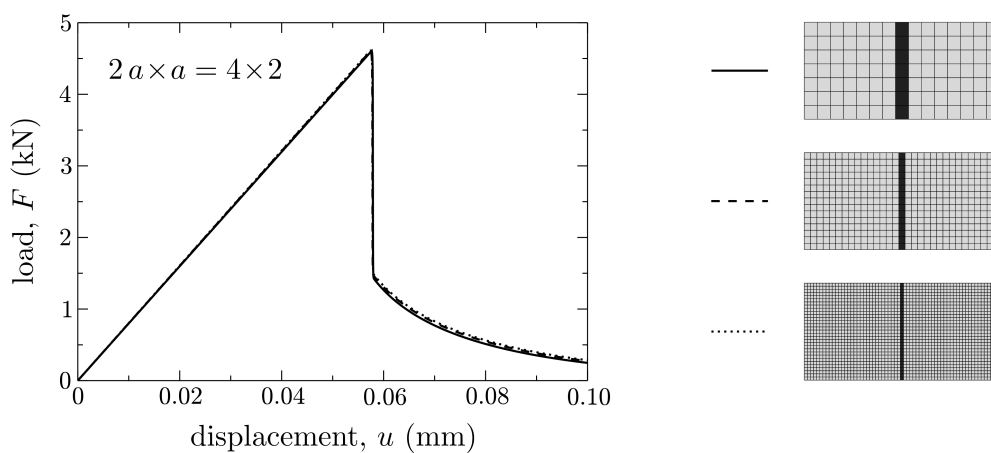


Figure 4.32: Effect of the discretization on the predicted response of a single ply to uniaxial tension; $a = 2$ mm; fibers parallel to the loading direction; localization triggered by a reduced section thickness across entire ply width.

controlled loading in combination with a classical Newton-Raphson algorithms. Consequently, only a sudden drop off in the sustainable load is observed.

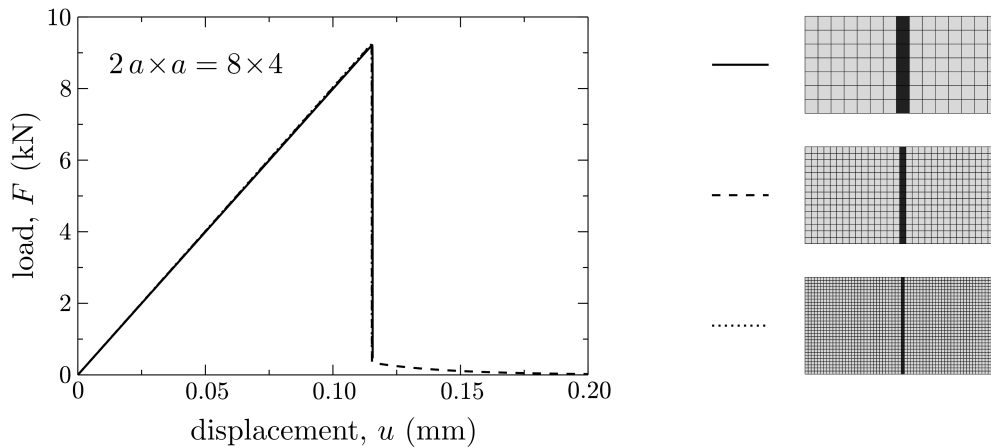


Figure 4.33: Effect of the discretization on the predicted response of a single ply to uniaxial tension; $a = 4$ mm; fibers parallel to the loading direction; localization triggered by a reduced section thickness across entire ply width.

For all specimen dimensions the predicted response is independent of the actual discretization. Obviously, the approach for avoiding mesh dependency works perfect in this simple case.

The second and the third set of the considered simulations address the influence of the orientation of FEM mesh with respect to the damage zone. For this purpose the discretization is varied, whereas the dimension is kept fixed at $a = 1$ mm.

In Fig. 4.34 the response obtained with a ‘biased mesh’ (solid line), a ‘free quad mesh’ (dashed line), and a ‘free trias mesh’ (dashed line) is shown. The influence of the discretization is visible especially for the trias mesh. Note that for the unstructured ‘free quad mesh’ and ‘free trias mesh’ the zone of the introduced imperfection is somewhat wider than the localization zone.

In Fig. 4.35 the response obtained with a ‘structured mesh’ (solid line), a ‘10°-rotated structured mesh’ (dashed line), and a ‘40°-rotated structured mesh’ (dotted line) is shown. Note again, for the ‘10°-rotated structured mesh’ and ‘40°-rotated structured mesh’ the zone of the introduced imperfection is somewhat wider than the localization zone. As expected, a rather pronounced influence of the discretization is observed for the ‘40°-rotated structured mesh’. The main reason for this is that the effective

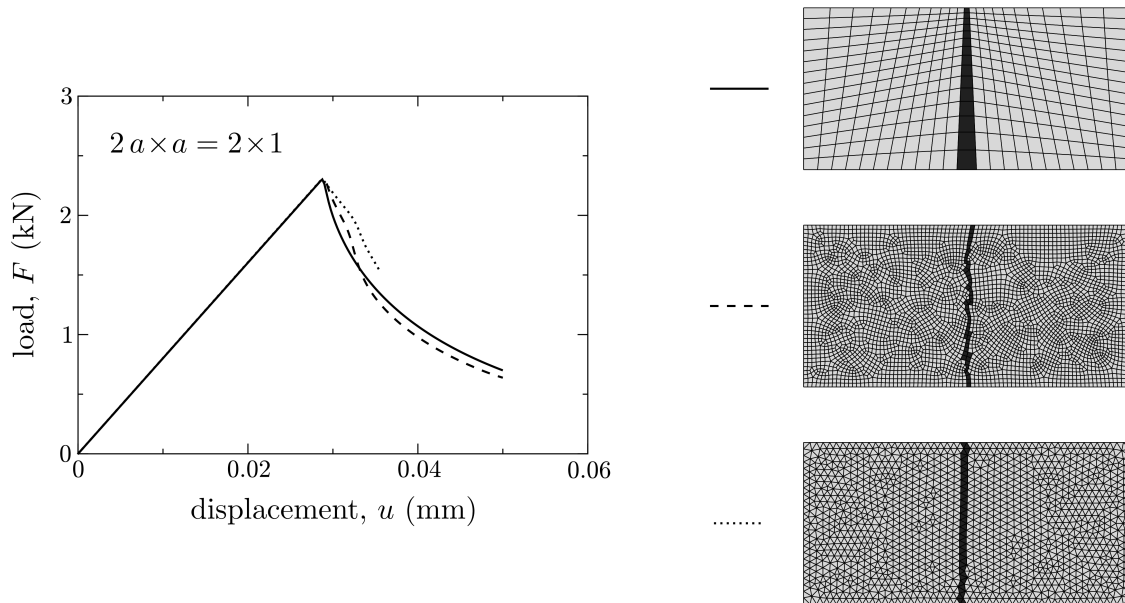


Figure 4.34: Effect of the discretization on the predicted response of a single ply to uniaxial tension; predictions obtained with a ‘biased mesh’ (solid line), a ‘free quad mesh’ (dashed line), and a ‘free trias mesh’ (dotted line); $a = 1$ mm; fibers parallel to the loading direction; localization triggered by a reduced section thickness across entire ply width.

with of the localization band is larger compared to the other cases, and this in turn increases the compliance drastically. In other words, for the latter case the characteristic length used in the stress strain formulation is too small as it does not account for the actual width of the localization zone.

The simple approach for reduction of mesh dependency accounts for the size of the mesh. The orientation of the mesh with respect to the ‘localization zone’ is not accounted for model formulation and, therefore, has some impact on the predictions. However, compared to a standard strain softening continuum the overall mesh dependency is reduced very efficiently.

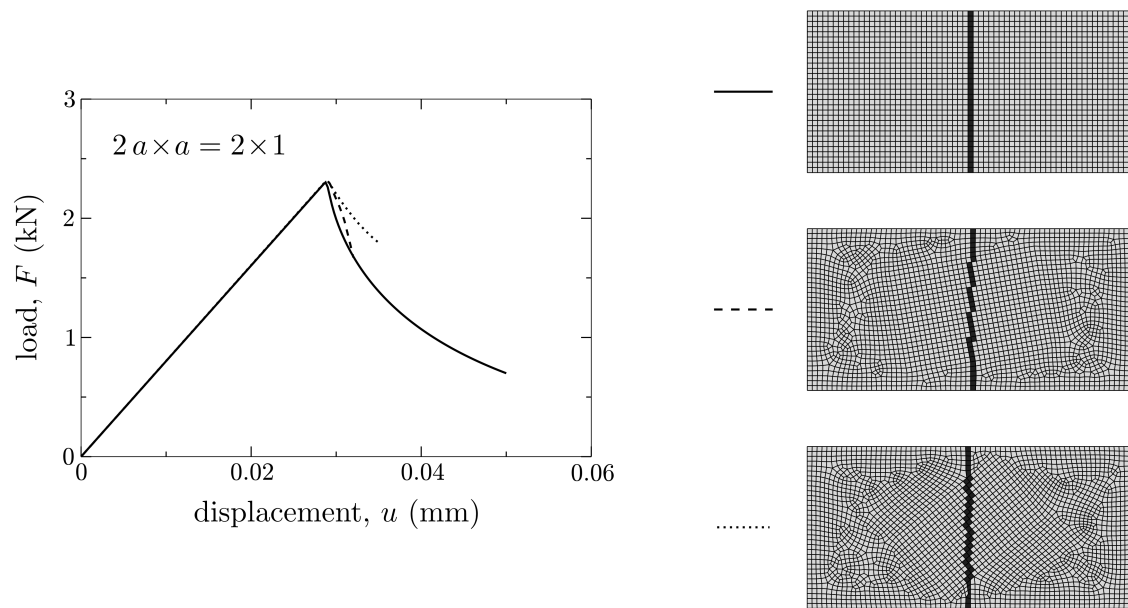


Figure 4.35: Effect of the discretization on the predicted response of a single ply to uniaxial tension; predictions obtained with a ‘structured mesh’ (solid line), a ‘10°-rotated structured mesh’ (dashed line), and a ‘40°-rotated structured mesh’ (dotted line); $a = 1$ mm; fibers parallel to the loading direction; localization triggered by a reduced section thickness across entire ply width.

4.5 Coupon tests

In the present section results from a test campaign are discussed, which is primarily designed to assess the predictive capabilities of the present plasticity model. The test campaign considers angle ply laminates, whereby the major part of the specimens are subjected to compression so that the resulting ply stress states are composed of transverse compressive and in-plane shear stresses. In order to study various stress ratios systematically, four different layups are considered. Apart from the compression tests, also experiments are conducted with emphasis on the influence of the loading history on the laminate behavior. In general, the nonlinear response of the specimen prior to failure is of interest. The test campaign is conducted at the *Polymer Competence Center Leoben GmbH (PCCL)* with specimens produced by *FACC AG*.

Experiments. The experiments are performed with coupons made of unidirectional tapes named Cycom[®]977-2-35/40-12KHTS-134-300, i.e. a carbon fiber reinforced epoxy prepeg with standard modulus fibers. In the following the material system is referred to as Cycom977. Figure 4.36 shows the dimensions of the specimens as well as the orientation of the laminate coordinate system. The considered layups are $[(90)_{16}]_S$, $[(+45/-45)_8]_S$, $[(+60/-60)_8]_S$, and $[(+75/-75)_8]_S$, where the nominal ply thickness is $t_p = 0.125$ mm. This results in a nominal thickness of the coupons of $t = 4.0$ mm. Tabs with a thickness of approximately $t_t = 1.75$ mm are applied in order to reduce stress concentrations caused by the clamping. The tabs are made of glass fiber reinforced polymer (GFRP); the layup of the tabs is $[(+45/-45)_m]$.

In Table 4.3 all performed tests are listed including the dimensions of the respective specimens. Note that the free length, l_f , is chosen such that premature buckling is avoided. With respect to the nomenclature of the tests, the letter specifies the applied loading conditions, i.e. ‘T’ stands for tension and ‘C’ stands for compression. Accordingly, TC means that tension is followed by a compressive loading. The number in the test name refers to the fiber angle of the layup. For each test case five specimens are tested.

The conducted tests consist of three sets. Results of the first set, i.e. T-45 and C-90, are used to calibrate the constitutive model with respect to the material system.

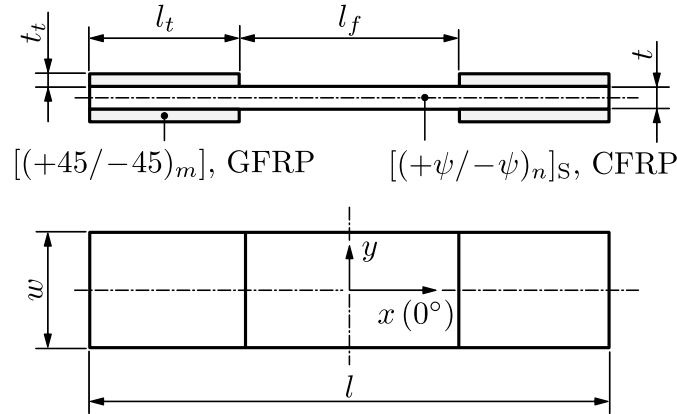


Figure 4.36: Dimensions of the coupon test specimens and definition of the laminate coordinate system.

Results of the second set, i.e. C-45, C-60, and C-75, are mainly used to assess the predictions of the proposed plasticity model. The third set, i.e. TC-45, TC-60, and CT-75, aims at possible effects of the loading history on the material response which have been investigated in the literature very rarely by now. In the present work the measurements of the third set are not compared to the model predictions.

The experimental setup used for the present test campaign is shown in Fig.4.37 (left). The tests are performed with a testing machine *MTS 810*. The strain field was obtained by means of an optical system (*ARAMIS*), which is used to measure

Table 4.3: Nomenclature, layups, and dimensions (mm) of the tested specimens.

Tests	Layups	l	l_f	w	t	t_t
T-45	$[(+45/-45)_8]_S$	240	134	32	4	1.75
C-90	$[(90)_{16}]_S$	130	20	32	4	1.75
C-45, TC-45	$[(+45/-45)_8]_S$	150	56	32	4	1.75
C-60, TC-60	$[(+60/-60)_8]_S$	140	32	32	4	1.75
T-75, C-75, CT-75	$[(+75/-75)_8]_S$	130	20	32	4	1.75

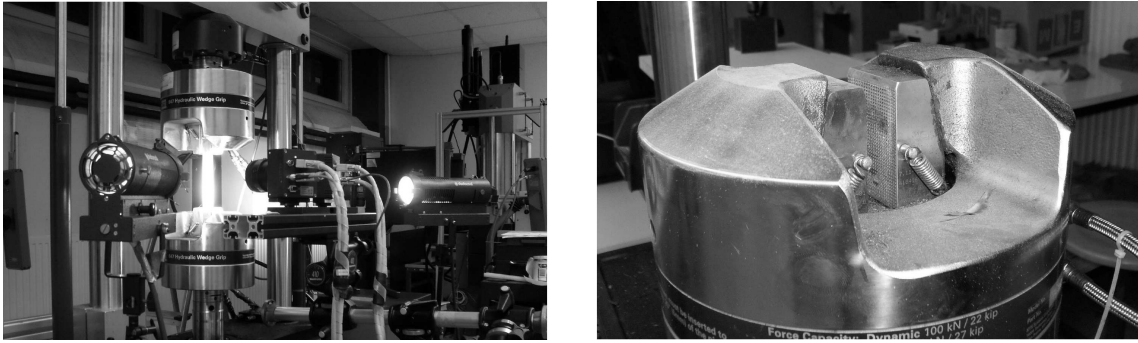


Figure 4.37: Experimental setup at the *PCCL* (left) consisting of testing rig, load cell, hydraulic wedge grips, and optical measurement system, which in turn consists of two cameras, two lamps, and a stand; close-up of the lower hydraulic wedge grip used for clamping of the specimens (right);

in-plane as well as out-of-plane displacements. The measuring window thereby covers the entire specimen width; in loading direction the entire free length if possible but at least one symmetric half is monitored in the compression tests. The specimens are clamped using hydraulic wedge grips, which allow for load reversals without manipulation. The lower grip is shown in Fig. 4.37 (right).

Simulations. In the FEM models only the free length of the specimens is considered and discretized by reduced integrated, eight-noded shell elements. The layups are modeled by means of layered section definitions. With respect to the through-thickness integration, Gauss quadrature with two Gauss points per ply is used. As usual, residual stresses from curing are taken in account by simulating a cooling-down.

To reduce the model size, only one eighth of the specimen is modeled (i.e. half of the width, half of the free length, and half of the thickness) and symmetry boundary conditions are applied. To model the clamping of the specimen, two sets of boundary conditions are studied which represent two possible extreme cases; the boundary conditions prevailing in the experiments are expected to lie somewhere in-between. With the first set of boundary conditions, the displacement in load direction, u_x , is prescribed at the region of clamping; all other degrees of freedom including the rotational ones (ρ_i) are constraint. The resulting model is sketched in Fig. 4.38 (left); the respective boundary conditions shall be referred to as the ‘encastre’ type bound-

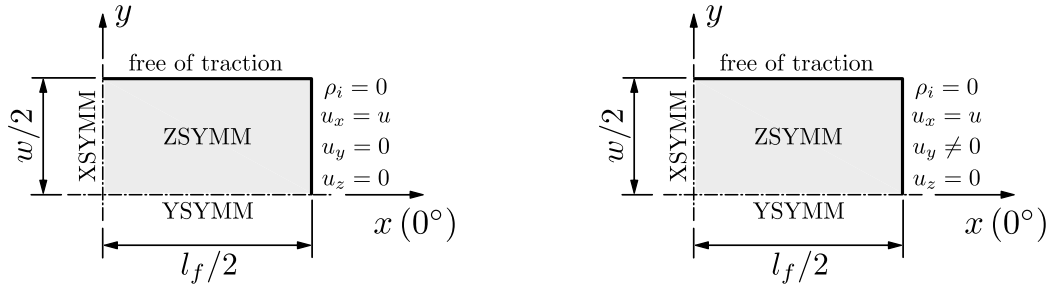


Figure 4.38: Sketch of the model with boundary conditions of type encastre (left) and of type free (right).

ary conditions. The boundary conditions of the second set are similar to the ones before but in-plane deformations transverse to the loading direction, u_y , are not constraint. The resulting model is sketched in Fig. 4.38 (right); the respective boundary conditions shall be referred to as the ‘free’ type boundary conditions.

The present test campaign focuses on the nonlinear specimen response observed prior to ultimate failure but does not draw attention to damage and strain localization. Nevertheless, the localized damage model is applied in the present simulations in order to predict the limit load. However, for the present simulations the limit load predictions might possess approximate character. This is because symmetry conditions are utilized to reduce the model size and because the used mesh is fine but still too coarse to adequately resolve the softening behavior.

Calibration. Before any predictions can be obtained, the constitutive model has to be calibrated with respect to the considered material system Cycom977. To this end the calibration scheme as described in Sect. 3.5 is applied, whereby data provided by *FACC* as well as the results from the tests T-45 (tension of a $[(+45/-45)_8]_S$ coupon) and C-90 (compression of a $[(90)_{16}]_S$ coupon) are used.

Values for the the nominal ply stiffness are listed in Table C.1. The in-plane shear modulus, G_{12} , is extracted from the initial stiffness of the $[(+45/-45)_8]_S$ laminate; the Poisson ratio ν_{12} is estimated. The remaining parameters are provided by *FACC*. As no parameters concerning the thermal behavior are available to the author, respective parameters of another carbon fiber reinforced material system, i.e. IM7/8552, are used. These parameters can be found in Table C.2. Values for the nominal ply

strength are listed in Table C.3. These values are provided by *FACC*, but the (in-plane) shear strength is estimated. The slope parameters $p^{(t)}$ and $p^{(c)}$ of Puck's failure surface are chosen in accordance with the guidelines given by Puck et al. (2002), but the weakening parameters are set to $s = m = 1$ since the model including localized damage is used. The experimental results of the tests T-45 and C-90 are used to calibrate the hardening behavior of the plasticity mechanisms p_I and p_{II} , respectively. These parameters are summarized in Table C.5. All remaining model parameters are set according to the procedure proposed in Sect. 3.5, but the interaction parameter is set to $\mu_I^{(t)} = 0.1$ in order to limit the effect of transverse tensile stresses from curing to a reasonable level. The respective parameters are listed in Table C.6. With respect to the localized damage model, the amount of matrix damage that triggers softening onset is taken to be $\xi_c^{(m)} = 0.015$. For the specific fracture energies the values listed in Table C.7 are used. References concerning these values are given in Sect. 4.6. The parameters of viscous regularization are chosen to be small compared to the simulation (pseudo) time of 1 s, namely $\eta^{(ft)} = \eta^{(fc)} = 2 \cdot 10^{-3}$ s and $\eta^{(mt)} = \eta^{(mc)} = 4 \cdot 10^{-3}$ s.

Some of the material parameters have been roughly estimated, but this way the material model is used as if it was applied in a practical application. Note again that only the results from the tests T-45 and C-90 as well as basic data provided by *FACC* are utilized to calibrate the model. The remaining experimental data is reserved to assess the predictions.

The correlation between experimental results and predictions could be further improved when the material parameters would be determined by an appropriate optimization algorithm in combination with all available test results. However, such a sophisticated calibration procedure is not desired in the present context.

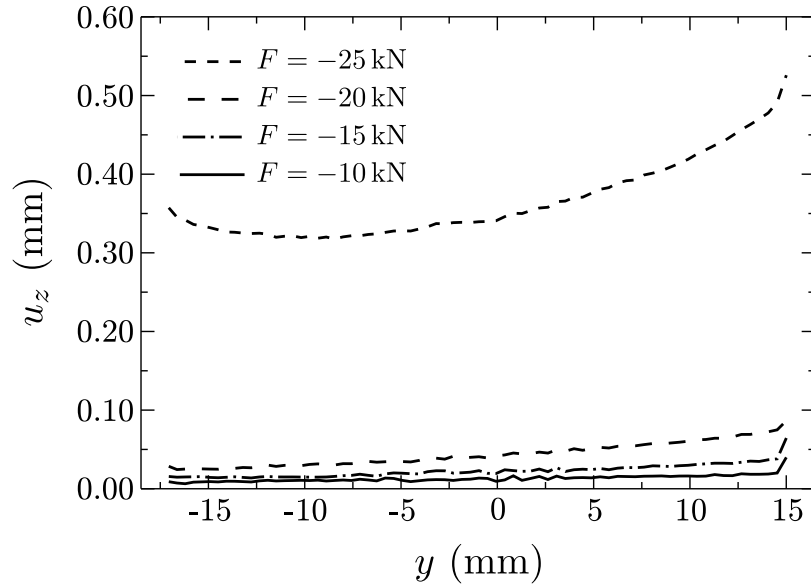


Figure 4.39: Test C-45, i.e. compression of a $[(+45/-45)_8]_S$ coupon. Out-of-plane displacement, u_z , along the section at $x = 0$ and $y = -w/2 \dots w/2$ for different specimen loads F .

Results. First of all the test C-45 is discussed in more detail since some features are most distinctive for this load case and, therefore, can be studied easily. Respective findings apply to the other tests as well.

The free length, l_f , is designed to avoid premature buckling. However, as the load is increased far beyond the elastic limit, the accumulated damage and the unrecoverable strains introduce imperfections, lead to lateral deflections in some cases, and affect the measured stress–strain response. This must be kept in mind when the experimental results are compared to the simulation results in which no lateral deflections are accounted for. In order to avoid misleading comparison, the measured stress–strain curves are cut off as soon as the measured out-of-plane displacements clearly exceed values which can be attributed to Poisson effects. The limit load, which is also predicted by the simulation, cannot be compared to the experimental results.

The magnitude of the measured lateral deflection is examined by curves as shown in Fig. 4.39. There the out-of-plane displacement, u_z , is plotted for the section at $x = 0$ and $y = -w/2 \dots w/2$ for loads of $F = -10, -15, -20$, and -25 kN. For loads smaller than $F = -20$ kN, the magnitude of the out-of-plane displacement is in a range which

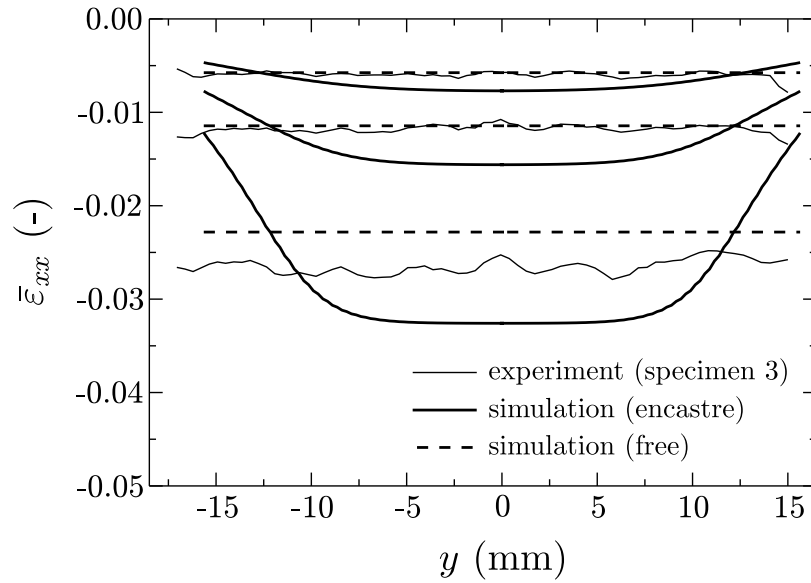


Figure 4.40: Test C-45. Laminate strain in loading direction, ε_{xx} , plotted for the section at $x = 0$ and $y = -w/2 \dots w/2$ for specimen loads of $F = -10$, -15 , and -20 kN; results from experiment and from simulation with free and encastre type boundary conditions.

is expected from Poisson effects. However, already for a load of $F = -25$ kN severe lateral deformation prevails in the experiment and the stress-strain curve measured at such high load levels is not used for comparison. A similar procedure is employed for all experimental results without further comments; respective plots of out-of-plane displacements are not shown for sake of brevity.

Another important feature to be investigated is the influence of the boundary conditions on the strain field. To demonstrate this influence (which is most pronounced for the test C-45), Fig. 4.40 shows the laminate strain ε_{xx} along the section at $x = 0$ and $y = -w/2 \dots w/2$ predicted by means of models with free and encastre type boundary conditions as well as measured in experiments. The distribution from the prediction using free boundary conditions is perfectly uniform (note that the latter predictions could, of course, also be obtained by simulations with a single FEM element). When encastre type boundary conditions are used, a considerable non-uniformity is predicted. The measured distribution of the laminate strain is again rather uniform. From this it can be concluded that the boundary conditions prevailing in the experimental testing are not comparable to a fixed support. This, in turn, is not surprising

as the tabs are relatively thick and as the bonding between the tabs and the coupon was recognized to be rather weak.

As the measured distribution of the laminate strain is rather uniform for all tested specimens, it is natural to introduce mean laminate strains, $\bar{\varepsilon}_{xx}$ and $\bar{\varepsilon}_{yy}$, which read

$$\bar{\varepsilon}_{xx} = \frac{1}{w} \int_{-w/2}^{w/2} \varepsilon_{xx}[x = 0, y] dy \quad \text{and} \quad \bar{\varepsilon}_{yy} = \frac{1}{w} \int_{-w/2}^{w/2} \varepsilon_{yy}[x = 0, y] dy . \quad (4.2)$$

The mean laminate stress shall be defined as the total applied force, F , divided by the nominal cross-section, i.e.

$$\bar{\sigma}_{xx} = \frac{F}{w t} . \quad (4.3)$$

Using the mean laminate stress and strain, classical stress–strain curves can be obtained which allow for convenient comparison of simulation and experimental results.

Finally, the laminate mean stress–strain curves of test C-45 can be compared. Such curves including un- and reloading loops are shown in Fig. 4.41, where experimental results from two different specimens and simulation results using encastre as well as free boundary conditions are plotted. Interestingly, the stress–strain curve from a simulation with encastre type boundary conditions implies a more compliant behavior compared to the stress–strain curve from a simulation with free type boundary conditions. However, when the respective force–displacement relation of the structure is investigated, the expected behavior is observed, i.e. the more constrained case is stiffer. The overall correlation between experimental and simulation results is good. Especially the ‘severity of the nonlinearity’ is predicted correctly.

Figures 4.42, 4.43, and 4.44 show the stress–strain curves which correspond to the remaining compression tests C-60, C-75, and C-90, respectively. The figures again show experimental results as well model predictions. Note that the larger the fiber angle (compared to the loading direction) is, the smaller gets the deformation transverse to the loading direction, and, consequently, the smaller is the difference between predictions obtained with the two types of boundary conditions. The response of C-90 is presented here even though respective test results are used to calibrate the constitutive model.

For all the tests the correlation between measurement and prediction is good and the response to the loading is predicted correctly. Nevertheless, especially for test

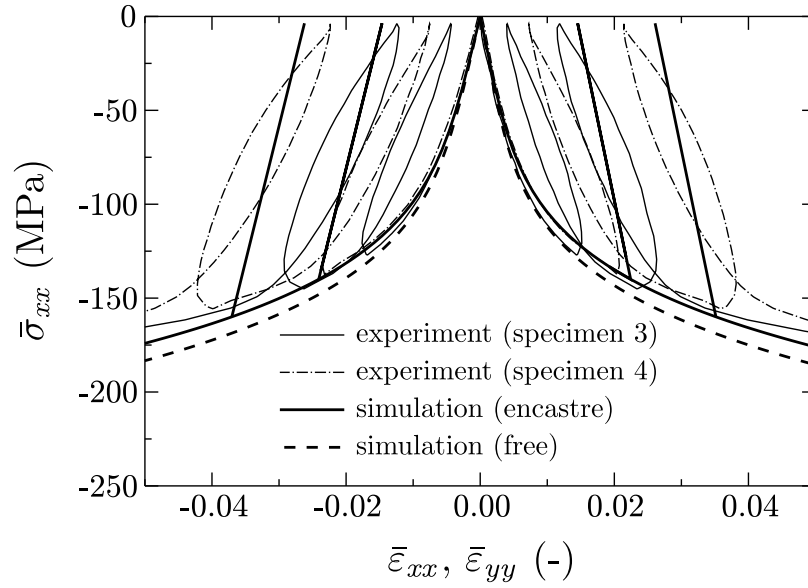


Figure 4.41: Test C-45, i.e. uniaxial compression of a $[(+45/-45)_8]_S$ coupon. Response of the coupon including un- and reloading loops in terms of mean laminate stress in loading direction, $\bar{\sigma}_{xx}$, versus mean laminate strain in loading direction, $\bar{\epsilon}_{xx}$, as well as versus mean laminate strain in transverse direction, $\bar{\epsilon}_{yy}$; predictions obtained with encastre and free type boundary conditions; experimental results for two specimens.

C-60 the unloading curves show that damage is under- and the residual strains are overestimated. This is not surprising as it was assumed in the formulation of the model that damage accumulation starts when the failure surface proposed by Puck is reached. Such high load levels are not reached within the compared parts of responses.

The mentioned model assumption has been introduced basically to keep the model easily applicable, even though González and LLorca (2007) showed that the behavior under dominant transverse compression can be affected by damage due to e.g. local failure of matrix/fiber interface. Earlier damage onset could be accounted for in the model rather easily by introducing a damage onset surface (which indeed was done in former versions of the model) but calibration of the model is then more complex.

As already mentioned, the predictions concerning limit loads are not assessed by the present study. Nevertheless, for the test C-45 a predicted contour plot is presented in Fig. 4.45 showing the strain localization. For the respective FEM analysis a model

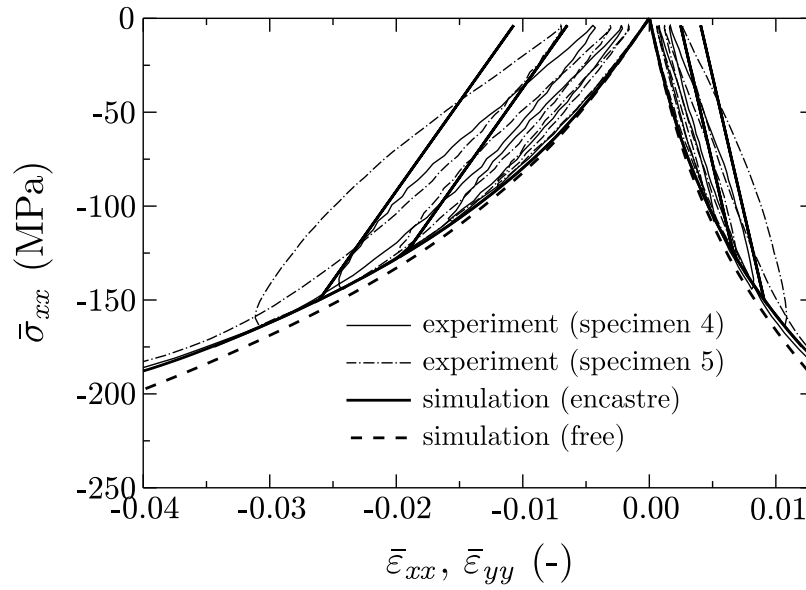


Figure 4.42: Test C-60, i.e. uniaxial compression of a $[(+60/-60)_8]_S$ coupon. Response of the coupon including un- and reloading loops in terms of mean laminate stress, $\bar{\sigma}_{xx}$, versus mean laminate strain in loading direction, $\bar{\varepsilon}_{xx}$, as well as versus mean laminate strain in transverse direction, $\bar{\varepsilon}_{yy}$; simulation results obtained with encastre and free type boundary conditions; experimental results for two specimens.

of the entire free region was used, but as no imperfections are introduced which would break the symmetry, an ‘undisturbed’ localization pattern is obtained. For all compression tests, i.e. C-45, C-60, C-75, and C-90, the predicted stress–strain curves are shown in Fig. 4.46. The limit load is indicated there by a ‘star’.

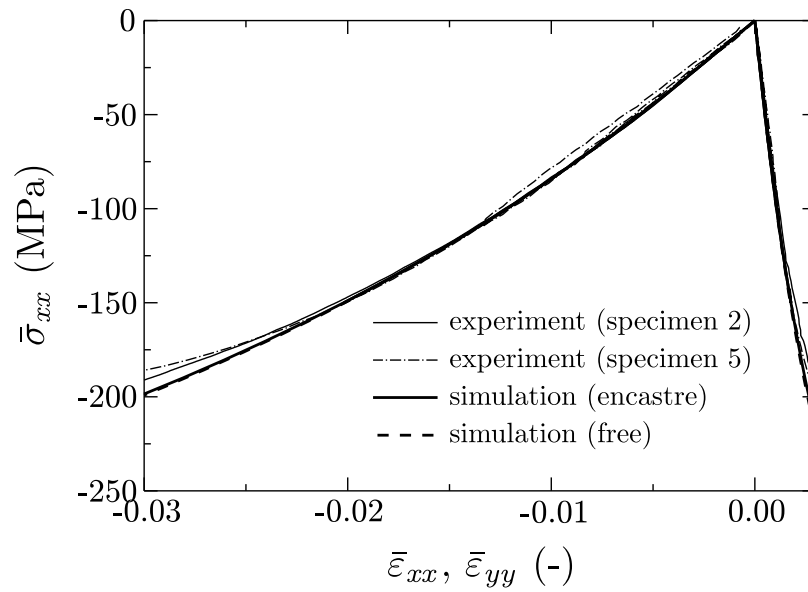


Figure 4.43: Test C-75, i.e. compression of a $[(+75/-75)_8]_S$ coupon. Response of the coupon in terms of mean laminate stress, $\bar{\sigma}_{xx}$, versus mean laminate strain in loading direction, $\bar{\epsilon}_{xx}$, as well as versus mean laminate strain in transverse direction, $\bar{\epsilon}_{yy}$; simulation results obtained with encastre and free type boundary conditions; experimental results for two specimens.

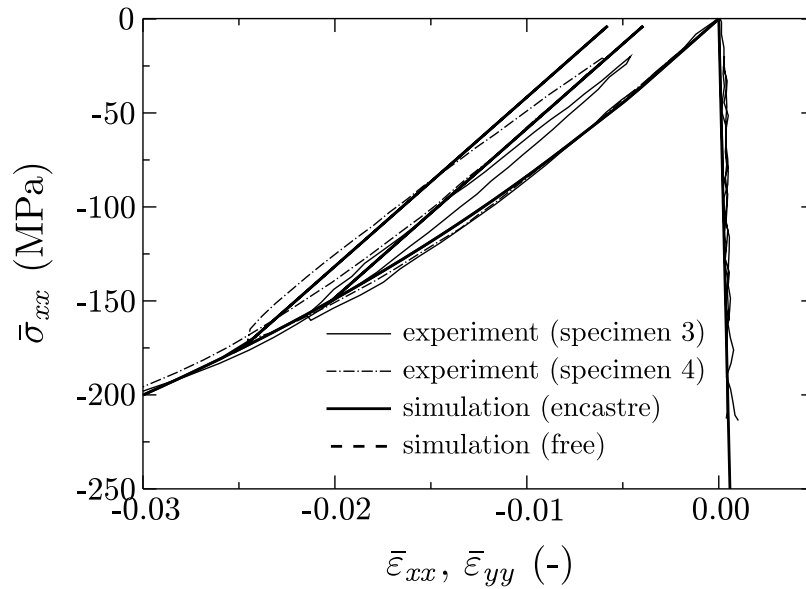


Figure 4.44: Test C-90, i.e. compression of a $[(90)_{16}]_S$ coupon. Response of the coupon including un- and reloading loops in terms of mean laminate stress, $\bar{\sigma}_{xx}$, versus mean laminate strain in loading direction, $\bar{\epsilon}_{xx}$, as well as versus mean laminate strain in transverse direction, $\bar{\epsilon}_{yy}$; simulation results obtained with encastre and free type boundary conditions; experimental results for two specimens.

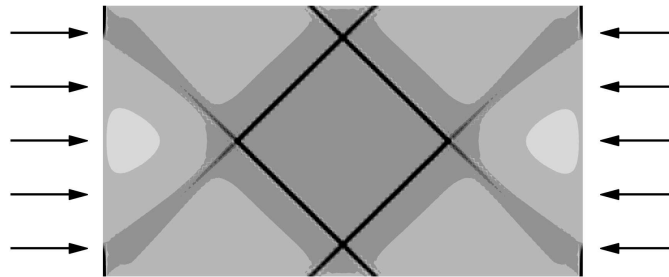


Figure 4.45: Test C-45, i.e. compression of a $[(+45/-45)_8]_S$ coupon. Distribution of the laminate strain in loading direction, ϵ_{xx} , predicted far beyond the peak load by means of an FEM model of the entire free region without imperfections and with encastre type boundary conditions.

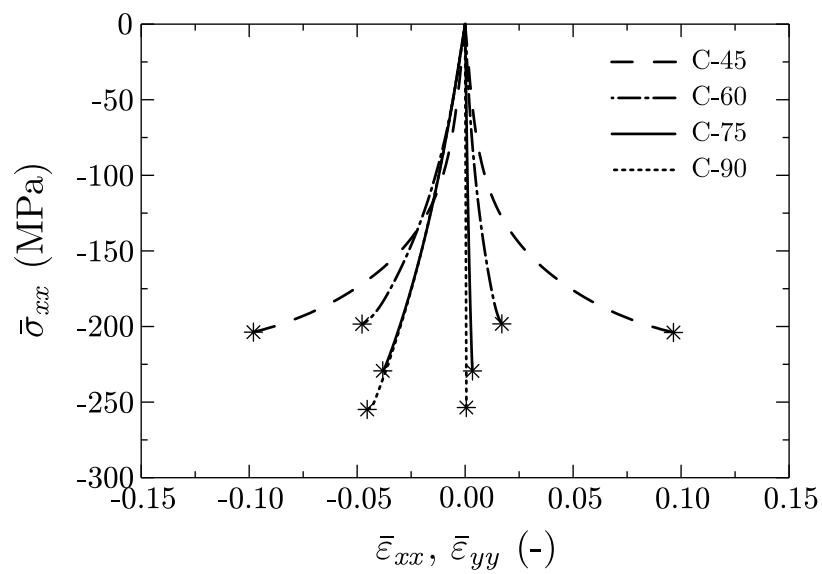


Figure 4.46: Tests C-45, C-60, C-75, and C-90. Predicted response including the limit load (star) in terms of mean laminate stress, $\bar{\sigma}_{xx}$, versus mean laminate strain in loading direction, $\bar{\epsilon}_{xx}$, as well as versus mean laminate strain in transverse direction, $\bar{\epsilon}_{yy}$.

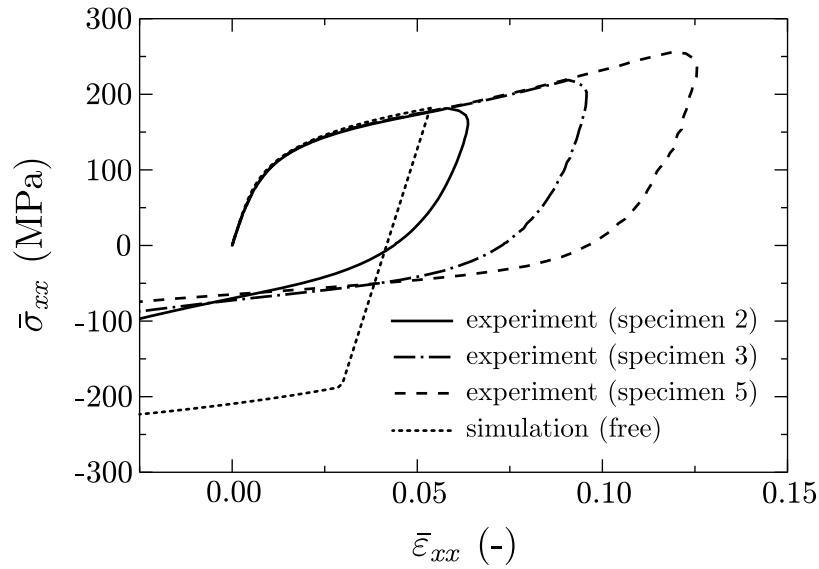


Figure 4.47: Test TC-45, a $[(+45/-45)_8]_S$ coupon subjected to uniaxial tension followed by uniaxial compression. Response of the coupon in terms of mean laminate stress, $\bar{\sigma}_{xx}$, versus mean laminate strain in loading direction, $\bar{\epsilon}_{xx}$; simulation results obtained with free type boundary conditions; experimental results for three specimens.

Finally, results from the tests are presented which aim at the effect of the loading history on the specimen response. These tests are TC-45, TC-60, and CT-75. Apart from test TC-45, the experimental results are given without comparison to predictions of the present model. Note that these tests focus on effects and phenomena which have been investigated in the literature very rarely.

Figure 4.47 shows the measured response for test TC-45, in which a $[(+45/-45)_8]_S$ coupon is subjected to uniaxial tension followed by uniaxial compression. The load is reversed at maximum tensile loads of $F = 20, 25,$ and 30 kN. Furthermore, the predicted response is shown for the case where the load is reversed at $F = 20$ kN. The measured response is astonishing. The stress-strain curve subsequent to the load reversal is approximately parallel to the curve of initial loading. Already in the region of the transition from tension to compression, the response becomes again very nonlinear. With respect to modeling of elasto-plasticity, this response suggests that the hardening behavior is not isotropic but is made up of isotropic and kinematic contributions. In the present model purely isotropic hardening was assumed. This

leads to the poor correlation between measured and predicted results observed in the compression regime.

In Fig. 4.48 a detail of the measured response for test TC-60 is shown, in which a $[(+60/-60)_8]_S$ coupon is subjected to uniaxial tension followed by uniaxial compression. The tensile load is reversed at $F = 14$ kN (specimen 3) and $F = 15$ kN (specimens 4 and 5), respectively. The response is compared to results from test C-60, where the same coupon is subjected to compression only. In Fig. 4.49 results from test CT-75 are shown, where a $[(+75/-75)_8]_S$ coupon is subjected to uniaxial compression followed by uniaxial tension. For both specimens shown in Fig. 4.49, the compressive load is reversed at $F = -20$ kN. The response is compared to results from test T-60, where the same coupon is subjected to tension only. When respective stress-strain curves are compared to each other, a small effect of damage, i.e. a slightly decreased stiffness, as well as some unrecoverable strains can be observed for the tests TC-60 and CT-75. However, the slope of the stress-strain curves do not change noticeably at transition from tension to compression and vice versa, i.e. neither the effect of stiffness recovery nor the effect of a sudden stiffness loss are pronounced enough to be observed by means of the present tests.

Discussion. In this section predictions obtained with the proposed constitutive model are compared experimental results obtained at the *PCCL*. This comparison shows that predictive capabilities of the present model are good. Especially the nonlinear response to loading is predicted correctly for various layups without any additional fitting. However, from unloading curves it can be seen that unrecoverable strains are somewhat overestimated, whereas the effect of damage is underestimated. Apart from the comparison, some experimental results are presented concerning phenomena treated very rarely in the literature.

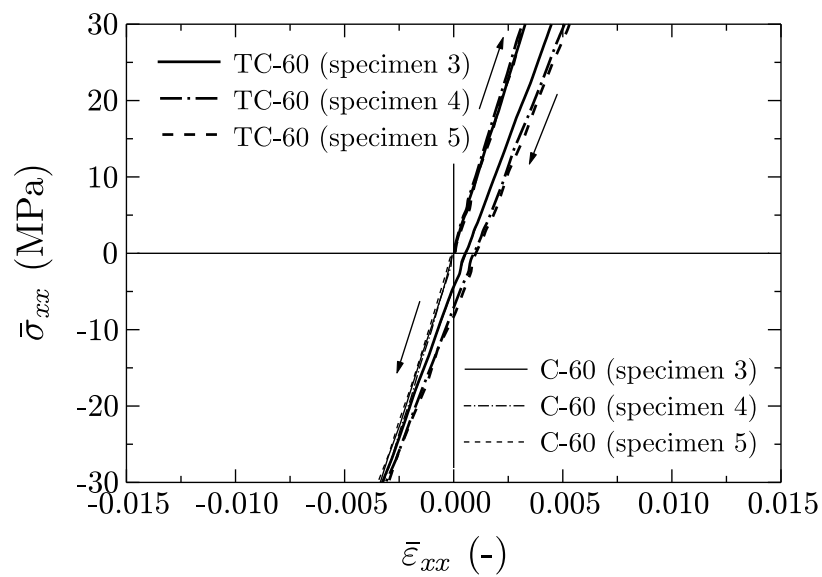


Figure 4.48: Test TC-60 versus C-60; a $[(+60/-60)_8]_S$ coupon is subjected to uniaxial tension followed by uniaxial compression (TC-60) or to uniaxial compression only (C-60); response of the coupon in terms of mean laminate stress, $\bar{\sigma}_{xx}$, versus mean laminate strain in loading direction, $\bar{\epsilon}_{xx}$;

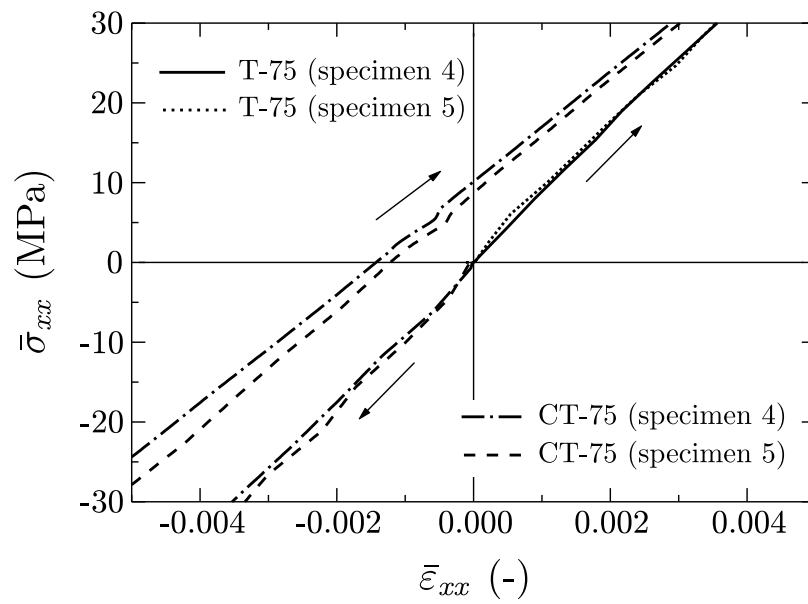


Figure 4.49: Test CT-75 versus T-75; a $[(+75/-75)_8]_S$ coupon is subjected to uniaxial compression followed by uniaxial tension (CT-75) or to uniaxial tension only (T-75); response of the coupon in terms of mean laminate stress, $\bar{\sigma}_{xx}$, versus mean laminate strain in loading direction, $\bar{\epsilon}_{xx}$;

4.6 Open hole tension tests

In the following section the response of open hole specimens subjected to uniaxial tension is investigated. The material system under consideration is IM7/8552 and different layups are studied, namely $[0^\circ/90^\circ]_s$, $[\pm 45^\circ]_s$, and $[+45^\circ/90^\circ/-45^\circ/0]_s$. Figure 4.50 shows the modeled specimen geometry and defines the laminate coordinate system. The absolute dimension is defined by the radius of the hole, R , which is chosen in accordance to the work by Jiang et al. (2007) to be $2R = 3.175$ mm, $2R = 6.350$ mm, and $2R = 12.700$ mm, respectively. The remaining dimensions, i.e. W and L , are determined by the ratios $L/R = 20$ and $W/R = 5$. The modeled ply and laminate thickness is of minor importance as it does not explicitly affect the strength predictions. In the present study only one eighth of the specimen is modeled (i.e. half of the width, half of the length, and half of the specimen thickness) and symmetry boundary conditions are applied. Finally, the FEM simulations are conducted using reduced integrated four- or eight-noded shell elements with layered section definitions. At critical regions the element size is chosen extremely small, i.e. in the vicinity of the hole around 0.03 mm. This is done because, on the one hand, high stress gradients need to be resolved. On the other hand, the specific fracture energies for localized matrix failure are very small, a fact that again requires fine FEM meshes at regions where softening takes place, cf. Eqn. (3.23). As usual, residual stresses from curing are taken into account by simulating a cooling-down from the given stress free temperature, T_{sf} , to a temperature of 20°C.

The FEM simulations presented in this section have been conducted in order to study the onset, the impact, and the interaction of the mechanisms incorporated within the present constitutive model. However, effects such as delamination and free edge effects are not accounted for in the present FEM simulations even though they are expected to have a significant impact on the structural response. Furthermore, geometrical symmetry conditions are used to reduce the FEM model size. Strictly speaking, this is inconsistent with both simulating strain localization as well as simulating layups that include e.g. $\pm 45^\circ$ -plies.

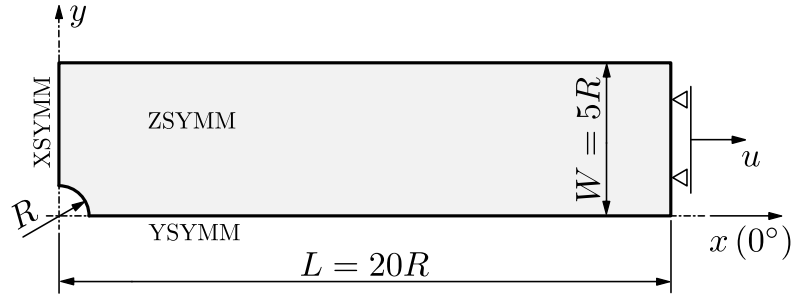


Figure 4.50: Dimensions of the open hole specimen, boundary conditions applied in the FEM model, and definition of the laminate coordinate system.

With respect to open hole tests, many research results were published in the last decades. For example in the paper by Lessard and Chang (1991) results from open hole compression tests are presented; the respective setup was analyzed numerically e.g. by Chang et al. (1991). Open hole tension tests were e.g. performed by Tan (1991), which in turn were treated numerically e.g. by Maimí et al. (2007b). A comprehensive investigation concerning open hole tension tests with focus on scaling effects was done by Green et al. (2007) and Hallett et al. (2009). Within the same work group, a cohesive zone model has been proposed by Jiang et al. (2007). This model was used to implement an interface element for the explicit FEM package *LS-DYNA*. The interface elements, in turn, were used within FEM models of open hole specimens. In FEM simulations based on such a cohesive zone approach, the proper placement of the interface elements is crucial; however, the proposed numerical setup is able to reproduce various experimental observations.

Calibration. Even though qualitative predictions are of interest, the constitutive model is calibrated with respect to the considered material system IM7/8552. Since IM7/8552 is also used within the WWFEs, the material data as provided by the WWFE can be used for this purpose. Accordingly, the same calibration scheme as applied in Sect. 4.3 is conducted and the respective material data can be found in the in Tabs. C.1, C.2, C.3, C.4, and C.5. However, since strain softening is simulated here, some modifications are recommended which have been already discussed in Sect. 3.5. Most important, the stiffness recovery parameter is set to $\mu_d = 0$, cf. Eqn. (3.8), in order to allow for a completely damaged material. Furthermore, $s = 1$ and $m = 1$

is set for Puck's weakening parameters. The interaction parameter μ_{II} of the plasticity model is chosen smaller compared to the result of calibration scheme described in Sect. 4.3, i.e. $\mu_{II} = 0.8$. This is done as the requirements of Eqn. (3.30) have to be fulfilled also for slightly increased peak stresses caused by viscous regularization. With respect to the localized damage model, the amount of matrix damage that triggers localization is taken to be $\xi_c^{(m)} = 0.015$. The specific fracture energies $G^{(mt)} = 0.2 \text{ N/mm}$ and $G^{(ps)} = 1.0 \text{ N/mm}$ are extracted from the paper by Jiang et al. (2007)¹. The remaining specific fracture energies are taken as $G^{(ft)} = 89.8 \text{ N/mm}$, $G^{(fc)} = 78.3 \text{ N/mm}$, and $G^{(mc)} = 0.8 \text{ N/mm}$. This is in accordance to the paper by Maimí et al. (2007b) where the material system T300/1034-C is considered. All the specific fracture energies are summarized in Table C.7. With respect to viscous regularization, the parameters are chosen small compared to the simulation (pseudo) time of 1 s, namely $\eta^{(ft)} = \eta^{(fc)} = 2 \cdot 10^{-3} \text{ s}$ and $\eta^{(mt)} = \eta^{(mc)} = 4 \cdot 10^{-3} \text{ s}$.

Results for Layup $[0^\circ/90^\circ]_S$. For this layup the area where initial matrix damage occurs is limited to very small regions at the vicinity of the hole. As a consequence, the structural response is linear almost until the limit load is reached. However, matrix damage starts to localize at the hole and then propagates in parallel to the loading direction towards the region of load introduction. Figure 4.51 shows the localization zone in terms of matrix damage which has accumulated in a 0° -ply at a relatively high load level. To provide a good impression of the localization zone, one half of the plate is shown even though only one quarter was modeled. This is done also in the following figures. Furthermore, the contour plots presented in this section are obtained from simulations in which hole diameters of $2R = 3.175 \text{ mm}$ are modeled.

The predicted damage behavior might be interpreted as 'longitudinal splitting' which is also observed in experimental testing. To demonstrate this, Fig. 4.52 shows matrix damage observed in a notched $[0^\circ/90^\circ]_S$ specimen caused by cyclic (uniaxial) loading. The picture is taken from the paper by Yang and Cox (2005).

¹Even though Jiang et al. consider IM7/8552 as well, they give different material parameters as done within the WWFE, namely $E_1^{(0)} = 161000 \text{ MPa}$, $E_2^{(0)} = 11380 \text{ MPa}$, $\nu_{12}^{(0)} = 0.32$, $G_{12}^{(0)} = 5170 \text{ MPa}$, $G_{23}^{(0)} = 3980 \text{ MPa}$, $Y^{(t)} = 60 \text{ MPa}$, and $S = 90 \text{ MPa}$.

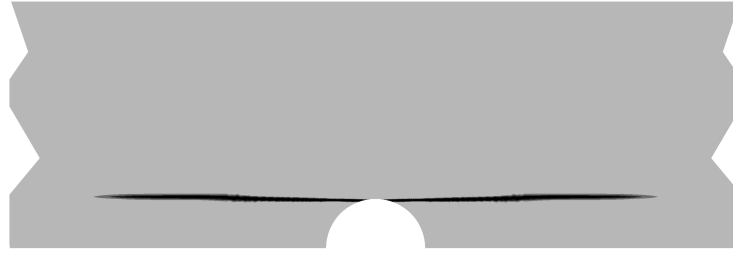


Figure 4.51: Localization zone in terms of accumulated matrix damage (ξ_2) predicted for a 0° -ply of the $[0^\circ/90^\circ]_S$ open hole specimen under tension.

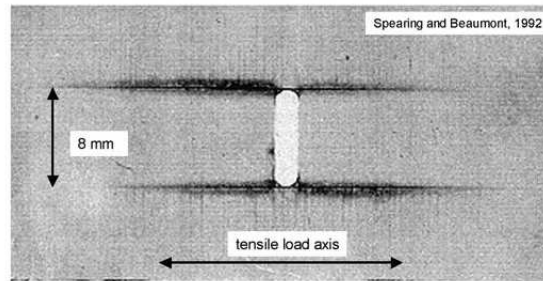


Figure 4.52: Matrix cracks observed in an notched $[0^\circ/90^\circ]_S$ specimen subjected to cyclic loading; figure taken from the paper by Yang and Cox (2005), originally published by Spearing and Beaumont (1992).

In general, openings such as the hole in the considered specimen are well known to cause stress concentrations. The impact of the matrix damage zone on the stress concentration is studied next. To this end, Fig. 4.53 shows the factor of fiber exertion, $f_E^{(f)}$, predicted in a 0° -ply of the $[0^\circ/90^\circ]_S$ laminate along the section at $x = 0$ and $y = R \dots 5R$. The individual curves correspond to different load levels, i.e. to different damage states. It can be seen that the matrix damage zone strongly reduces stress concentration; finally the cross section is much more uniformly loaded. This, in turn, shifts onset of fiber failure to higher specimen loads. Note that the curves of Fig. 4.53 are not smooth at $y/R = 1$ as some artificial progressive fiber failure is predicted already at rather low load levels.

Results for $[\pm 45^\circ]_S$. Here no fibers are oriented in loading direction. This makes the specimen compliant and the predicted structural response is strongly nonlinear.

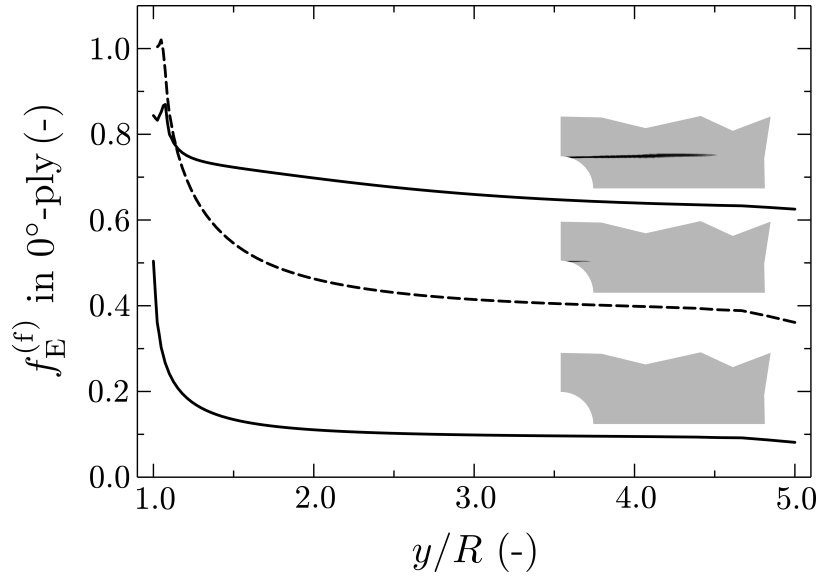


Figure 4.53: Factor of fiber exertion, $f_E^{(f)}$, at $x = 0$ and $y = R \dots 5R$ predicted in a 0° -ply of the $[0^\circ/90^\circ]_S$ laminate.

Such behavior is also observed in experiments e.g. conducted by Lessard and Chang (1991). In the model the pronounced non-linearity is mainly caused by the accumulation of plastic shear strains along an x-shaped area. Considering a low load level, the distribution of the plastic shear strains is shown in Fig. 4.54. As the load is increased, matrix damage accumulates and finally starts to localize. Figure 4.55 shows the respective localization zone in terms of matrix damage predicted for the moment where the load reaches its peak value. The same localization pattern is obtained also when a perfect model of the entire specimen geometry is used. Remember that no imperfection is used in the present FEM model to trigger the damage localization.

Figure 4.56 shows the FEM model proposed by Jiang et al. (2007) with its embedded interface elements. When the placement of the interface elements (which was inspired by experimental results) is compared to the zones of localized matrix damage observed before, convincing similarities become obvious.

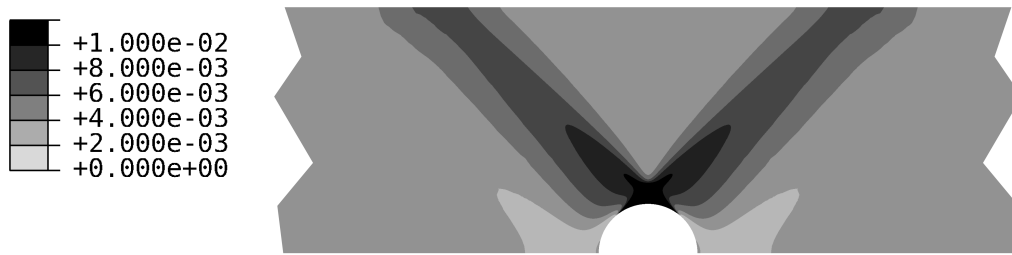


Figure 4.54: Accumulated plastic shear strains, $\gamma_{12}^{(pl)}$, predicted for a $+45^\circ$ -ply of the $[\pm 45^\circ]_S$ open hole specimen under tension.

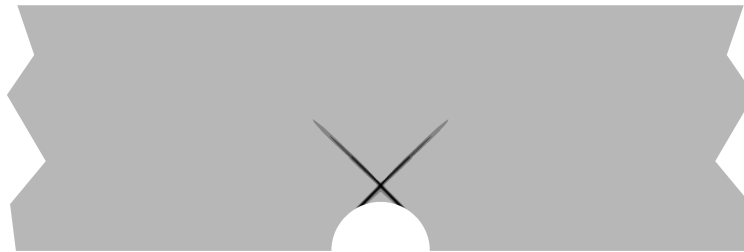


Figure 4.55: Localization zone in terms of accumulated matrix damage, ξ_2 , predicted for a $+45^\circ$ -ply of the $[\pm 45^\circ]_S$ open hole specimen under tension.

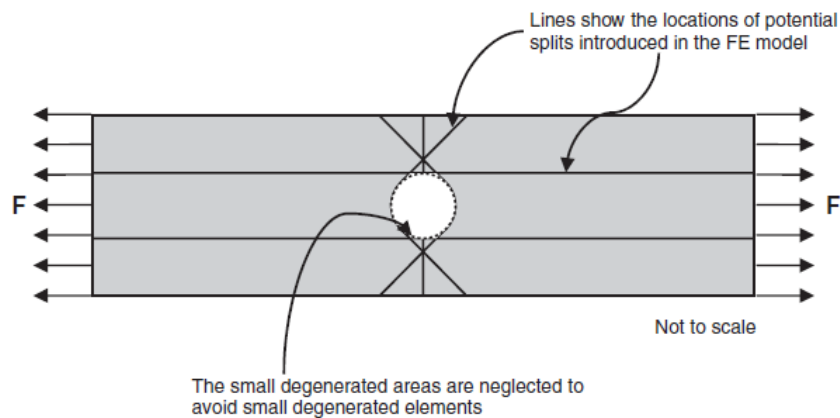


Figure 4.56: Sketch of the FEM model proposed by Jiang et al. (2007); black lines show the embedded interface elements; the picture is taken from the paper by Jiang et al. (2007).

Results for $[+45^\circ/90^\circ/-45^\circ/0]_S$. The predicted behavior is totally different for quasi-isotropic laminates compared to the layups treated so far. During loading of such specimen, various modeled mechanisms become active within the plies. The structural response is, nevertheless, linear almost until the limit load is reached. In Fig. 4.57 a contour plot is given exemplarily concerning the matrix damage which has accumulated when the load reaches its peak. Note that the maximum value of all ply level predictions is plotted there. The peak load is determined by localized failure; the respective localization zone initiates at the hole. The narrow localization zone is also plotted in Fig. 4.57. Note that its color (light gray) is not consistent with the legend.

The contour plot given in Fig. 4.57 is obtained for a model with a hole diameter of $2R = 3.175$ mm. However, for the other absolute dimensions similar failure behavior is observed. With this respect a systematical study has been performed in which each geometry was discretized by various FEM meshes. The observed failure behavior is shown to be independent from the actual FEM discretization.

In experimental testing the specimen size has an impact on the observed failure behavior. Possible failure modes of $[+45^\circ/90^\circ/-45^\circ/0]_S$ specimens observed in experimental tests are shown in Fig. 4.58. For the specimens depicted there the ratios $L/R = 20$ and $W/R = 5$ hold but the absolute dimension as well as the stacking of the plies have been varied. The pictures shown in Fig. 4.58 are taken from the paper by Hallett et al. (2009).

Discussion. In the present section the response of open hole specimens subjected to uniaxial tension is investigated. As the layup is varied, very different failure behavior is observed in the simulations. The overall response can thereby range from very compliant to linear elastic almost up to the peak load. Qualitative comparison of the results suggests that important intra-ply mechanisms are captured well by the proposed constitutive model. However, it shall be repeated that delamination is not accounted for in the present modeling approach.

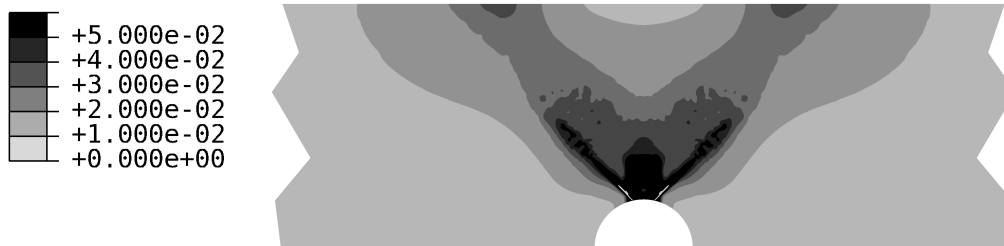


Figure 4.57: Accumulated matrix damage, ξ_2 , predicted at the peak load for $[+45^\circ/90^\circ/-45^\circ/0]_S$ open hole specimen with hole diameter of $2R = 3.175$ mm; maximum value of all ply level predictions as well as localization zone (light gray).

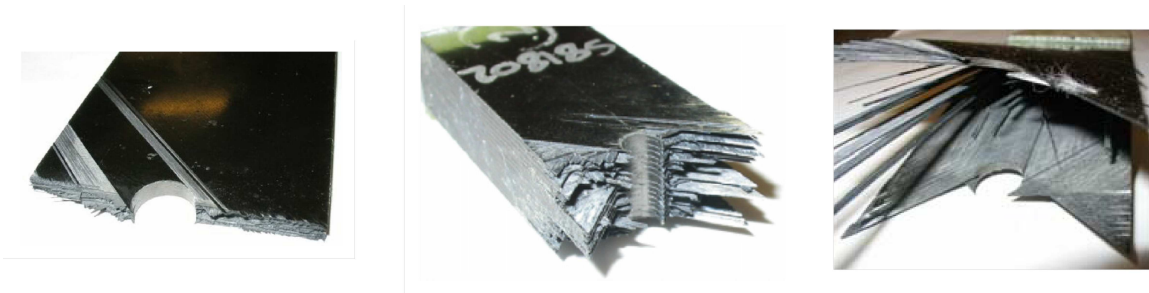


Figure 4.58: Failure modes observed in experimental tests with various $[+45^\circ/90^\circ/-45^\circ/0]_S$ open hole specimen; pictures taken from the paper by Hallett et al. (2009).

Chapter 5

Summary

In order to predict the response of laminated composites made of unidirectional fiber reinforced polymers, it is commonly accepted to combine a kinematic laminate model with a constitutive model for the homogenized ply material. In the formulation of such a constitutive model the nonlinear ply behavior should be accounted for in order to achieve reliable predictions also beyond the elastic limit. The formulation of such a ‘nonlinear’ constitutive model was the main objective of the present work.

Motivated by experimental observations, the constitutive model distinguishes two major types of phenomena which both lead to pronounced nonlinear ply behavior. These phenomena are ‘stiffness degradation’ and ‘unrecoverable strain accumulation’.

Stiffness degradation is attributed to microscopic brittle matrix cracking, fiber/matrix debonding, as well as progressive fiber failure and is modeled via continuum damage mechanics. With respect to damage evolution two different approaches are utilized, whereby the actual material state determines the active one. The first approach deals with stiffness degradation due to evenly distributed, matrix dominated phenomena. The respective damage evolution equation is related to the material exertion predicted with recourse to Puck’s failure surface. The second approach for damage evolution deals with stiffness degradation that shows strain softening and is formulated with respect to elastic strains. Here matrix dominated as well as fiber dominated phenomena are accounted for. In order to estimate the anisotropic effect of brittle damage, the ply material behavior is featured by the behavior of a fictitious material which consists of inhomogeneities embedded into the undamaged ply material. The fic-

titious material is used to estimate the anisotropic characteristics of damage via a micromechanical method.

Unrecoverable strain accumulation is associated to the formation of microscopic areas with inelastic deformed matrix material. Based on phenomenological assumptions, the unrecoverable strain accumulation is modeled by two plasticity mechanisms. They treat the evolution of plastic in-plane shear strains and the evolution of plastic normal strains of the ply. By the presented approach the ductile portion of the behavior of fiber reinforced polymer plies as observed in experimental testing is captured. This is of major importance for accurate predictions beyond the non-linearities due to monotonic loading.

In order to use the constitutive model for quantitative predictions, the model has to be calibrated with respect to the considered material system. The respective procedure for easy calibration of the model parameters has been discussed in the present work. The limitations of the proposed constitutive model have been addressed in detail as well.

The development of the constitutive model aims at the analysis of laminated, thin-walled structures as for example used in many applications of aeronautics. Since finite element methods are state-of-the-art tools for structural analyses, the constitutive model has been implemented as a user defined material within the commercial FEM package *Abaqus*. The numerical procedure including the derivation of the material Jacobian matrix has been discussed.

The capabilities of the proposed constitutive model are assessed by comparing its predictions to experimental data. For this purpose laminates subjected to homogeneous loading conditions, coupon tests, and other components are considered. Most of the predicted responses show good agreement with the experimental results. This holds true for different loading scenarios which in turn lead to very different ply loading conditions. Finally it can be stated that the responses of the considered laminates, which are highly nonlinear in some cases, are predicted well by the present constitutive model. This increases the confidence in the model predictions what is very advantageous since improved prediction reliability is a major prerequisite exploitation of the weight saving potential of modern material systems.

The proposed constitutive model offers some outstanding features concerning the simulation of laminated composites. Firstly, residual deformations are predicted which is very unlike to many other available models. Secondly, the laminate stiffness affected by anisotropic brittle damage is captured. Finally, the behavior of components in the proximity of the load carrying capacity can be simulated since strain softening is modeled as well. All the mentioned phenomena are incorporated within a single constitutive model, which is easy to calibrate and readily implemented within FEM. The constitutive model can, therefore, be used in FEM analyses of entire structures.

Due to the complexity of the material model, quite a number of model parameters have been introduced. However, the sensitivity of the model to changing some of them is low, i.e. the characteristics of the predicted response is determined by the modeled mechanisms and not by the actual values of the model parameters. This behavior is very advantageous and, accordingly, the model is well suited for practical applications in engineering purposes. Even if not all model parameters can be calibrated from experimental results, predictions with sufficient accuracy can be expected.

Nevertheless, further work needs to be done. First of all the constitutive model should be combined with a method for the simulation of the emergence and growth of delaminations. Furthermore, the plane stress assumption should be abandoned so that also thick-walled laminates, as typically used at regions of load introductions, can be analyzed. Additional testing of the constitutive model would be desired to further increase the confidence in the model predictions.

Appendix A

Notations

In this section the notations are discussed which are used in the present work. To this end, the tensorial notation (\mathbf{a}_{ij} , \mathbf{A}_{ijkl}) is used as reference notation.

The engineering notation (\mathbf{a} , \mathbf{A}) is used in the present work to represent tensorial equations based on tensors of rank two and four by equations based on vectors and matrices, respectively. In order to assure correct results compared to the tensorial equations, the operations acting on the matrices and vectors are modified with respect to classical matrix operations. How the representations look like is discussed very briefly below; how the matrix operations are modified is extensively documented in the thesis by Nogales (2008). The vector/matrix notation ($\underline{\mathbf{a}}$, $\underline{\underline{\mathbf{A}}}$) is used for various equations where matrices and vectors are involved. Here the operations acting on the matrices and vectors are classical operations, but this leads to a limited applicability, i.e. some tensorial equations cannot be expressed in this notation. All the used notations are summarized in the listing below.

Tensorial notation (used as reference in this section only):

\mathbf{a}_{ij} , α_{ij} ... tensors of rank two
 \mathbf{A}_{ijkl} , \mathbf{B}_{ijkl} ... tensors of rank four

Engineering notation (quasi-vector and quasi-matrix notation):

\mathbf{a} , $\boldsymbol{\alpha}$... vector representations of symmetric tensors of rank two
 \mathbf{A} , \mathbf{B} ... matrix representations of tensors of rank four with minor symmetry

Vector/matrix notation:

$$\begin{aligned} \underline{\mathbf{a}}, \underline{\boldsymbol{\alpha}} & \quad \dots \text{ vectors} \\ \underline{\underline{\mathbf{A}}}, \underline{\underline{\mathbf{B}}} & \quad \dots \text{ matrices} \end{aligned}$$

In the present work tensors are represented by vectors and matrices. How these representations are introduced is related to the double contraction of a fourth-rank tensor and a second-rank tensor, which shall be given by

$$\mathbf{a}_{ij} = \mathbf{A}_{ijkl} \mathbf{b}_{lk} . \quad (\text{A.1})$$

To represent this simple equation by matrices and vectors only, the ‘strain-like’ vector representation of the symmetric second-rank tensor \mathbf{b}_{ij} ,

$$\mathbf{b} = \begin{pmatrix} b_{11} \\ b_{22} \\ b_{33} \\ 2 b_{12} \\ 2 b_{13} \\ 2 b_{23} \end{pmatrix} = \begin{pmatrix} b_1 \\ b_2 \\ b_3 \\ b_4 \\ b_5 \\ b_6 \end{pmatrix} = \underline{\underline{\mathbf{b}}} . \quad (\text{A.2})$$

and the ‘stress-like’ vector representation of the symmetric second-rank tensor \mathbf{a}_{ij} ,

$$\mathbf{a} = \begin{pmatrix} a_{11} \\ a_{22} \\ a_{33} \\ a_{12} \\ a_{13} \\ a_{23} \end{pmatrix} = \begin{pmatrix} a_1 \\ a_2 \\ a_3 \\ a_4 \\ a_5 \\ a_6 \end{pmatrix} = \underline{\underline{\mathbf{a}}} , \quad (\text{A.3})$$

are introduced. Note that in the present work such vector representations are typically used for stress and strain tensors. If so, they are also referred to as vectors of stress and strain components, respectively.

Due to the introduced vector representations, it is straightforward to introduce a matrix representation of the fourth rank tensor \mathbf{A}_{ijkl} such that, finally, the double contraction can be written as

$$\mathbf{a} = \mathbf{A} \mathbf{b} \quad \text{and} \quad \underline{\underline{\mathbf{a}}} = \underline{\underline{\mathbf{A}}} \underline{\underline{\mathbf{b}}} , \quad (\text{A.4})$$

respectively. Here \mathbf{A} and $\underline{\underline{\mathbf{A}}}$ stand for the same matrix and the operation between \mathbf{A} and \mathbf{b} and between $\underline{\underline{\mathbf{A}}}$ and $\underline{\underline{\mathbf{b}}}$ is the classical matrix operation. Accordingly, both notations are equivalent in this example.

To demonstrate the difference between the engineering notation and the vector/matrix notation, it is assumed that the inverted relation of the above double contraction can be written as

$$\mathbf{b}_{ij} = \mathbf{B}_{ijkl} \mathbf{a}_{lk} . \quad (\text{A.5})$$

As long as the same scheme is used to obtain the matrices \mathbf{B} and $\underline{\underline{\mathbf{B}}}$ from the tensor \mathbf{B}_{ijkl} , and as long as same stress- and strain-like vector representations are used, it holds

$$\mathbf{b} = \mathbf{B} \mathbf{a} \quad \text{and} \quad \underline{\underline{\mathbf{b}}} \neq \underline{\underline{\mathbf{B}}} \underline{\underline{\mathbf{a}}} . \quad (\text{A.6})$$

Here the product between \mathbf{B} and \mathbf{a} is not a classical matrix operation.

Note that various vector representations have been proposed in the literature; the presented one has some advantages concerning the computation of energy densities. For further information see for example the paper by Nadeau and Ferrari (1998).

Plane stress states

For plane stress states, $\sigma_{i3} = 0$ holds for $i = 1, 2, 3$. Such stress states are represented by vectors containing only $N = 3$ stress components and read

$$\underline{\underline{\boldsymbol{\sigma}}} = \begin{pmatrix} \sigma_{11} \\ \sigma_{22} \\ \sigma_{12} \end{pmatrix} = \begin{pmatrix} \sigma_1 \\ \sigma_2 \\ \sigma_3 \end{pmatrix} . \quad (\text{A.7})$$

Even though $\varepsilon_{i3} \neq 0$ for $i = 1, 2, 3$, the respective vector of strain components reads

$$\underline{\underline{\boldsymbol{\varepsilon}}} = \begin{pmatrix} \varepsilon_{11} \\ \varepsilon_{22} \\ 2\varepsilon_{12} \end{pmatrix} = \begin{pmatrix} \varepsilon_{11} \\ \varepsilon_{22} \\ \gamma_{12} \end{pmatrix} = \begin{pmatrix} \varepsilon_1 \\ \varepsilon_2 \\ \varepsilon_3 \end{pmatrix} . \quad (\text{A.8})$$

Here the engineering shear strain (shear angle) has been used, which shall be defined as $\gamma_{ij} = 2\varepsilon_{ij}$ for $i, j = 1, 2, 3$ with $i \neq j$.

Appendix B

Puck's failure criterion

In the following the equations of Puck's failure criterion for plane stress states are summarized. Thereby, parametric coupling and weakening due to longitudinal stresses as proposed by Schürmann (2005) and Puck and Mannigel (2007), respectively, is used.

Puck's failure surface is defined in terms of five nominal strength values, $X^{(t)}$, $X^{(c)}$, $Y^{(t)}$, $Y^{(c)}$, and S , two slope parameters, $p^{(t)}$ and $p^{(c)}$, and two weakening parameters, s and m . Here X is the nominal strength in fiber direction, Y is the nominal strength in (in-plane) transverse direction, and S is the nominal (in-plane) shear strength. Furthermore, the superscripts (t) and (c) refer to tensile and compressive loading conditions, respectively. The slope parameters, s and m , are termed $p_{\perp||}^+$ and $p_{\perp||}^-$ in Puck's notation.

Transition point. The transition between non-inclined fracture planes and inclined fracture planes takes place at stress ratios of $\sigma_{22}/|\sigma_{12}| = -\sigma_{22}^</math>/\sigma_{12}^</math>. Here the components $-\sigma_{22}^</math> and $\pm\sigma_{12}^</math> refer to points on the failure surface at $\sigma_{11} = 0$; they are defined by$$$

$$\sigma_{22}^</math> = \frac{S}{2p^{(c)}} \left(\sqrt{1 + 2p^{(c)} \frac{Y^{(c)}}{S}} - 1 \right), \quad (\text{B.1})$$

$$\sigma_{12}^</math> = S \sqrt{1 + 2p^{(c)} \frac{\sigma_{22}^</math>}{S}}. \quad (\text{B.2})$$

Compared to Puck's notation, $R_{23}^A = \sigma_{22}^</math> and $\tau_c = \sigma_{12}^</math> hold.$$

Fracture plane angle. If $\sigma_{22} < 0$ and $0 \leq \left| \frac{\sigma_{12}}{\sigma_{22}} \right| \leq \left| \frac{\sigma_{12}^{\prime}}{\sigma_{22}^{\prime}} \right|$ hold, the fracture plane angle, φ , is defined by

$$\cos \varphi = \sqrt{\frac{\sigma_{22}^{\prime}}{|\sigma_{22}^*|}}, \quad (\text{B.3})$$

where σ_{22}^* is the transverse stress at failure. The maximum fracture plane angle, ϕ , reached under uniaxial transverse compression is defined by

$$\cos \phi = \sqrt{\frac{\sigma_{22}^{\prime}}{Y^{(c)}}}. \quad (\text{B.4})$$

Failure Surface. The failure surface can be written as

$$F_P = F_P[\sigma_{11}, \sigma_{22}, \sigma_{12}] = F_P^{(m)}[\sigma_{22}, \sigma_{12}] - F_P^{(f)}[\sigma_{11}] = 0. \quad (\text{B.5})$$

The functions $F_P^{(m)}$ and $F_P^{(f)}$ are defined in a piecewise manner and read as follows.

If $\sigma_{22} \geq 0$ then $\varphi = 0$ and

$$F_P^{(m)} = \sqrt{\left(1 - p^{(t)} \frac{Y^{(t)}}{S}\right)^2 \left(\frac{\sigma_{22}}{Y^{(t)}}\right)^2 + \left(\frac{\sigma_{12}}{S}\right)^2} + p^{(t)} \frac{\sigma_{22}}{S}; \quad (\text{B.6})$$

if $\sigma_{22} < 0$ and $0 \leq \left| \frac{\sigma_{22}}{\sigma_{12}} \right| \leq \left| \frac{\sigma_{22}^{\prime}}{\sigma_{12}^{\prime}} \right|$ then $\varphi = 0$ and

$$F_P^{(m)} = \sqrt{\left(p^{(c)} \frac{\sigma_{22}}{S}\right)^2 + \left(\frac{\sigma_{12}}{S}\right)^2} + p^{(c)} \frac{\sigma_{22}}{S}; \quad (\text{B.7})$$

if $\sigma_{22} < 0$ and $0 \leq \left| \frac{\sigma_{12}}{\sigma_{22}} \right| \leq \left| \frac{\sigma_{12}^{\prime}}{\sigma_{22}^{\prime}} \right|$ then $\varphi \geq 0$ and

$$F_P^{(m)} = \left(\left(\frac{\sigma_{12}}{2(S + p^{(c)} \sigma_{22})} \right)^2 + \left(\frac{\sigma_{22}}{Y^{(c)}} \right)^2 \right) \frac{Y^{(c)}}{-\sigma_{22}}. \quad (\text{B.8})$$

If $-s X^{(c)} \leq \sigma_{11} \leq s X^{(t)}$ then

$$F_P^{(f)} = 1; \quad (\text{B.9})$$

if $s X^{(t)} < \sigma_{11} < X^{(t)}$ then

$$F_P^{(f)} = \sqrt{1 - \frac{1 - m^2}{(1 - s)^2} \left(\frac{\sigma_{11}}{X^{(t)}} - s \right)}; \quad (\text{B.10})$$

if $-X^{(c)} < \sigma_{11} < -s X^{(c)}$ then

$$F_P^{(f)} = \sqrt{1 - \frac{1 - m^2}{(1 - s)^2} \left(\frac{\sigma_{11}}{-X^{(c)}} - s \right)}. \quad (\text{B.11})$$

Appendix C

Material parameters

Table C.1: Engineering elastic constants of the undamaged ply material for the material systems considered in the present work; values indicated by the superscript † are estimated by the author.

	AS4/PEEK	AS4/3501-6	glass/epoxy	G4-800/5260	IM7/8552	Cycom977
$E_1^{(0)}$ (MPa)	128000	126000	45600	173000	165000	146000
$E_2^{(0)}$ (MPa)	11000	11000	16200	10000	9000	9000
$\nu_{12}^{(0)}$ (-)	0.300	0.280	0.278	0.330	0.340	0.340 [†]
$G_{12}^{(0)}$ (MPa)	4650	6600	5830	6940	5600	4270 [†]

Table C.2: Parameters defining the thermal behavior of some material systems considered in the present work.

	AS4/3501-6	glass/epoxy	G4-800/5260	IM7/8552
T_{sf} ($^{\circ}\text{C}$)	177	120	95	177
α_{11} ($10^{-6}/\text{K}$)	-1.0	8.6	-0.6	-1.0
α_{22} ($10^{-6}/\text{K}$)	26.0	26.4	36.0	18.0

Table C.3: Nominal ply strength values of the material systems considered in the present work; values indicated by the superscript \dagger are estimated by the author.

	AS4/PEEK	AS4/3501-6	glass/epoxy	G4-800/5260	IM7/8552	Cycom977
$X^{(t)}$ (MPa)		1950	1280	2750	2560	2100
$X^{(c)}$ (MPa)		1480	800	1700	1590	1407
$Y^{(t)}$ (MPa)		48	40	75	73	82
$Y^{(c)}$ (MPa)	243 †	200	145	210	185	249
S (MPa)	80 †	79	73	90	90	110 †

Table C.4: Slope and weakening parameters needed for the definition of Puck’s failure surface; slope parameters as suggested by Puck et al. (2002), but the value indicated by the superscript † is estimated by the author; weakening parameters as suggested by Schürmann (2005); the values in brackets are used when also the model for localized damage is applied.

	AS4/PEEK	AS4/3501-6	glass/epoxy	G4-800/5260	IM7/8552	Cycom977
$p^{(t)}$ (-)		0.35	0.30	0.35	0.35	0.35
$p^{(c)}$ (-)	0.15 [†]	0.30	0.25	0.30	0.30	0.30
s (-)		0.5	0.5	0.5	0.5 (1.0)	0.5 (1.0)
m (-)		0.5	0.5	0.5	0.5 (1.0)	0.5 (1.0)

Table C.5: Parameters of the power laws as calibrated for the present constitutive model, cf. Sect. 3.5.

	AS4/PEEK	AS4/3501-6	glass/epoxy	G4-800/5260	IM7/8552	Cycom977
$\tilde{\sigma}_I^{(0)}$ (MPa)	35.8	29.3	30.6	29.9	31.9	22.8
k_I (MPa)	151	231	133	164	167	161
n_I (-)	0.163	0.222	0.160	0.182	0.183	0.214
$\tilde{\sigma}_{II}^{(0)}$ (MPa)	105	153	90.3	126	106	41.7
k_{II} (MPa)	486	490	332	411	350	1175
n_{II} (-)	0.179	0.142	0.143	0.143	0.143	0.364

Table C.6: Damage parameters and interaction parameters as estimated for the present constitutive model, cf. Sect. 3.5; the values in brackets are used when also the model for localized damage is applied; for details see text.

	AS4/PEEK	AS4/3501-6	glass/epoxy	G4-800/5260	IM7/8552	Cycom977
$e^{(m)}$ (-)		0.01	0.01	0.01	0.01	0.01
$k_d^{(m)}$ (-)		8.32	6.88	8.75	8.86	8.00
$\xi_{a(c)}^{(m)}$ (-)		0.1	0.1	0.1	0.1 (0.015)	0.1 (0.015)
μ_d (-)		10	10	10	10 (0)	10 (0)
λ_I (-)	1.50	1.50	1.50	1.50	1.50	1.50
λ_{II} (-)	0.25	0.25	0.25	0.25	0.25	0.25
$\mu_I^{(t)}$ (-)		0.35	0.30	0.35	0.35	0.10
$\mu_I^{(c)}$ (-)	0.15	0.13	0.19	0.13	0.16	0.08
μ_{II} (-)	1.32	1.75	1.10	1.26	1.07 (0.80)	0.33 (0.25)

Table C.7: Specific fracture energies used within the localized damage model; the values are given in N/mm.

$G^{(ft)}$	$G^{(fc)}$	$G^{(mt)}$	$G^{(mc)}$	$G^{(ps)}$
89.8	78.3	0.2	0.8	1.0

Appendix D

Mean field theory

In the following, Eqns. (3.9) and (3.10) from page 21 are derived. These equations consider the effective¹⁾ compliance tensor of a multiphase composite consisting of a matrix phase and several populations of inhomogeneities. It is important to note that in the present context the matrix phase represents the undamaged, homogenized, transversely isotropic ply material. Accordingly, the matrix phase is referred to by the superscript (0). The populations p of inhomogeneities represent the fictitious inhomogeneities as introduced in Sect.3.1. For a more detailed derivation of the effective compliance tensor or for information about other mean field approaches, the reader is referred to Böhm (2009).

The effective strain, $\langle \boldsymbol{\varepsilon} \rangle$, and the effective stress, $\langle \boldsymbol{\sigma} \rangle$, of the composite material are defined by the volume averages

$$\langle \boldsymbol{\varepsilon} \rangle = \frac{1}{V} \int_V \boldsymbol{\varepsilon}[\mathbf{x}] dV \quad (\text{D.1})$$

$$\langle \boldsymbol{\sigma} \rangle = \frac{1}{V} \int_V \boldsymbol{\sigma}[\mathbf{x}] dV . \quad (\text{D.2})$$

¹⁾In the framework of micromechanics, ‘effective’ refers to far-field properties.

In an analogous way, the total averaged strain and total averaged stress in the individual phases are defined as

$$\langle \boldsymbol{\varepsilon} \rangle^{(0)} = \frac{1}{V^{(0)}} \int_{V^{(0)}} \boldsymbol{\varepsilon}[\mathbf{x}] dV^{(0)} \quad (\text{D.3})$$

$$\langle \boldsymbol{\varepsilon} \rangle^{(p)} = \frac{1}{V^{(p)}} \int_{V^{(p)}} \boldsymbol{\varepsilon}[\mathbf{x}] dV^{(p)} \quad (\text{D.4})$$

and

$$\langle \boldsymbol{\sigma} \rangle^{(0)} = \frac{1}{V^{(0)}} \int_{V^{(0)}} \boldsymbol{\sigma}[\mathbf{x}] dV^{(0)} \quad (\text{D.5})$$

$$\langle \boldsymbol{\sigma} \rangle^{(p)} = \frac{1}{V^{(p)}} \int_{V^{(p)}} \boldsymbol{\sigma}[\mathbf{x}] dV^{(p)}, \quad (\text{D.6})$$

respectively. The relation between the total volume V and the phase volumes, $V^{(0)}$ and $V^{(p)}$, is given by

$$V = V^{(0)} + \sum_p V^{(p)}. \quad (\text{D.7})$$

Furthermore, all phases are taken to behave elastic, i.e. the relations

$$\langle \boldsymbol{\varepsilon} \rangle^{(0)} = \mathbf{C}^{(0)} \langle \boldsymbol{\sigma} \rangle^{(0)} \quad (\text{D.8})$$

$$\langle \boldsymbol{\varepsilon} \rangle^{(p)} = \mathbf{C}^{(p)} \langle \boldsymbol{\sigma} \rangle^{(p)} \quad (\text{D.9})$$

hold with $\mathbf{C}^{(0)} = [\mathbf{E}^{(0)}]^{-1}$ and $\mathbf{C}^{(p)} = [\mathbf{E}^{(p)}]^{-1}$.

Following the approach of Pedersen (1983), averaged perturbation stresses, $\boldsymbol{\sigma}_{\text{ptb}}^{(0)}$ and $\boldsymbol{\sigma}_{\text{ptb}}^{(p)}$, respectively, are taken to act on the phases in addition to the applied homogeneous far-field stress, $\boldsymbol{\sigma}_a$. Accordingly, the phase stresses read

$$\langle \boldsymbol{\sigma} \rangle^{(0)} = \boldsymbol{\sigma}_a + \boldsymbol{\sigma}_{\text{ptb}}^{(0)} \quad (\text{D.10})$$

$$\langle \boldsymbol{\sigma} \rangle^{(p)} = \boldsymbol{\sigma}_a + \boldsymbol{\sigma}_{\text{ptb}}^{(p)}. \quad (\text{D.11})$$

Under these assumptions the averaged strains may be formulated as

$$\langle \boldsymbol{\varepsilon} \rangle^{(0)} = \boldsymbol{\varepsilon}_a^{(0)} + \boldsymbol{\varepsilon}_{\text{ptb}}^{(0)} \quad (\text{D.12})$$

$$\langle \boldsymbol{\varepsilon} \rangle^{(p)} = \boldsymbol{\varepsilon}_a^{(0)} + \boldsymbol{\varepsilon}_{\text{ptb}}^{(0)} + \boldsymbol{\varepsilon}_c^{(p)} = \langle \boldsymbol{\varepsilon} \rangle^{(0)} + \boldsymbol{\varepsilon}_c^{(p)}, \quad (\text{D.13})$$

where $\boldsymbol{\varepsilon}_c^{(p)}$ denotes the constrained strain felt by the inhomogeneities of population p . This constrained strain is handled within Eshelby's equivalent inclusion framework (see e.g. Böhm, 2004). The strain response of the unreinforced matrix, $\boldsymbol{\varepsilon}_a^{(0)}$, and the averaged perturbation strain in the matrix phase, $\boldsymbol{\varepsilon}_{\text{ptb}}^{(0)}$, are given by

$$\boldsymbol{\varepsilon}_a^{(0)} = \mathbf{C}^{(0)} \boldsymbol{\sigma}_a \quad (\text{D.14})$$

$$\boldsymbol{\varepsilon}_{\text{ptb}}^{(0)} = \mathbf{C}^{(0)} \boldsymbol{\sigma}_{\text{ptb}}^{(0)}. \quad (\text{D.15})$$

Due to the outlined assumptions, the equivalent inclusion approach by Eshelby (1957) takes the form

$$\langle \boldsymbol{\sigma} \rangle^{(p)} = \boldsymbol{\sigma}_a + \boldsymbol{\sigma}_{\text{ptb}}^{(p)} \quad (\text{D.16})$$

$$= \mathbf{E}^{(p)} (\boldsymbol{\varepsilon}_a^{(0)} + \boldsymbol{\varepsilon}_{\text{ptb}}^{(0)} + \boldsymbol{\varepsilon}_c^{(p)}) \quad (\text{D.17})$$

$$= \mathbf{E}^{(0)} (\boldsymbol{\varepsilon}_a^{(0)} + \boldsymbol{\varepsilon}_{\text{ptb}}^{(0)} + \boldsymbol{\varepsilon}_c^{(p)} - \boldsymbol{\varepsilon}_\tau^{(p)}), \quad (\text{D.18})$$

where $\boldsymbol{\varepsilon}_\tau^{(p)}$ is the equivalent eigenstrain (Böhm, 2004). From this approach the perturbation stress acting on the inhomogeneities of population p follows as

$$\boldsymbol{\sigma}_{\text{ptb}}^{(p)} = \mathbf{E}^{(0)} (\boldsymbol{\varepsilon}_{\text{ptb}}^{(0)} + \boldsymbol{\varepsilon}_c^{(p)} - \boldsymbol{\varepsilon}_\tau^{(p)}) = \boldsymbol{\sigma}_{\text{ptb}}^{(0)} + \mathbf{E}^{(0)} (\mathbf{S}^{(p)} - \mathbf{I}) \boldsymbol{\varepsilon}_\tau^{(p)}, \quad (\text{D.19})$$

where Eshelby's relation

$$\boldsymbol{\varepsilon}_c^{(p)} = \mathbf{S}^{(p)} \boldsymbol{\varepsilon}_\tau^{(p)} \quad (\text{D.20})$$

has been used. For the perturbation stresses it further holds

$$\left(\sum_p \xi^{(p)} \boldsymbol{\sigma}_{\text{ptb}}^{(p)} \right) + \xi^{(0)} \boldsymbol{\sigma}_{\text{ptb}}^{(0)} = \mathbf{0}, \quad (\text{D.21})$$

where the volume fraction of the matrix phase,

$$\xi^{(0)} = 1 - \sum_p \xi^{(p)}, \quad (\text{D.22})$$

has been used. Finally the perturbation stress and the perturbation strain in the matrix phase read

$$\boldsymbol{\sigma}_{\text{ptb}}^{(0)} = - \left(\sum_p \xi^{(p)} \mathbf{E}^{(0)} (\mathbf{S}^{(p)} - \mathbf{I}) \boldsymbol{\varepsilon}_\tau^{(p)} \right) \quad (\text{D.23})$$

$$\boldsymbol{\varepsilon}_{\text{ptb}}^{(0)} = - \left(\sum_p \xi^{(p)} (\mathbf{S}^{(p)} - \mathbf{I}) \boldsymbol{\varepsilon}_\tau^{(p)} \right). \quad (\text{D.24})$$

In order to derive an explicit relation for the equivalent eigenstrain, Eqn. (D.21) is approximated by

$$\left(\sum_p \xi^{(p)} \right) \boldsymbol{\sigma}_{\text{ptb}}^{(p)} + \xi^{(0)} \boldsymbol{\sigma}_{\text{ptb}}^{(0)} = 0 . \quad (\text{D.25})$$

This approximation leads to

$$\boldsymbol{\sigma}_{\text{ptb}}^{(0)} = - \left(\sum_p \xi^{(p)} \right) \mathbf{E}^{(0)} (\mathbf{S}^{(p)} - \mathbf{I}) \boldsymbol{\varepsilon}_{\tau}^{(p)} = -\xi \mathbf{E}^{(0)} (\mathbf{S}^{(p)} - \mathbf{I}) \boldsymbol{\varepsilon}_{\tau}^{(p)} \quad (\text{D.26})$$

$$\boldsymbol{\varepsilon}_{\text{ptb}}^{(0)} = - \left(\sum_p \xi^{(p)} \right) (\mathbf{S}^{(p)} - \mathbf{I}) \boldsymbol{\varepsilon}_{\tau}^{(p)} = -\xi (\mathbf{S}^{(p)} - \mathbf{I}) \boldsymbol{\varepsilon}_{\tau}^{(p)} , \quad (\text{D.27})$$

where the total volume fraction of inhomogeneities,

$$\xi = \sum_p \xi^{(p)} \quad (\text{D.28})$$

has been used. The last two equations are plugged into Eqns. (D.17) and (D.18), and the equivalent eigenstrain finally reads

$$\boldsymbol{\varepsilon}_{\tau}^{(p)} = - \left[(\mathbf{E}^{(p)} - \mathbf{E}^{(0)}) (\mathbf{S}^{(p)} - \xi (\mathbf{S}^{(p)} - \mathbf{I})) + \mathbf{E}^{(0)} \right]^{-1} ((\mathbf{E}^{(p)} - \mathbf{E}^{(0)}) \boldsymbol{\varepsilon}_{\text{a}}^{(0)}) . \quad (\text{D.29})$$

The approximation used to derive this relation means that the equivalent eigenstrain for population p is computed as if the same perturbation stresses would act in all the other populations. This is of course a rather coarse approximation, but it has an impact on the elasticity predictions only when more than one population of inhomogeneities with significant elastic contrasts between the different populations and/or with significantly different aspect ratios are considered. However, in very pathological situations of the present context the error in the elastic moduli is shown to be in the range of only few percent. In all other situations the elasticity predicted with this approximation is equivalent to classical Mori-Tanaka estimates. Furthermore, remember that the equations derived in this section are not used for micromechanical investigations.

Following the findings of Tandon and Weng (1984), the applied strain can be expressed as

$$\boldsymbol{\varepsilon}_{\text{a}} = \langle \boldsymbol{\varepsilon} \rangle = \left(\sum_p \xi^{(p)} \langle \boldsymbol{\varepsilon} \rangle^{(p)} \right) + \xi^{(0)} \langle \boldsymbol{\varepsilon} \rangle^{(0)} \quad (\text{D.30})$$

$$= \left(\sum_p \xi^{(p)} (\boldsymbol{\varepsilon}_{\text{a}}^{(0)} + \boldsymbol{\varepsilon}_{\text{ptb}}^{(0)} + \boldsymbol{\varepsilon}_{\text{c}}^{(p)}) \right) + \xi^{(0)} (\boldsymbol{\varepsilon}_{\text{a}}^{(0)} + \boldsymbol{\varepsilon}_{\text{ptb}}^{(0)}) \quad (\text{D.31})$$

$$= \boldsymbol{\varepsilon}_{\text{a}}^{(0)} + \boldsymbol{\varepsilon}_{\text{ptb}}^{(0)} + \left(\sum_p \xi^{(p)} \boldsymbol{\varepsilon}_{\text{c}}^{(p)} \right) , \quad (\text{D.32})$$

and it follows

$$\boldsymbol{\varepsilon}_a = \boldsymbol{\varepsilon}_a^{(0)} - \left(\sum_p \xi^{(p)} (\mathbf{S}^{(p)} - \mathbf{I}) \boldsymbol{\varepsilon}_\tau^{(p)} \right) + \left(\sum_p \xi^{(p)} \mathbf{S}^{(p)} \boldsymbol{\varepsilon}_\tau^{(p)} \right) = \boldsymbol{\varepsilon}_a^{(0)} + \left(\sum_p \xi^{(p)} \boldsymbol{\varepsilon}_\tau^{(p)} \right). \quad (\text{D.33})$$

The relation between the applied stress and the applied strain reads

$$\boldsymbol{\sigma}_a = \mathbf{E} \boldsymbol{\varepsilon}_a = \mathbf{E}^{(0)} \boldsymbol{\varepsilon}_a^{(0)}, \quad (\text{D.34})$$

where \mathbf{E} is the unknown effective stiffness tensor of the composite. Consequently, it holds

$$\begin{aligned} \boldsymbol{\sigma}_a &= \mathbf{E} \left(\boldsymbol{\varepsilon}_a^{(0)} + \left(\sum_p \xi^{(p)} \boldsymbol{\varepsilon}_\tau^{(p)} \right) \right) \\ &= \mathbf{E} \left(\mathbf{I} + \left(\sum_p -\xi^{(p)} [(\mathbf{E}^{(p)} - \mathbf{E}^{(0)}) (\mathbf{S}^{(p)} - \xi (\mathbf{S}^{(p)} - \mathbf{I})) + \mathbf{E}^{(0)}]^{-1} (\mathbf{E}^{(p)} - \mathbf{E}^{(0)}) \right) \right) \boldsymbol{\varepsilon}_a^{(0)} \end{aligned}$$

By rearranging the last equations, an expression for the elasticity tensor of the multiphase composite is obtained,

$$\mathbf{E} = \mathbf{E}^{(0)} \left[\mathbf{I} + \left(\sum_p -\xi^{(p)} [(\mathbf{E}^{(p)} - \mathbf{E}^{(0)}) (\mathbf{S}^{(p)} - \xi (\mathbf{S}^{(p)} - \mathbf{I})) + \mathbf{E}^{(0)}]^{-1} (\mathbf{E}^{(p)} - \mathbf{E}^{(0)}) \right) \right]^{-1},$$

from which the compliance tensor follows as

$$\mathbf{C} = \left(\mathbf{I} + \left(\sum_p -\xi^{(p)} [(\mathbf{E}^{(p)} - \mathbf{E}^{(0)}) (\mathbf{S}^{(p)} - \xi (\mathbf{S}^{(p)} - \mathbf{I})) + \mathbf{E}^{(0)}]^{-1} (\mathbf{E}^{(p)} - \mathbf{E}^{(0)}) \right) \right) \mathbf{C}^{(0)}.$$

To obtain the Eqns. (3.9) and (3.10) from Sect. 3.1, the last equation is simplified to

$$\mathbf{C} = \left(\mathbf{I} + \sum_p \mathbf{D}^{(p)} \right) \mathbf{C}^{(0)} \quad (\text{D.35})$$

with

$$\mathbf{D}^{(p)} = -\xi^{(p)} [(\mathbf{E}^{(p)} - \mathbf{E}^{(0)}) (\mathbf{S}^{(p)} - \xi (\mathbf{S}^{(p)} - \mathbf{I})) + \mathbf{E}^{(0)}]^{-1} (\mathbf{E}^{(p)} - \mathbf{E}^{(0)}). \quad (\text{D.36})$$

By some further manipulation, one obtains the fully equivalent expression

$$\mathbf{C} = \mathbf{C}^{(0)} + \left(\sum_p \xi^{(p)} [(\mathbf{C}^{(p)} \mathbf{E}^{(0)} - \mathbf{I})^{-1} + \xi^{(0)} (\mathbf{I} - \mathbf{S}^{(p)})]^{-1} \right) \mathbf{C}^{(0)}. \quad (\text{D.37})$$

Appendix E

Transformations

In the following a transformation from one set of orthogonal axes, $x_1-x_2-x_3$, to another set, $x'_1-x'_2-x'_3$, with the same origin 0 is considered. It is worth to look at such transformations since tensors are defined by their transformation laws. In the famous book written by Nye (1957) one can read the following¹⁾:

A fourth-rank tensor is defined, like tensors of lower rank, by its transformation law. The 81 numbers A_{ijkl} representing a physical quantity are said to form a fourth-rank tensor if they transform on change of axes to A'_{ijkl} , where

$$A'_{ijkl} = n_{im}n_{jn}n_{ko}n_{lp}A_{mnop} .$$

For tensors of rank two it holds analogously

$$a'_{ij} = n_{ik}n_{jl}a_{kl} .$$

In the last two equations, n_{ij} is the matrix of direction cosines, whereas each entry ij in n_{ij} gives the cosine of the angle between x'_i and x_j . Note that in general $n_{ij} \neq n_{ji}$.

With respect to implementation, it is desired to express coordinate transformations by simple matrix operations. Hence, the transformation matrices ${}^{\sigma}\underline{\underline{T}}$ and ${}^{\varepsilon}\underline{\underline{T}}$ are introduced for stress-like and strain-like vector representations of second-rank tensors, respectively, such that it holds

$$\underline{\underline{\sigma}}' = {}^{\sigma}\underline{\underline{T}} \underline{\underline{\sigma}} \quad \text{and} \quad \underline{\underline{\varepsilon}}' = {}^{\varepsilon}\underline{\underline{T}} \underline{\underline{\varepsilon}} . \quad (\text{E.1})$$

¹⁾Nye uses T_{ijkl} instead of A_{ijkl}

For the purpose of a simple example, a rotation about the principal axes x_1 is considered, the corresponding matrix of direction cosines for passive rotation (the coordinate system is rotated, not the quantity itself) reads

$$n_{ij}^{(1)} = \begin{bmatrix} 1 & 0 & 0 \\ 0 & c & s \\ 0 & -s & c \end{bmatrix}, \quad (\text{E.2})$$

where $c = \cos \alpha$, $s = \sin \alpha$ is used and α is the angle of rotation. In order to compute the transformation matrices, one has to compare

$$\sigma'_{ij} = n_{ik}^{(1)} n_{jl}^{(1)} \sigma_{kl} \quad \text{with} \quad \underline{\underline{\sigma}}' = {}^{\sigma} \underline{\underline{T}}^{(1)} \underline{\underline{\sigma}}$$

and

$$\varepsilon'_{ij} = n_{ik}^{(1)} n_{jl}^{(1)} \varepsilon_{kl} \quad \text{with} \quad \underline{\underline{\varepsilon}}' = {}^{\varepsilon} \underline{\underline{T}}^{(1)} \underline{\underline{\varepsilon}}.$$

This leads to the transformation matrices for rotation about x_1 , which read

$${}^{\sigma} \underline{\underline{T}}^{(1)} = \begin{bmatrix} 1 & 0 & 0 & 0 & 0 & 0 \\ 0 & c^2 & s^2 & 0 & 0 & +2cs \\ 0 & s^2 & c^2 & 0 & 0 & -2cs \\ 0 & 0 & 0 & +c & +s & 0 \\ 0 & 0 & 0 & -s & +c & 0 \\ 0 & -cs & +cs & 0 & 0 & c^2 - s^2 \end{bmatrix} \quad (\text{E.3})$$

and

$${}^{\varepsilon} \underline{\underline{T}}^{(1)} = \begin{bmatrix} 1 & 0 & 0 & 0 & 0 & 0 \\ 0 & c^2 & s^2 & 0 & 0 & +cs \\ 0 & s^2 & c^2 & 0 & 0 & -cs \\ 0 & 0 & 0 & +c & +s & 0 \\ 0 & 0 & 0 & -s & +c & 0 \\ 0 & -2cs & +2cs & 0 & 0 & c^2 - s^2 \end{bmatrix}. \quad (\text{E.4})$$

With the transformation matrices defined, e.g. the transformation rule of the elasticity matrix can be derived. To this end, the generalized hook's law can be used. When

$$\underline{\underline{\sigma}} = \underline{\underline{E}} \underline{\underline{\varepsilon}} \quad \text{and} \quad \underline{\underline{\sigma}}' = \underline{\underline{E}}' \underline{\underline{\varepsilon}}' \quad (\text{E.5})$$

are required to hold, the transformation rule

$$\underline{\underline{\mathbf{E}'}} = {}^{\sigma}\underline{\underline{\mathbf{T}}} \underline{\underline{\mathbf{E}}} [{}^{\sigma}\underline{\underline{\mathbf{T}}}]^{\text{T}} \quad (\text{E.6})$$

is obtained easily, in which the relation

$$[{}^{\varepsilon}\underline{\underline{\mathbf{T}}}]^{\text{T}} = [{}^{\sigma}\underline{\underline{\mathbf{T}}}]^{-1} \quad (\text{E.7})$$

has been applied. Assuming that the Eshelby tensor is represented by the matrix $\underline{\underline{\mathbf{S}}}$ such that

$$\underline{\underline{\varepsilon}}_c = \underline{\underline{\mathbf{S}}} \underline{\underline{\varepsilon}}_{\tau} \quad \text{and} \quad \underline{\underline{\varepsilon}}'_c = \underline{\underline{\mathbf{S}'}} \underline{\underline{\varepsilon}}'_{\tau} \quad (\text{E.8})$$

hold, the transformation rule for the matrix $\underline{\underline{\mathbf{S}}}$ reads

$$\underline{\underline{\mathbf{S}'}} = {}^{\varepsilon}\underline{\underline{\mathbf{T}}} \underline{\underline{\mathbf{S}}} [{}^{\varepsilon}\underline{\underline{\mathbf{T}}}]^{-1} = {}^{\varepsilon}\underline{\underline{\mathbf{T}}} \underline{\underline{\mathbf{S}}} [{}^{\sigma}\underline{\underline{\mathbf{T}}}]^{\text{T}}. \quad (\text{E.9})$$

Appendix F

Energy dissipation

Following the Abaqus/Standard User's Manual (2009), an energy equation can be derived which reads

$$\rho \frac{dU}{dt} = \boldsymbol{\sigma} \cdot \dot{\boldsymbol{\xi}}, \quad (\text{F.1})$$

where U is the internal energy per unit mass and ρ is the mass density. Here the component vector $\boldsymbol{\sigma}$ is not the output of the constitutive law but represents the stresses which actually prevail in the FEM model. The component vector $\boldsymbol{\sigma}$, therefore, accounts for numerical stabilizing methods. The internal energy W stored in the volume V is defined by

$$W = \int_V \rho U dV. \quad (\text{F.2})$$

However, it is assumed that the material behavior is determined by local effects only. Accordingly, the volume specific equivalent to W is of interest, which reads

$$w = \rho U. \quad (\text{F.3})$$

By integration of Eqn. (F.1) the volume specific internal energy can be expressed by

$$w = \int_0^t \boldsymbol{\sigma} \cdot \dot{\boldsymbol{\xi}} d\tau = \quad (\text{F.4})$$

$$\underbrace{\int_0^t \boldsymbol{\sigma}^{(\text{nv})} \cdot \dot{\boldsymbol{\xi}}^{(\text{el})} d\tau}_{w_{\text{E}}^{(\text{nv})}} + \underbrace{\int_0^t \boldsymbol{\sigma}^{(\text{nv})} \cdot \dot{\boldsymbol{\xi}}^{(\text{pl})} d\tau}_{w_{\text{P}}^{(\text{nv})}} + \underbrace{\int_0^t (\boldsymbol{\sigma}^{(\text{v})} - \boldsymbol{\sigma}^{(\text{nv})}) \cdot \dot{\boldsymbol{\xi}} d\tau}_{w^{(\text{v})}} + w^{(\text{a})}. \quad (\text{F.5})$$

The first term introduced in Eqn. (F.5) is referred to as volume specific elastic strain energy, $w_E^{(nv)}$, which can be further split up, i.e.

$$w_E^{(nv)} = w_R^{(nv)} + w_D^{(nv)}. \quad (F.6)$$

Here $w_R^{(nv)}$ is the volume specific recoverable strain energy which reads

$$w_R^{(nv)} = \int_0^t \left(\underline{\underline{\mathbf{E}}}_t \underline{\underline{\boldsymbol{\varepsilon}}}^{(el)} \right) \cdot \underline{\underline{\dot{\boldsymbol{\varepsilon}}}}^{(el)} d\tau = \frac{1}{2} \underline{\underline{\boldsymbol{\varepsilon}}}^{(el)} \cdot \underline{\underline{\mathbf{E}}}_t \underline{\underline{\boldsymbol{\varepsilon}}}^{(el)} \quad (F.7)$$

with $\underline{\underline{\mathbf{E}}}_t$ being the elasticity matrix reached at time t and fixed upon unloading. Furthermore, $w_D^{(nv)}$ is the volume specific energy dissipated through damage which reads

$$w_D^{(nv)} = w_E^{(nv)} - w_R^{(nv)} = \int_0^t \underline{\underline{\boldsymbol{\sigma}}}^{(nv)} \cdot \underline{\underline{\dot{\boldsymbol{\varepsilon}}}}^{(el)} d\tau - \int_0^t \left(\underline{\underline{\mathbf{E}}}_t \underline{\underline{\boldsymbol{\varepsilon}}}^{(el)} \right) \cdot \underline{\underline{\dot{\boldsymbol{\varepsilon}}}}^{(el)} d\tau. \quad (F.8)$$

The second term introduced in Eqn. (F.5), $w_P^{(nv)}$, is the the volume specific energy dissipated through plasticity; the third term, $w^{(v)}$, is the the volume specific energy dissipated through viscous regularization; the last term, $w^{(a)}$, is the volume specific energy introduced artificially (e.g. by the **Abaqus** keyword ***STABILIZE**) to improve the convergence behavior. Note that for the rates of the volume specific energy dissipation it must hold $\dot{w}_D^{(nv)} \geq 0$ and $\dot{w}_P^{(nv)} \geq 0$ at any time in order to be consistent with thermodynamics. All the mentioned volume specific energies are available as **UMAT** output and **Abaqus** output, respectively.

Appendix G

Usage of the UMAT

In this chapter some comments are given with respect to the usage of the UMAT. In the next subsection the keywords are discussed which have to be included in the **Abaqus** input file. Afterwards, the material parameters (**PROPS**) and the solution dependent variables (**STATEV**) are discussed.

Abaqus interface

In **Abaqus** the FEM model of the considered problem has to be defined on basis of an input file, in which keywords (***KEYWORD**) are followed by their parameters. When the present UMAT is used, the input file should contain the lines

```
*MATERIAL, NAME=NAME-OF-THE-MATERIAL
*DEPVAR
    340
*USER MATERIAL, CONSTANTS=80
    material parameters PROPS ...
*EXPANSION, TYPE=ORTHO
     $\alpha_{11}, \alpha_{22}, \alpha_{33}$ 
*INITIAL CONDITIONS, TYPE=SOLUTION
    initialization of the solution dependent variables STATEV ...
*INITIAL CONDITIONS, TYPE=TEMPERATURE
    name-of-the-element-set, Tsf
```

Within the keyword `*DEPVAR`, the number of the solution dependent variables is defined, i.e. it is set to 340. Within the keyword `*USER MATERIAL`, `CONSTANTS=80`, the list `PROPS` is given as discussed in detail in the next subsection. The respective parameters concern the initial ply stiffness, values for the nominal ply strength, and the damage and plasticity parameters. Additionally, flags can be set concerning the desired material model. Within the keyword `*EXPANSION`, `TYPE=ORTHO`, the thermal expansion behavior of the ply material is defined. Within the keyword `*INITIAL CONDITIONS`, `TYPE=SOLUTION`, the solution dependent variables `STATEV` are initialized. The solution dependent variables as well as the respective initialization are discussed in detail in the last subsection of this chapter. Within the keyword `*INITIAL CONDITIONS`, `TYPE=TEMPERATURE`, the stress free temperature of the laminate, T_{sf} , can be defined.

In order to make the UMAT user-friendly, a `python` script has been developed which generates the required input out of handy material data files. If desired, the script thereby follows the calibration scheme as described in Sect. 3.5.

As the UMAT is usually used in combination with a `*SHELL SECTION` definition, the transverse shear stiffness has to be defined manually using the keyword `*TRANSVERSE SHEAR STIFFNESS`. Note that the usage of the UMAT is questionable when the transverse shear stiffness is important for the considered problem. Furthermore, it is recommended to define ‘enhanced hourglass control’ within the keyword `*SECTION CONTROLS` when first-order, reduced-integration elements are used. Alternatively, hourglass control stiffness parameters have to be defined manually using the keyword `*HOURGLASS STIFFNESS`.

Input of the UMAT

In this section the list PROPS containing the material parameters is described. Note that all entries not mentioned below must be set to 0.

switches

- PROPS(1) switch concerning the desired material model:
 0 ... linear elastic material behavior
 1 ... elasto-plastic material behavior
 2 ... elasto-damage material behavior
 3 ... elasto-plastic-damage material behavior:
- PROPS(2) switch concerning softening behavior:
 0 ... no softening
 1 ... softening due to progressive fiber failure
 2 ... softening due to progressive matrix failure
 3 ... full softening
- PROPS(3) switch concerning UMAT output:
 0 ... no output is written to *job.msg*
 n ... output for the element number n is written to *job.msg*

initial elastic properties

- PROPS(5...7) initial Young's moduli: $E_1^{(0)}, E_2^{(0)}, E_3^{(0)}$
 PROPS(8...10) initial shear moduli: $G_{12}^{(0)}, G_{13}^{(0)}, G_{23}^{(0)}$
 PROPS(11...13) initial Poisson ratios: $\nu_{12}^{(0)}, \nu_{13}^{(0)}, \nu_{23}^{(0)}$

nominal ply strength values

- PROPS(14...18) strength values: $X^{(t)}, X^{(c)}, Y^{(t)}, Y^{(c)}, S$
 PROPS(19...20) slope parameters of Puck: $p^{(t)}, p^{(c)}$
 PROPS(23...24) weakening parameters of Puck: s, m

damage parameters

- PROPS(25...26) aspect ratios: $e^{(f)}$, $e^{(m)}$
- PROPS(33...37) specific fracture energies: $G^{(ft)}$, $G^{(fc)}$, $G^{(mt)}$, $G^{(mc)}$, $G^{(ps)}$
- PROPS(49) parameter for stiffness recovery: μ_d
- PROPS(50) allowable or critical amount of matrix damage: $\xi_a^{(m)}$ or $\xi_c^{(m)}$
- PROPS(52) evolution parameter for distributed damage: $k_d^{(m)}$
- PROPS(54) correction factor, f_L , which is incorporated in the computation of the characteristic length by $L = f_L L_{abq}$, where L_{abq} is the characteristic element length estimated by **Abaqus**
- PROPS(45...48) viscous parameters: $\eta^{(ft)}$, $\eta^{(fc)}$, $\eta^{(mt)}$, $\eta^{(mc)}$

plasticity parameters

- PROPS(57...64) interaction parameters: $\mu_I^{(t)}$, $\mu_I^{(c)}$, μ_{II} , λ_I , λ_{II} , 0, 8, 8
- PROPS(65...72) hardening p_I: $\tilde{\sigma}_I^{(0)}$, 0, $\tilde{\sigma}_I^*$ at $\kappa_I = \kappa_I^*$, κ_I^* , 0, 0, k_I , n_I
- PROPS(73...80) hardening p_{II}: $\tilde{\sigma}_{II}^{(0)}$, 0, $\tilde{\sigma}_{II}^*$ at $\kappa_{II} = \kappa_{II}^*$, κ_{II}^* , 0, 0, k_{II} , n_{II}

Output of the UMAT

In this section the list STATEV containing the solution dependent variables is described. Note that entries not mentioned below are used to store output which is of minor importance for the user.

flags

STATEV(1)	flag concerning plasticity
	0 ... plasticity was not active in current increment
	1 ... plasticity was active in current increment
STATEV(2)	flag concerning damage
	0 ... damage was not active in current increment
	1 ... damage was active in current increment
STATEV(3)	flag concerning softening
	0 ... softening was not active in current increment
	1 ... softening was active in current increment
STATEV(4)	flag concerning UMAT errors
	0 ... no errors have occurred
	1 ... errors have occurred

actual elastic properties

STATEV(5...7)	actual Young's moduli: E_1, E_2, E_3
STATEV(8...10)	actual shear moduli: G_{12}, G_{13}, G_{23}
STATEV(11...13)	actual Poisson ratios: $\nu_{12}, \nu_{13}, \nu_{23}$

variables concerning UMAT errors

STATEV(14)	step number of the first UMAT error
STATEV(15)	increment number of the first UMAT error
STATEV(16)	identification number of the first UMAT error

variables from various failure criteria

- STATEV(17...18) factors of exertion: $f_E^{(f)}$, $f_E^{(m)}$
 STATEV(19) fracture plane angle predicted by Puck: φ
 STATEV(20) failure mode predicted by Puck: 1 $\hat{=}$ A; 2 $\hat{=}$ B; 3 $\hat{=}$ C
 STATEV(21...23) other factors of exertion: $f_{E,Puck}$, $f_{E,TsaiHill}$, $f_{E,TsaiWu}$

variables concerning damage

- STATEV(25...28) damage variables: ξ_1 , ξ_2 , ξ_3 , ξ_4

variables concerning plasticity

- STATEV(33...34) internal hardening variables: κ_I , κ_{II}
 STATEV(35...40) plastic strain components: 0, $\varepsilon_{22}^{(pl)}$, $\varepsilon_{33}^{(pl)}$, $\gamma_{12}^{(pl)}$, 0, 0

volume specific energies

- STATEV(41...45) energy densities: $w_E^{(nv)}$, $w_R^{(nv)}$, $w_D^{(nv)}$, $w_P^{(nv)}$, $w^{(v)}$

variables concerning the non-viscous system

- STATEV(81...84) damage variables: $\xi_1^{(nv)}$, $\xi_2^{(nv)}$, $\xi_3^{(nv)}$, $\xi_4^{(nv)}$
 STATEV(89...94) stress components: $\sigma_{11}^{(nv)}$, $\sigma_{22}^{(nv)}$, $\sigma_{33}^{(nv)}$, $\sigma_{12}^{(nv)}$, $\sigma_{13}^{(nv)}$, $\sigma_{23}^{(nv)}$

elasticity matrices

- STATEV(100...135) initial elasticity matrix: $\underline{\underline{E}}^{(0)}$
 STATEV(140...175) actual elasticity matrix: $\underline{\underline{E}}$

Eshelby matrices

- STATEV(180...215) Eshelby matrix of population 1: $\underline{\underline{S}}^{(1)}$
 STATEV(220...255) Eshelby matrix of population 2: $\underline{\underline{S}}^{(2)}$
 STATEV(260...295) Eshelby matrix of population 3: $\underline{\underline{S}}^{(3)}$
 STATEV(300...335) Eshelby matrix of population 4: $\underline{\underline{S}}^{(4)}$

Storage of matrices. The matrix representations $\underline{\underline{\mathbf{E}}}^{(0)}$, $\underline{\underline{\mathbf{E}}}$, $\underline{\underline{\mathbf{S}}}^{(1)}$, $\underline{\underline{\mathbf{S}}}^{(2)}$, $\underline{\underline{\mathbf{S}}}^{(3)}$, and $\underline{\underline{\mathbf{S}}}^{(4)}$ are stored in the list `STATEV` according to the `FROTRAN` convention, i.e. in a column-by-column manner. Furthermore, for the matrix representations of the Eshelby tensors it must hold

$$\underline{\underline{\boldsymbol{\varepsilon}}}_c^{(p)} = \underline{\underline{\mathbf{S}}}^{(p)} \underline{\underline{\boldsymbol{\varepsilon}}}_\tau^{(p)} . \quad (\text{G.1})$$

Initialization of STATEV. Subsequent to `*INITIAL CONDITIONS, TYPE=SOLUTION`, the solution dependent variables must be initialized. Thereby, all of them should be set to 0 apart from the ones which are used for matrix storage. In order to initialize the variables for matrix storage, the `UMAT` provides two possibilities. If it is desired that the computation of the initial elasticity and Eshelby matrices is done by the `UMAT` using the parameters from the list `PROPS`, also the solution dependent variables `STATEV(100...335)` should be set to 0. However, if a relatively large FEM model is considered, this approach might be too computationally expensive as the evaluation is done at the beginning of the analysis for each Gauss point individually. Such computations are suppressed when non-zero initial values are found by the `UMAT`, i.e. when the the evaluation of the matrices and a corresponding initialization of the values `STATEV(100...335)` is done by the user (e.g. using the `python` script).

Bibliography

- D. H. Allen. Damage evolution in laminates. In R. Talreja, editor, *Damage Mechanics of Composite Materials*, volume 9 of *Composite Materials Series*, chapter 3. Elsevier Science Ltd., Oxford, UK, 1994.
- O. Allix, L. Daudeville, and P. Ladevèze. Delamination and damage mechanics. In D. Baptiste, editor, *Mechanics and Mechanisms of Damage in Composites and Multi-Materials*, pages 143–158. Mechanical Engineering Publications Limited, London, UK, 1991.
- F. Armero and S. Oller. A general framework for continuum damage models. I. infinitesimal plastic damage models in stress space. *Int. J. Sol. Struct.*, 37(48-50): 7409–7436, 2000.
- E. J. Barbero and P. Lonetti. An inelastic damage model for fiber reinforced laminates. *J. Compos. Mater.*, 36(8):941–962, 2002.
- S. Basu, A. M. Waas, and D. R. Ambur. Prediction of progressive failure in multidirectional composite laminated panels. *Int. J. Sol. Struct.*, 44(9):2648–2676, 2007.
- Z. P. Bažant and B. H. Oh. Crack band theory for fracture of concrete. *Materials and Structures*, 16(3):155–177, 1983.
- Z. P. Bažant, J. J. H. Kim, I. M. Daniel, E. Becq-Giraudon, and G. Zi. Size effect on compression strength of fiber composites failing by kink band propagation. *Int. J. Fract.*, 95(1):103–141, 1999.
- H. J. Böhm. A Short Introduction to Continuum Micromechanics. In H. J. Böhm, editor, *Mechanics of Microstructured Materials*, volume 464 of *CISM courses and lectures*, pages 1–40. Springer-Verlag Wien New York, 2004.

- H. J. Böhm. Notes on some mean field approaches for thermoelastic two-phase composites. Institute of Lightweight Design and Structural Biomechanics, Vienna University of Technology, Vienna, Austria, 2009.
- P. P. Camanho, C. G. Dávila, S. T. Pinho, L. Iannucci, and P. Robinson. Prediction of in situ strengths and matrix cracking in composites under transverse tension and in-plane shear. *Composites Part A*, 37(2):165–176, 2006.
- K. Y. Chang, S. Llu, and F. K. Chang. Damage tolerance of laminated composites containing an open hole and subjected to tensile loadings: Part II—analysis. *J. Compos. Mater.*, 25:2–43, 1991.
- C. G. Dávila, C. A. Rose, and P. P. Camanho. A procedure for superposing linear cohesive laws to represent multiple damage mechanisms in the fracture of composites. *Int. J. Fract.*, 158(2):211–223, 2009.
- G. Duvaut and J. L. Lions. Inequalities in physics and mechanics, 1979.
- J. D. Eshelby. The determination of the elastic field of an ellipsoidal inclusion, and related problems. *Pro.Roy.Soc.London*, 421:376–396, 1957.
- Th. Flatscher, C. Schuecker, and H. E. Pettermann. Prediction of plastic strain accumulation in continuous fiber reinforced laminates by a constitutive ply model. *Int. J. Fract.*, (158):145–156, 2009a. doi: 10.1007/s10704-009-9345-4.
- Th. Flatscher, C. Schuecker, and H. E. Pettermann. A constitutive ply model for stiffness degradation and plastic strain accumulation: Its application to WWFE-III (Part A). 2009b. (submitted for World Wild Failure Exercise III).
- Th. Flatscher, C. Schuecker, and H. E. Pettermann. A constitutive model for continuous fiber reinforced polymer plies. *Proceedings in Applied Mathematics and Mechanics*, 2009c. (submitted).
- A. C. Gavazzi and D. C. Lagoudas. On the numerical evaluation of Eshelby’s tensor and its application to elastoplastic fibrous composites. *Comput. Mech.*, 7:13–19, 1990.
- C. González and J. LLorca. Mechanical behavior of unidirectional fiber-reinforced polymers under transverse compression: Microscopic mechanisms and modeling. *Comp. Sci. and Tech.*, 67:2795–2806, 2007.

- P. Grassl and M. Jirásek. Damage-plastic model for concrete failure. *Int. J. Sol. Struct.*, 43(22-23):7166–7196, 2006.
- B. G. Green, M. R. Wisnom, and S. R. Hallett. An experimental investigation into the tensile strength scaling of notched composites. *Composites Part A*, 38(3):867–878, 2007.
- S. R. Hallett, B. G. Green, W. G. Jiang, K. H. Cheung, and M. R. Wisnom. The open hole tensile test: a challenge for virtual testing of composites. *Int. J. Fract.*, 158(2):169–181, 2009.
- E. Hansen, K. Willam, and I. Carol. A two-surface anisotropic damage/plasticity model for plain concrete. In R. de Borst, J. Mazars, G. Pijaudier-Cabot, and J. G. M. van Mier, editors, *Proceedings of 4th International Conference on Fracture Mechanics of Concrete and Concrete Structures*, pages 549–556. Balkema, 2001.
- Z. Hashin. Failure criteria for unidirectional fiber composites. *J. Appl. Mech.*, 47(6):329–334, 1980.
- C. T. Herakovich, R. D. Schroedter, A. Gasser, and L. Guitard. Damage evolution in $[\pm 45]_S$ laminates with fiber rotation. *Comp. Sci. and Tech.*, 60(15):2781–2789, 2000.
- M. Hinton, A. S. Kaddour, and P. D. Soden. *Failure Criteria in Fibre-Reinforced-Polymer Composites: The World-Wide Failure Exercise*. Elsevier Science & Technology Books, 2004.
- S.-Y. Hsu, T. J. Vogler, and S. Kyriakides. Inelastic behavior of an AS4/PEEK composite under combined transverse compression and shear. Part II: modeling. *Int. J. Plast.*, 15:807–836, 1999.
- W. G. Jiang, S. R. Hallett, B. G. Green, and M. R. Wisnom. A concise interface constitutive law for analysis of delamination and splitting in composite materials and its application to scaled notched tensile specimens. *Int. J. Numer. Meth. Engng*, 69(9):1982, 2007.
- M. Jirásek. Modeling of Localized Inelastic Deformation. Lecture Notes, 2005.

- R. M. Jones. *Mechanics of Composite Materials*. Taylor & Francis Inc., Philadelphia, PA, USA, second edition, 1999.
- L. M. Kachanov. On creep rupture time. *Izv. Acad. Nauk SSSR, Otd. Techn. Nauk*, 8:26–31, 1958.
- A. S. Kaddour, M. J. Hinton, S. Li, and P. Smith. Instructions to contributors of the third World-Wide Failure Exercise. 2010. (to be published).
- M. Knops. *Analysis of Failure in Fiber Polymer Laminates*. Springer-Verlag Berlin Heidelberg, 2008.
- P. Ladevèze. On a damage mechanics approach. In D. Baptiste, editor, *Mechanics and Mechanisms of Damage in Composites and Multi-Materials*, pages 119–142. Mechanical Engineering Publications Limited, London, UK, 1991.
- P. Ladevèze. A damage mesomodel of laminate composites. In J. Lemaitre, editor, *Handbook of Materials Behavior Models*, pages 1004–1014. Academic Press, London, UK, 2001.
- F. Lagattu and M. C. Lafarie-Frenot. Variation of PEEK matrix crystallinity in APC-2 composite subjected to large shearing deformations. *Comp. Sci. and Tech.*, 60(4):605–612, 2000.
- I. Lapczyk and J. A. Hurtado. Progressive damage modeling in fiber-reinforced materials. *Composites Part A*, 38:2333–2341, 2007.
- J. Lemaitre. *A Course on Damage Mechanics*. Springer-Verlag Berlin Heidelberg, 1992.
- L. B. Lessard and F. K. Chang. Damage tolerance of laminated composites containing an open hole and subjected to compressive loadings: Part II—experiment. *J. Compos. Mater.*, 25:44–64, 1991.
- S. Li, S. R. Reid, and P. D. Soden. A continuum damage model for transverse matrix cracking in laminated fibre-reinforced composites. *Phil. Trans. R. Soc. Lond. A*, 356:2379–2412, 1998.
- J. Lubliner. *Plasticity theory*. Macmillan Publishing Company, 1990.

- P. Maimí, P. P. Camanho, J. A. Mayugo, and C. G. Dávila. A continuum damage model for composite laminates: Part I – constitutive model. *Mech. Mat.*, 39:897–908, 2007a.
- P. Maimí, P. P. Camanho, J. A. Mayugo, and C. G. Dávila. A continuum damage model for composite laminates: Part II – computational implementation and validation. *Mech. Mat.*, 39:909–919, 2007b.
- P. Maimí, J. A. Mayugo, and P. P. Camanho. A three-dimensional damage model for transversely isotropic composite laminates. *J. Compos. Mater.*, 42:2717–2745, 2008.
- H. Mang and G. Hofstetter. *Festigkeitslehre*. Springer-Verlag Wien New York, 2004.
- A. Matzenmiller, J. Lubliner, and R. L. Taylor. A constitutive model for anisotropic damage in fiber-composites. *Mech. Mat.*, 20:125–152, 1995.
- P. Middendorf. Auslegung und Simulation von Composite Strukturen in der Luftfahrt: Stand der Technik, zukünftige Anforderungen und Forschungsschwerpunkte. *NAFEMS Magazin*, 1:34–42, 2008.
- J. C. Nadeau and M. Ferrari. Invariant tensor-to-matrix mappings for evaluation of tensorial expressions. *J. Elasticity*, 52:43–61, 1998.
- A. T. Nettles and E. J. Biss. Low temperature mechanical testing of carbon-fiber/epoxy-resin composite materials. Technical Report TP 3663, NASA, 1996.
- S. Nogales. *Numerical Simulation of the Thermal and Thermomechanical Behaviour of Metal Matrix Composites*. PhD thesis, Institute of Lightweight Design and Structural Biomechanics, Vienna University of Technology, Vienna, Austria, 2008. (also published in: VDI Fortschritt-Berichte VDI Reihe 18 Nr. 317. VDI-Verlag, Düsseldorf).
- J. F. Nye. *Physical properties of Crystals*. Oxford Science Publications, 1957.
- O. B. Pedersen. Thermoelasticity and plasticity of composites – I: Mean field theory. *Acta Metall.*, 31(11):1795–1808, 1983.

- E. J. Pineda, A. M. Waas, B. A. Bednarczyk, C. S. Collier, and P. W. Yarrington. Progressive damage and failure modeling in notched laminated fiber reinforced composites. *Int. J. Fract.*, 158:125–143, 2009.
- S. T. Pinho, P. Robinson, and L. Iannucci. Fracture toughness of the tensile and compressive fibre failure modes in laminated composites. *Comp. Sci. and Tech.*, 66(13):2069–2079, 2006.
- S. T. Pinho, P. Robinson, and L. Iannucci. Developing a four point bend specimen to measure the mode I intralaminar fracture toughness of unidirectional laminated composites. *Comp. Sci. and Tech.*, 69(7-8):1303–1309, 2009.
- A. Puck. *Festigkeitsanalyse von Faser-Matrix-Laminaten*. Carl Hanser Verlag, München Wien, Germany, 1996.
- A. Puck and M. Mannigel. Physically based non-linear stress-strain relations for the inter-fibre fracture analysis of FRP laminates. *Comp. Sci. and Tech.*, 67:1955–1964, 2007.
- A. Puck and H. Schürmann. Failure analysis of FRP laminates by means of physically based phenomenological models. *Comp. Sci. and Tech.*, 58:1045–1067, 1998.
- A. Puck and H. Schürmann. Failure analysis of FRP laminates by means of physically based phenomenological models. *Comp. Sci. and Tech.*, 62:1633–1662, 2002.
- A. Puck, J. Kopp, and M. Knops. Guidelines for the determination of the parameters in Puck’s action plane strength criterion. *Comp. Sci. and Tech.*, 62:(3) 371–378; (9) 1275, 2002.
- J. N. Rabotnov. *Creep Problems in Structural Members*, volume 7 of *North-Holland series in Applied Mathematics and Mechanics*. North-Holland, Amsterdam, Netherlands, 1969.
- R. A. Schapery. Prediction of compressive strength and kink bands in composites using a work potential. *Int. J. Sol. Struct.*, 32(6):739–766, 1995.
- C. Schuecker. *Mechanism based modeling of damage and failure in fiber reinforced polymer laminates*. PhD thesis, Institute of Lightweight Design and Structural

- Biomechanics, Vienna University of Technology, Vienna, Austria, 2005. (also published in: VDI Fortschritt-Berichte VDI Reihe 18 Nr. 303. VDI-Verlag, Düsseldorf).
- C. Schuecker and H. E. Pettermann. A continuum damage model for fiber reinforced laminates based on ply failure mechanisms. *Compos. Struct.*, 76(1-2):162–173, 2006.
- C. Schuecker and H. E. Pettermann. Fiber reinforced laminates: Progressive damage modeling based on failure mechanisms. *Arch. Comput. Methods Eng.*, 15:163–184, 2008a.
- C. Schuecker and H. E. Pettermann. Combining elastic brittle damage with plasticity to model the non-linear behavior of fiber reinforced laminates. In P. P. Camanho, C. G. Dávila, S. T. Pinho, and J. J. C. Remmers, editors, *Mechanical Response of Composites*, pages 99–117. Springer, 2008b.
- C. Schuecker, C. G. Dávila, and H. E. Pettermann. Modeling the non-linear response of fiber-reinforced laminates using a combined damage/plasticity model. Technical Report NASA/TM-2008-215314, NASA Langley Research Center, 2008.
- H. Schürmann. *Konstruieren mit Faser-Kunststoff-Verbunden*. Springer-Verlag Berlin Heidelberg, 2005.
- J. C. Simo and T. J. R. Hughes. *Computational Inelasticity*. Springer-Verlag New York Berlin Heidelberg, 1998.
- P. D. Soden, M. J. Hinton, and A. S. Kaddour. Lamina properties, lay-up configurations and loading conditions for a range of fibre-reinforced composite laminates. *Comp. Sci. and Tech.*, 58:1011–1022, 1998.
- P. D. Soden, M. J. Hinton, and A. S. Kaddour. Biaxial test results for strength and deformation of a range of E-glass and carbon fibre reinforced composite laminates: failure exercise benchmark data. *Comp. Sci. and Tech.*, 62:1489–1514, 2002.
- S. M. Spearing and P. W. R. Beaumont. Fatigue damage mechanics of composite materials. I: Experimental measurement of damage and post-fatigue properties. *Comp. Sci. and Tech.*, 44(2):159–168, 1992.

- R. Talreja. Damage characterization by internal variables. In R. Talreja, editor, *Damage Mechanics of Composite Materials*, volume 9 of *Composite Materials Series*, chapter 2. Elsevier Science Ltd., Oxford, UK, 1994.
- S. C. Tan. A progressive failure model for composite laminates containing openings. *J. Compos. Mater.*, 25(5):556, 1991.
- G. P. Tandon and G. J. Weng. The effect of aspect ratio of inclusions on the elastic properties of unidirectionally aligned composites. *Polym. Compos.*, 5:327–333, 1984.
- E. Totry, C. González, and J. LLorca. Prediction of the failure locus of C/PEEK composites under transverse compression and longitudinal shear through computational micromechanics. *Comp. Sci. and Tech.*, 68:3128–3136, 2008.
- W. Van Paepegem, I. De Baere, and J. Degrieck. Modelling the nonlinear shear stress–strain response of glass fibre-reinforced composites. Part I: Experimental results. *Comp. Sci. and Tech.*, 66:1455–1464, 2006a.
- W. Van Paepegem, I. De Baere, and J. Degrieck. Modelling the nonlinear shear stress–strain response of glass fibre-reinforced composites. Part II: Model development and finite element simulations. *Comp. Sci. and Tech.*, 66:1465–1478, 2006b.
- J. Varna, R. Joffe, N. V. Akshantala, and R. Talreja. Damage in composite laminates with off-axis plies. *Comp. Sci. and Tech.*, 59:2139–2147, 1999.
- J. Varna, R. Joffe, and R. Talreja. A synergistic damage-mechanics analysis of transverse cracking in $[\pm\theta/90_4]_s$ laminates. *Comp. Sci. and Tech.*, 61:657–665, 2001.
- T. J. Vogler and S. Kyriakides. Inelastic behavior of an AS4/PEEK composite under combined transverse compression and shear. Part I: experiments. *Int. J. Plast.*, 15: 783–806, 1999.
- Q. Yang and B. Cox. Cohesive models for damage evolution in laminated composites. *Int. J. Fract.*, 133(2):107–137, 2005.
- O. C. Zienkiewicz and R. L. Taylor. *The Finite Element Method*, volume 1&2. Butterworth-Heinemann, 2000.